Plastic-Free Oceans

Predicting Net Behaviour by Combining Computational Modelling and Experimental Hydrodynamic Analysis

Robin van Bohemen

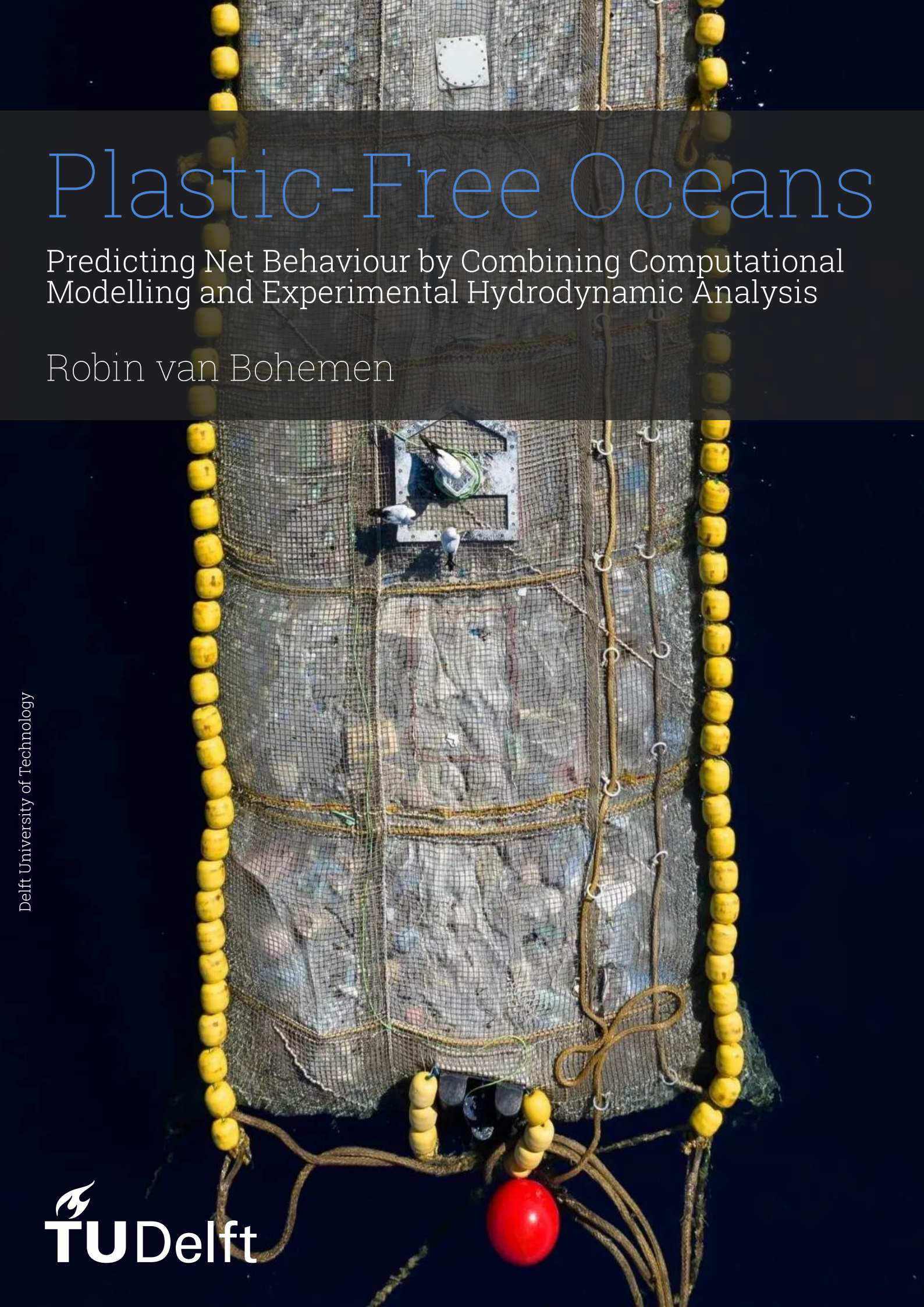

Delft University of Technology

TU Delft

Plastic-Free Oceans

Predicting Net Behaviour by Combining Computational Modelling and Experimental Hydrodynamic Analysis

by

Robin van Bohemen

Student Name	Student Number
Robin van Bohemen	4714695

Chairman of Thesis Committee:	Dr. Ir. J.O. Colomés Gené
University Supervisor:	Dr. Ir. B.C. Ummels
Company Supervisor:	Ir. A.J. Haenen
Company Supervisor:	Dr. Ir. A.D. Rakotonirina
Date:	June 21, 2024
Faculty:	Faculty of Mechanical Engineering, Delft
Study:	MSc. Offshore & Dredging Engineering

TU Delft

mocean ADVANCED OFFSHORE TECHNOLOGY

THE OCEAN CLEANUP

Preface

In a world where one global issue after another fills the front pages, initiatives that provide solutions are more crucial than ever. One such initiative is The Ocean Cleanup. The massive production of plastic has brought many benefits, but a significant portion of this plastic has ended up on beaches or is floating in the oceans, posing a serious threat to marine life. The idea of removing all the plastic waste from the ocean sounds rather simple; however, the execution of this requires a lot of research and engineering. I am honoured to have the opportunity to write my thesis on this subject, and I hope that my research will contribute, even if only slightly, to the steps towards achieving plastic-free oceans.

I would like to express my gratitude to all the members of the graduation committee for their support throughout this process. I want to thank Bart for his supervision of the overall process and for providing positive and valuable feedback during the last nine months. Additionally, I want to thank Anner and Daniel for their guidance and for sharing their critical engineering insights on my project. Finally, I would like to express my appreciation to Oriol for his expertise and constructive feedback during the progress meetings.

Lastly, I would like to thank my colleagues at Mocean Offshore, my family, and my friends for their invaluable support during this final stage of my study.

As of now, they can officially call me an engineer.

Robin van Bohemen
Delft, June 2024

Summary

Plastic has many valuable properties and has become an intrinsic part of our everyday life. An approximated 400 million tonnes is produced every year, consequently, vast quantities of plastic waste find their way into the oceans. The question ”Why don't we just clean it up?” led to the founding of The Ocean Cleanup by Dutch entrepreneur Boyan Slat in 2013.

As of the writing of this thesis, The Ocean Cleanup has removed 12,989,690 kilograms of trash from oceans and rivers. System 03, consisting of two towing vessels towing a large net, is utilised to extract plastic waste from the oceans. To catch as much plastic at minimum time, effort and money, it is essential to have a comprehensive understanding of the behaviour of this net in water. A 3D Finite Element model is employed to simulate the system. Drawbacks in this model are the high computational demand and inaccuracies. These inaccuracies are caused by missing knowledge regarding drag coefficients at low angles of attack and the extrapolation of net behaviour to large nets.

The main objective of this research is to develop a simple, yet accurate model to simulate the physical behaviour of a high length-to-depth ratio net towed through water. Achieving accuracy in the model requires a comprehensive understanding of the net's behaviour in water, which has been investigated through a series of experiments. The simplicity of the model ensures low computational demand, enabling its use in offshore operations for swift decision-making on board. The developed model is validated using measurements obtained from campaigns conducted by The Ocean Cleanup. The performance of this simplified model is then compared to that of the 3D Finite Element model. Finally, the simplified model is applied to predict the behaviour of potential future systems.

In the experiment, the loads on two different nets were measured as they were towed through a basin at various velocities and angles of attack. The results show a significant decrease in drag at low angles of attack, attributed to the shielding effect. Experiments with two-meter and six-meter nets revealed that the shielding effect becomes insignificant beyond these lengths. Consequently, the drag coefficients calculated at various angles of attack for the six-meter net are utilised in the model.

To predict loads on the system, the model estimates the system's shape. For an accurate simulation of reality, the model makes an initial guess on how the system could look like. After this guess, an iteration loop starts until convergence is achieved. Convergence indicates that the system has reached equilibrium, accounting for external influences, internal forces, deformations, and the shape of the system. The model uses system properties, vessel positions and environmental conditions as input to generate the predicted shape of the system and the predicted loads acting on the system.

The performance of the simplified model is assessed by examining the error between the predicted and measured loads under various conditions. This performance is then compared to that of the 3D model. Both models demonstrate accuracy, with a MAE of just over 20%. In the wide-span cases, which occur most frequently in the campaigns, the simplified model performs better than the 3D model. In terms of simulation time, the 2D model significantly outperforms the 3D model. While the 3D model requires approximately one week to complete its simulations, the 2D model finishes in 0.14 seconds, making it a flexible and user-friendly option. Altogether the simplified model is a simple, yet accurate model to simulate the physical behaviour of a high length-to-depth ratio net towed through water.

To demonstrate the model's functionality, it is applied to one of the trips, showing the maximum sailing velocities to ensure the system remains within its limits. The same trip is then simulated using potentially new nets and increased sailing velocities, resulting in a higher plastic catch. To improve the model's accuracy, aspects like wave direction, wind speed and wind direction can be implemented. Additionally, conducting a CFD analysis is recommended to gain a deeper understanding of net behaviour, which can help avoid the expense of additional tank tests.

Contents

List of Figures

List of Tables

Nomenclature

Abbreviations

Abbreviation	Definition
AoA	Angle of Attack
CAPEX	Capital Expenditures
CFD	Computational Fluid Dynamics
GPGP	Great Pacific Garbage Patch
HDPE	High Density Poly-Ethylene
DT	Digital Twin
KPI	Key Performance Indicator
MAE	Mean Absolute Error
MAPE	Mean Absolute Percentage Error
MARIN	Maritime Research Institute Netherlands
OPEX	Operating Expenditures
PDF	Probability Density Function
PSD	Power Spectral Density
RMSE	Root Mean Square Error
STW	Speed Through Water

Symbols

Symbol	Definition	Unit
A	Area	[m^2]
a	Wave amplitude	[m]
C_D	Drag coefficient	[-]
C_L	Lift coefficient	[-]
d	Depth	[m]
d_w	Twine diameter	[m]
E	Young's Modulus	[Pa]
F	Force	[N]
f	Frequency	[Hz]
H_s	Significant wave height	[m]
k	Wave number	[m$^-1$]
l	Length	[m]
L_m	Mesh size	[m]
Re	Reynolds Number	[-]
S_n	Solidity	[-]
S_{max}	Maximum wave steepness	[-]
T	Tension	[N]
T_p	Wave period	[s]
u	Particle velocity	[m/s]
v	Velocity	[m/s]
α	Angle of attack	[degree]
ϵ	Elastic elongation	[-]
η	Dynamic viscosity	[N s/m^2]
λ	Wave length	[m]

Symbol	Definition	Unit
ν	Kinematic viscosity	[m^2/s]
ρ	Density	[kg/m^3]
ϕ	Mesh angle/Orientation	[degree]
ω	Angular frequency	[s^-1]
θ	Angle of attack	[degree]

1 Introduction

To provide an understanding of the purpose of this research, the problem of plastic pollution is introduced in Section 1.1, followed by an introduction to The Ocean Cleanup in Section 1.2, an organisation dedicated to developing solutions to this problem. The research framework is discussed in Section 1.3, outlining topics covered in this thesis. Based on this framework, the problem statement is presented in Section 1.4. The objective and research questions of the thesis are detailed in Section 1.5. Finally, the methodology for achieving this objective is described in Section 1.6.

1.1. Plastic Pollution

Plastic has many valuable properties and has become an intrinsic part of our everyday life. An approximated 400 million tonnes is produced every year (OECD, 2022), some of which eventually ends up in our environment. Consequently, vast quantities of plastic find their way into the oceans annually. In 2023, an estimated 171 trillion pieces were floating around at sea (Eriksen et al., 2023). Most of this plastic eventually beaches on coastlines, posing serious consequences for coastal environments and communities. The remaining plastics stay afloat much longer. The long lifespan of plastics, supposedly one of its best properties, results in large amounts of plastic waste floating around for years where they persist, gradually degrading into micro-plastics. Items like bottle caps drift into the open ocean, gathering in gyres, large rotating currents driven by wind and the Earth's rotation, as shown in Figure 1.1. The largest accumulation occurs in the Great Pacific gyre, commonly known as the Great Pacific Garbage Patch (GPGP). The question 'Why don't we just clean it up?' (Slat, 2012) kept lingering in the mind of Dutch entrepreneur Boyan Slat, which resulted in the founding of The Ocean Cleanup in 2013 at the age of eighteen.

As of the writing of this thesis, The Ocean Cleanup has removed 12,989,690 kilograms of trash from oceans and rivers. Although it is challenging to determine the exact amount of plastic waste leaking into rivers and coasts, recent research from 2023 estimates it to be around six billion kilograms (Ritchie, 2023). The Ocean Cleanup is actively developing various methods to extract this waste from our oceans and rivers.

Figure 1.1: Schematic overview of the five rotating currents, called gyres, where floating plastic accumulates (Slat, 2014)

1.2. The Ocean Cleanup

To protect the environment, Boyan Slat founded *The Ocean Cleanup* in 2013 with the goal:

To reach 90% reduction of floating ocean plastic by 2040 (The Ocean Cleanup, n.d.)

Achieving the stated goal requires the integration of two actions. On the one hand, the plastic supply into the oceans needs to be stopped. On the other hand, the plastic that is already in the ocean needs to be extracted. The Ocean Cleanup operates in various locations worldwide, employing diverse systems to clean up as much marine debris as possible as soon as possible. Looking at the inflow of marine debris it makes sense to state that the top priority should be preventing plastics from entering the ocean, leaving the plastic already there just floating around for now. However, due to UV radiation, chemical degradation, wave mechanics, and grazing by marine life, large, floating pieces of plastic will degrade into smaller pieces. Because of the long time it takes for plastics to decompose, there is enough time to degrade into microplastics (<5 mm) (Van Sebille et al., 2015). The problem with these microplastics is that they are harmful to marine life due to ingestion, besides that, the smaller the fragments, the more challenging to clean up. Therefore, both cleaning up the oceans and stopping the plastic supply into the oceans, are part of the goal of The Ocean Cleanup.

To stop the plastic supply into the oceans, The Ocean Cleanup deployed their first 'Interceptor' in the Cengkareng Drain in Indonesia in February 2019. This first interceptor functions as a barrier in the river, helping reduce plastic leaking into the ocean. In the following years, The Ocean Cleanup developed and deployed multiple types of Interceptors in the world's most polluting rivers. For the other part of the mission, The Ocean Cleanup developed a large system that operates in the oceans to extract the plastics that are already there. Figure 1.2 shows System 03, consisting of two towing vessels, a large net and a retention zone in the back of the U-shape.

Figure 1.2: Drone shot of The Ocean Cleanup System 03

The Ocean Cleanup's system to clean the oceans consists of two vessels towing a 2150-meter-long floater. A 4-meter deep net, connected to the floater, functions to accumulate floating plastics in the back of the U-shaped system. Here, the retention zone is located to collect all the plastics. The floaters on both sides of the retention zone are called the wings and are connected by towing cables to the vessels. During the transition from System 002 to System 03, the installation of multiple wing modules results in a full-size net extending over two kilometres, as depicted in the schematic view illustrated in Figure 1.3a. The system is towed through water at a sailing speed varying between 0.5 and 1.0 m/s. This slow speed ensures that bycatch during operations is minimised. Additionally, diverse techniques are integrated into the system. To warn fish, turtles and other animals, the system produces a high-frequency sound and incorporates green LED lights to indicate its presence. Additionally, cameras are installed in the retention zone for visual inspection. Three large bottom holes serve as escape routes

and there is access to air for trapped animals. As a last resort, an emergency release is installed, freeing a potentially trapped animal, including the plastic within the retention zone.

In the specific case of The Ocean Cleanup, an organisation that supports the preservation of marine ecosystems and is completely funded by donations, the main drivers translate into the following two Key Performance Indicators (KPI's) (Jiménez et al., 2023):

- The costs in euros per kilogram of extracted plastic
- The CO_2 emission in tonnes per tonne of extracted plastic

The Ocean Cleanup is committed to making efficient use of the obtained donations, as stated in the first KPI, and aims at minimising environmental impact in operations, as stated in the second KPI. To do this as efficiently as possible, the understanding of hydrodynamic loads acting on its cleanup systems, influencing CO_2 emissions and costs, becomes essential. In order to reach the stated goal, expansion of the fleet or extension of the size of the systems is crucial, making the understanding of hydrodynamic loads on the systems even more imperative.

1.3. Research Framework

Based on extensive literature research including various papers and interviews and discussions with experts, the knowledge gaps have been identified. These knowledge gaps provide the basis of this thesis in the problem statement.

Load Predictions

By the usage of a plastic dispersion model in combination with weather forecasts, the optimal sailing route of the vessels is determined. External factors such as severe weather forecasts or regions with low plastic densities could change the steering strategy of the operation quickly. Throughout the operations, the forces exerted on the system must stay within the load limits of 71.25 tonnes at all times to prevent the system from failure. In order to make predictions on the behaviour of the system, The Ocean Cleanup is using a 3D Finite Element model in OrcaFlex. OrcaFlex is a software program used for dynamic analysis of offshore marine systems. A top view of System 03 in OrcaFlex is shown in Figure 1.3b. More detailed information about the functioning of the model is provided in Chapter 4.

Net Behaviour

Despite millennia of practical experience in the usage of nets and the passing down of techniques from generation to generation, there are still aspects of net behaviour in water unknown which makes this research even more interesting and fundamental. To gain knowledge on this net behaviour, the fishing industry has conducted various experiments and studies on net properties and net behaviour in water. Most experiments in this field involve small net panels with a length-to-depth ratio of 1. As a result, the understanding is limited when it comes to extrapolating the behaviour observed in a net with a length-to-depth ratio of 1 to that of a net with a ratio exceeding 500. The initial twine of the net may influence the local current, subsequently impacting the effect of the current on the second twine. The hypothesis posits that the current is altered in a manner that leads to a decrease in drag for the subsequent twines. However, the extent to which this occurs is currently unknown.

Drag Factors

Determining drag factors on net panels placed perpendicular to incoming flow is investigated and validated in different studies. However, determining drag factors on long nets, in different angles of attack is still fairly unknown in the literature. Studies are looking into net panels under an angle of attack and concluding that the drag on the net panel is dependent on the angle of attack. Exploring the expected rise in drag at higher angles of attack is an intriguing area of investigation. This involves examining the magnitude of the increase and determining its applicability when extrapolated to the entire system.

System Configurations

Missing knowledge on net behaviour also causes a problem for the 3D model of System 03 that The Ocean Cleanup is using at the moment. When it comes to a wide-span configuration of the system, meaning a large distance between the towing vessels, which governs perpendicular flow on the net,

the model's calculation of the total system drag closely aligns with real-life measurements from the GPGP. For a small span, meaning that parts of the net are at small inclination angles relative to the incoming flow, the model turns out to be too conservative by showing higher forces than the real-life measurements. This means something happens here that is not taken into account in the model. For example, the shielding effect could cause this deviation from the model results. The influence of one twine onto the next one may change the drag and with that the drag coefficients on small angles of attack. Other options for deviating measurements are of course due to deviating environmental conditions like current, waves or wind that can deviate from reality in the model.

Computational modelling

Modelling a net of two thousand by four meters contains an enormous amount of parts, even in simplified form. The result is that every calculation or simulation takes a lot of time and demands high computational power. A more simplified model of the system that is able to calculate system properties in different configurations does not exist yet. A model like this would be very valuable for the organisation enabling quick calculations on the net for decisions on steering strategy for example. This model would facilitate easy determination of routes and provide insights into the forces acting on both the net and the towing vessels.

Scientifical and Practical Contribution

This research makes a practical contribution to The Ocean Cleanup and enhances scientific understanding of nets in water. The Ocean Cleanup's goal of a '90% reduction of floating ocean plastic by 2040' can only be achieved if the organisation is ready to scale up. A crucial prerequisite for scaling up is understanding the system's behaviour, according to Marceau Phillipe-Janon from the Hydrodynamics team at The Ocean Cleanup (Philippe-Janon, 2023). Accurately predicting the system's behaviour enables improvements, expansions, and multiplications of the system, bringing the organisation closer to its ultimate goal.

In addition to facilitating scaling up and advancing The Ocean Cleanup's mission, this research holds scientific value by investigating the shielding effect and exploring the relationship between net behaviour and different length-to-depth ratios. A better understanding of net behaviour in water can lead to more efficient net usage across various industries.

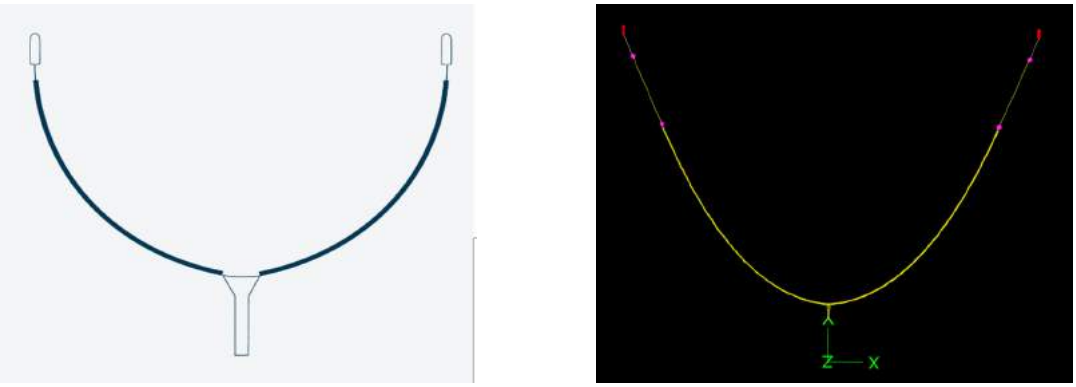

(a) Schematic view (The Ocean Cleanup, n.d.) **(b)** 3D Finite Element model

Figure 1.3: Top view of System 03

1.4. Problem Statement

Systems that The Ocean Cleanup is working with are the first in the world with this specific configuration, which means there is little literature available on the exact properties of these systems. This finding was confirmed by Yannick Pham, Steering Strategy Manager at The Ocean Cleanup (Pham, 2023). This forces the organisation to look into a comparable industry, working with sort of comparable materials: the fishing industry. In a way, both the fishing industry and The Ocean Cleanup share similar

goals: extracting objects or fish from the water in an efficient way.

To summarize the problems as introduced in the research framework, the three main problems are:

- Missing knowledge on the behaviour of nets in a current under small inclination angles. What is the influence of shielding and how does that affect the drag coefficients?
- Missing knowledge on how to extrapolate the behaviour of small net panels to a net with a high length-to-depth ratio. Can the forces just be multiplied or does the ratio influence the behaviour?
- Modelling a net in 3D takes a large number of elements and therefore a calculation or simulation demands high computational power. How does a model that can be used for quick but accurate calculations look like?

Further research should investigate the influence of the angle of attack of incoming flow on a net, the impact of the system's high length-to-depth ratio, and methods to model net behaviour without excessive computational demand.

1.5. Objective & Research Question

The main objective of this research is to develop a simple, yet accurate model to simulate the physical behaviour of a high length-to-depth ratio net towed through water.

To reach this objective, the following research question is defined:

What is the physical behaviour of a high length-to-depth ratio net towed through water?

To answer this main research question, the following sub-questions have been defined:

1. *What is the drag coefficient of a flat net panel of a high length-to-depth ratio net?*
2. *How can drag coefficients for net panels be quantified experimentally?*
3. *What is the influence of the inclination angle of a net panel on the drag coefficient?*
4. *How can experimental results on flat net panels be extrapolated to full-size nets?*
5. *How can the physical behaviour of a high length-to-depth ratio net be accurately captured in a fast-running computational model?*
6. *How can measurement data be used to validate the performance of the computational model?*

Besides the importance of the accuracy of the developed model, it is also important to make it as simplified as possible, without compromising its accuracy. Simplification helps keep computational demands and computing time low. This is essential for using the model as a tool for swift decision-making, such as determining steering strategies. While a more complex tool with higher computational demands may be suitable for detailed predictions during operation preparation and system design, a quick and accurate tool is indispensable for making rapid decisions during real-life offshore operations. Additionally, the model needs to be robust which means it can predict loads in all kind of situations and present the errors with the measured loads.

1.6. Methodology

The approach to answer the research questions and to attain the main objective involves a series of several connected stages, which are:

- Literature Phase
- Experimental Phase
- Modelling Phase
- Integration & Validation Phase

Given the inherent uncertainty of experiments, redundancy has been incorporated into the project design. By implementing four stages, delays caused by postponements or adjustments in the experiments can be mitigated. Additionally, the Experimental Phase and the Modelling Phase can be conducted concurrently, providing a flexible working methodology.

Literature Phase
Prior to this thesis, an extensive literature review is conducted to determine the existing knowledge gap on the topic and to formulate the problem statement. In addition to the available literature, interviews are arranged with various experts at The Ocean Cleanup. These interviews involve discussing the experts' knowledge of the topic, identifying information gaps, and determining what additional research would be valuable for their organisation. The conclusion of the Literature Phase is the Literature Review which defines the knowledge gap and the Research Plan used for this thesis. A summary of this literature review is presented in Chapter 2.

Experimental Phase
Together with The Ocean Cleanup, an experiment will be set up to get a comprehensive understanding of the net behaviour in operation. The goal is to contribute to solutions to the, in Section 1.4 mentioned problems. Experiment results can be used to investigate the influence of different nets in various currents under various inclination angles. Additionally, the knowledge on extrapolation of small net panels to high length-to-depth ratio nets can be researched.

Modelling Phase
Independent of the experimental phase, a simplified model will be developed in the Modelling Phase. As mentioned in Section 1.4, one of the problems is that the current 3D model has a very high computational demand which makes it impossible to do quick calculations using this 3D model. To do estimations on net behaviour and forces on the system during operation, a model with lower computational demand would be useful. This model will make it possible to combine real-life environmental data, like current and wave information, with steering strategy decisions to estimate the behaviour and forces of the system on the spot.

Integration & Validation Phase
In the final phase, the Integration & Validation Phase, all work will be combined to answer the research question. In this phase, the gathered data from the experiment will be implemented into the model. The drag factors at different inclination angles and the knowledge of extrapolation of small net panel behaviour can be used in the model to improve the accuracy and to get results as close to reality as possible. After integrating the experimental results into the 2D model, it is essential to validate the model to assess its accuracy. Real-life measurements from recent campaigns in the Great Pacific Garbage Patch will be utilised for this purpose. This data includes information such as vessel positions, current speeds, wave heights, and loads on the winch connected to the net. Signals like vessel positions and environmental conditions will serve as input for the model. The model's generated output will be compared with measured winch loads to determine its performance. Similar validation steps will be carried out for the 3D model. Ultimately, both models will be compared based on accuracy, usability, and simulation time.

Figure 1.4 shows how the sub-questions are divided over the four phases.

	Literature Phase (H2)	Experimental Phase (H3)	Modelling Phase (H4)	Integration & validation Phase (H5)
1. What is the drag coefficient of a flat net panel of a high length-to-depth ratio net?	X	X		
2. How can drag coefficients of net panels be quantified experimentally?		X		
3. What is the influence of the inclination angle of a net panel on the drag coefficient?		X		
4. How can experimental results on flat net panels be extrapolated to full-size nets?		X		
5. How can the physical behaviour of a high length-to-depth ratio net be accurately captured in a fast-running computational model?			X	
6.How can measurement data be used to validate the performance of the computational model?				X

Figure 1.4: Division of sub-questions over the four phases

1.6.1. Report Outline

This research starts with a literature framework regarding net properties and net behaviour in Chapter 2. This second chapter dives into theory on net behaviour and on conducting experiments to partly answer the first sub-question. Chapter 3 introduces the experiment conducted at MARIN and presents the outcomes. This experiment contributes to answering the first four sub-questions. Next, Chapter 4 explains the developed model and treats various aspects of the model, answering sub-question 5. The experiment results and the model are combined in Chapter 5 in which the model is validated using measurement data, answering sub-question 6. Subsequently, the model is applied to real-life situations in Chapter 6. Followed by a discussion, conclusions and recommendations for further research in Chapter 7, Chapter 8 and Chapter 9, respectively.

2

Literature Framework

Besides their use in extracting plastics from the ocean, nets have a long history of wide-ranging applications. In 1914 a remarkable archaeological find was made in Finnish territory called the 'Antrea Net Find'. In this find, multiple tools and a Stone Age fishing net are found, dated to around 8400 B.C. (Miettinen et al., 2008). Nets in that time were made of shavings of wood woven into chords and they were used for fishing. This was the start of fishing nets which evolved to all different kinds of nets used in fishery nowadays, like prawn trawls, fishing cages, and drag nets made from different materials.

As stated in (Tang et al., 2018), Reynolds number, solidity ratio, inclination angle, knot type, and twine construction all contribute to the characteristics of a certain net configuration. In this chapter, after the introduction of net properties in Section 2.1 and experiment locations in Section 2.2, these hydrodynamics will be investigated. First, the dimensionless Reynolds number will be discussed in Section 2.3. Next, the drag coefficient will be addressed in Section 2.4 followed by a section about the deformation of nets in Section 2.5. Lastly, the influence of solidity and the influence of shielding will be elaborated on, this is shown in Section 2.6 and Section 2.7, respectively.

2.1. Net Properties

Mesh size

In the context of nets, the mesh size, denoted as L_m, represents the distance between the two centerlines of two adjacent twines, as shown in Figure 2.1. A large mesh size means there is low drag on the net, but it also allows small objects to flow through it. Smaller mesh sizes can effectively filter out the smallest objects in water, but this comes at the cost of increased drag forces.

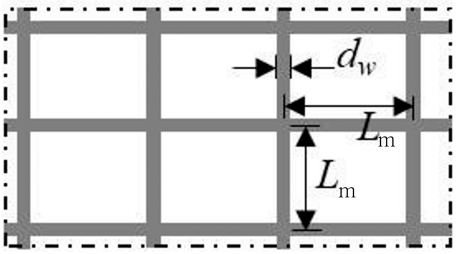

Figure 2.1: Definition of mesh size (L_m) and twine diameter (d_w) (Cheng et al., 2020)

Mesh shape

The way the twines are arranged relative to each other determines the mesh shape. The most standard configuration of the twines is all twines perpendicular to each other. This way of netting results in a pattern of squares as shown in Figure 2.1. A more traditional method of fabricating nets involves arranging twines at a 45° angle, resulting in a diamond mesh. Other less frequently used mesh shapes

are unequilateral, hexagonal, tetragonal, or diamond-shaped and squared combined, all shown in Figure 2.2. The decision for a certain mesh size and mesh shape depends on the function of the net. A soccer goal net is sufficient if the diamond mesh size is small enough to prevent the ball from passing through. To filter microplastics from the sea, one might consider a very small mesh size and a square mesh shape to extract the small plastics in all possible shapes. Traditionally, diamond mesh is used for fishing, while The Ocean Cleanup has chosen to use square mesh. Matt K. Broadhurst explains this choice with his experiment in which he proves that the catch rate for, in his case prawns, is higher for diamond mesh, compared to square mesh (Broadhurst et al., 2004).

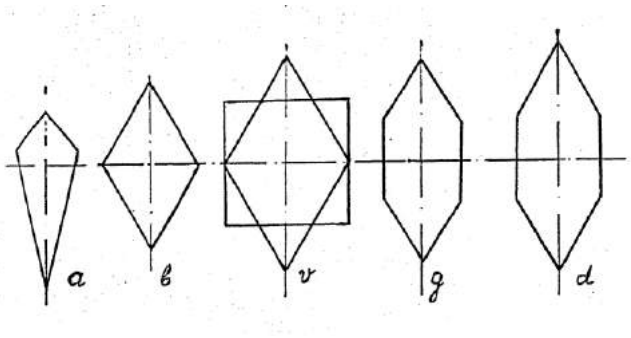

Figure 2.2: Mesh shapes: (a) unequilateral, (b) diamond-shaped, (v) diamond-shaped and square, (g) hexagonal, (d) hexagonal (Shevtsov, 1988)

Twine diameter

A net consists of a pattern of woven ropes called twines. The diameter of these twines, d_w, influences the strength of the net, the stiffness of the net, and the solidity. Firstly, a larger twine diameter results in the pulling force on a net being distributed over a larger area, thereby increasing the maximum pulling strength of the net. A horizontal pulling force on the net is distributed over all horizontal twines of the net. Secondly, a larger twine diameter provides more resistance to the deformation of the net, contributing to its stiffness. Moreover, the solidity increases with a larger twine diameter, more details on this aspect can be found in the next paragraph.

Solidity

An often-used variable that characterizes hydrodynamic performances is the solidity S_n. The solidity is the ratio of the projected area by the net A_p normal to the net panel to the outline area of the entire net panel A (Castellano et al., 2008):

$$S_n = \frac{A_p}{A} \tag{2.1}$$

For a basic square mesh, the solidity is given by:

$$S_n = \frac{2L_m d_w - d_w^2}{L_m^2} \tag{2.2}$$

Where L_m is the mesh size and d_w represents the twine diameter. In cases where a diamond-shaped net is used, the solidity also depends on the mesh angle ϕ, as shown in Figure 2.3 (Zhou et al., 2015). In this case Equation 2.2 changes into

$$S_n = \frac{2L_m d_w - d_w^2}{L_m^2 \sin(2\phi)} \tag{2.3}$$

Together with the inclination angle of the flow on the net panel, the solidity influences the drag coefficient by increasing the area that blocks the incoming flow (Tsukrov et al., 2011). More information on how the inclination angle influences the drag coefficient can be found in Section 2.7.

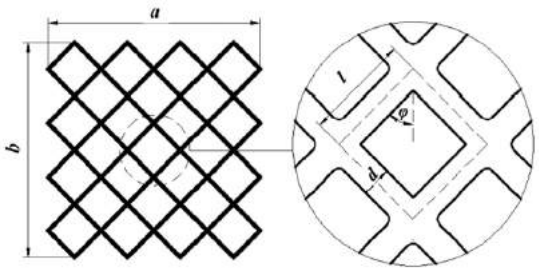

Figure 2.3: Geometric parameters for a typical diamond netting (Zhou et al., 2015)

Inclination angle

The most basic way to determine the drag coefficient by experiment is by positioning a net panel perpendicular to the incoming flow. The inclination angle is defined as the angle between the net panel and the incoming flow, so, in this case, the inclination angle is 90 degrees. By varying the inclination angle relative to the incoming flow, a shielding effect can occur which causes variations in the drag factor. The shielding effect is caused by the influence of one twine on the flow reaching the second twine, in turn, influencing the flow to the next twine. More on this can be found in Section 2.7.

Knotting

In Figure 2.4 a clear difference between different types of knotting is shown. In the left picture, one can see a knotless way of weaving nets whereas in the right picture, the single English knot is used to connect the twines of the net. This knotting influences the solidity and with that the drag on the system. Hao Tang compared the two nets from Figure 2.4 and concluded that the drag coefficient of the knotted net was $1.23 \sim 1.35$ times greater than the drag coefficient of the knotless netting, which means knotting could influence the hydrodynamics of netting (Tang et al., 2018).

Figure 2.4: Experimental samples of knotless nylon (polyacrylamide or PA) netting (left, four-strand braid) and knotted nylon netting (right, single English knot) (Tang et al., 2018)

Materials

In 2009, the most commonly used material in the aquaculture industry for nets was nylon (Balash et al., 2009). In recent years, the aquaculture industry has seen the adoption of innovative net materials such as Dyneema, nylon monofilament, Hampidjan Dynex, and Euroline Premium Plus (Balash & Sterling, 2012). Every material has its own influence on the hydrodynamics of the net by varying density and varying surface structure. These properties can influence the incoming flow and with that the drag or dynamics of the net.

The Ocean Cleanup netting

The net material used by The Ocean Cleanup is Dyneema. Dyneema is a material that combines high strengths with low weights and is therefore very suitable for The Ocean Cleanup. These knotless nets are constructed from a robust polyethylene fiber. Another advantage of Dyneema is that it requires less antifouling compared to nylon nets, making it a more eco-friendly option. The used twine diameter in the net of System 03 is 1.5 millimeters and the mesh size is 16 millimeters which results in a solidity of 0.179. The weaving of the net is knotless and as mentioned, the mesh of the net has a square shape.

2.2. Experiments

To determine the mentioned net properties or to validate models that simulate net behaviour, experiments can be conducted. Two types of test facilities for doing net experiments in water are the flume

tank and the towing tank.

2.2.1. Flume Tank

'By definition, a flume tank is an artificial channel or chute carrying a stream of circulated water and is analogous to a wind tunnel.' (Moret & Legge, 2014). Simply said: a fluid flows through a basin or channel along a fixed object. Flume tanks serve as research tools for conducting experiments on hydrodynamical processes and come in different configurations. Some are designed for freshwater, some for seawater; some are temperature controlled, some are laboratory facilities and some can be used in the field. Also, the shape of the flume tank varies per tank, with four different configurations shown in Figure 2.5 (Jonsson et al., 2006). Each flume tank configuration is suitable for specific research questions. Within a flume tank, water is circulated using pumps or propellers and crosses the test section with a certain current velocity. The test section is the part where the test setup is observed and where the measurements are conducted under controlled conditions. In a flume tank experiment, an object can be secured within the tank while a current is passed through it. During this process, measurements can be taken to assess the forces acting on the object or to analyse any deformations it may undergo. Examples of net-experiments in flume tanks are stated in (Madsen et al., 2011), (Thierry et al., 2020), (Stewart & Ferro, 1985) and (Bouhoubeiny et al., 2014).

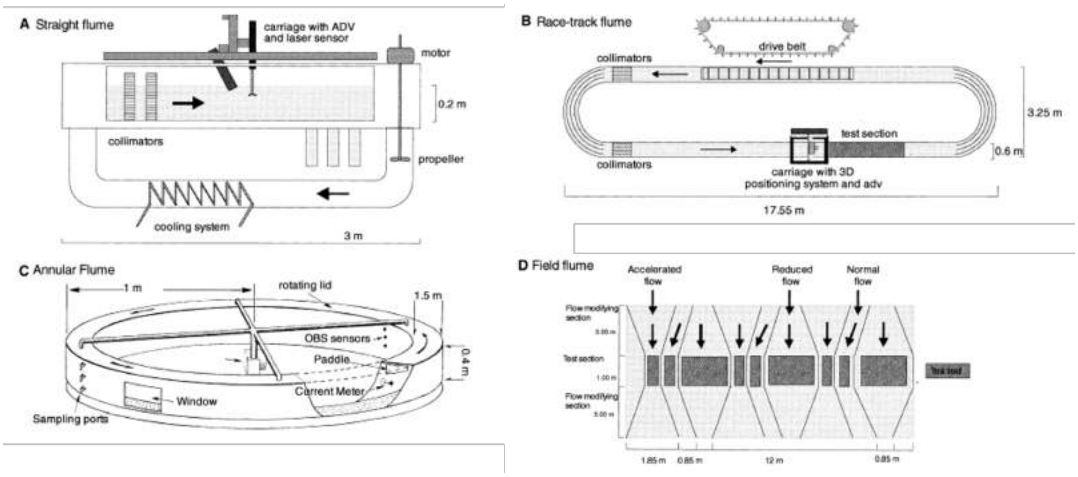

Figure 2.5: Schematic overview of four types of flume tanks. (A) Straight flume, (B) Race-track flume, (C) Annular flume, (D) Field flume (Jonsson et al., 2006)

2.2.2. Towing Tank

Instead of pumping a fluid through a flume tank, it is also possible to tow or propel an object through a basin filled with water. This is done in a test setup called the towing tank. By using a towing tank, hydrodynamic behaviour can be studied. One clear advantage of using a towing tank, as opposed to a flume tank, is the reduced energy demand. Moving a model through a fluid requires much less power than pumping a large volume of water past a stationary model. Other advantages include the ability to easily vary the velocity of the model through water and adjust the direction of the model, making it suitable for simulating manoeuvring vessels (Gad el Hak, 1987). However, towing tanks do have their disadvantages, such as vibrations of the carriage and limitations in running time due to the finite length of the basin. Towing tanks are not limited to the study of boat and ship hydrodynamics; they are also employed to study the aerodynamics of bodies like wings or blades. In a towing tank, it is, compared to a wind tunnel, easier to produce arbitrary velocity profiles by using electric motors instead of moving a bulk of fluid. Additionally, the kinematic viscosity of water is smaller which makes it possible to test with higher Reynolds numbers at lower velocity (Jentzsch et al., 2021). In Figure 2.6 the towing tank of Technische Universität Berlin is shown, comprising a water basin with a length of 250 m, a width of 8 m and a depth of 4.8 m, along with a carriage train that moves along two rails lining the basin's walls. As mentioned, in towing tank experiments, the test object is towed through water. Throughout this process, measurements can be acquired to assess forces acting on the object, and any resulting de-

formations can be observed, just as in flume tank experiments. Examples of towing tank experiments are stated in (Patursson et al., 2010), (Shimizu et al., 2018), (Swift et al., 2006) and (Kristiansen et al., 2015).

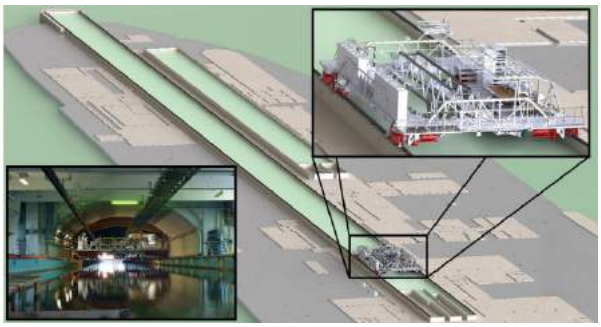

Figure 2.6: Towing tank and towing carriage at TU Berlin (Jentzsch et al., 2021)

2.3. Reynolds Number

One of the most important numbers in microfluidics is the Reynolds number. The Reynolds number is a dimensionless number that is used to describe the relationship between inertial forces and viscous forces. This means that the Reynolds number helps in describing the transport properties of a particle with inertia moving in a fluid. The first time the number is described is in 1883 (Reynolds, 1883). The Reynolds number is defined as

$$Re = \frac{inertia forces}{viscous forces} = \frac{\rho * v * d_w}{\eta} = \frac{v * d_w}{\nu} \tag{2.4}$$

In this equation ρ is the density of the fluid in [kg/m^3], v is the incoming velocity of the fluid in [m/s], d_w the twine diameter in [m], η the dynamic viscosity in [Ns/m^2] and ν as kinematic viscosity [m^2/s].

As can be seen in the equation, a very low Reynolds number implies that viscous forces dominate over inertial forces. As an example, a small, folded paper boat has a low Reynolds number which results in that it will not be able to force its way across the streamlines of the fluid. A large vessel with Reynolds numbers of about $1 * 10^9$ has enough inertia to move its way through the streamlines of the fluid (Rapp, 2017).

When considering different twine diameters in nets, ranging from one millimeter to one centimeter, and mesh sizes varying from one centimeter to one meter, the typical Reynolds number range will be $10^2 - 10^4$ (Fredheim, 2005). For The Ocean Cleanup System 03 net with a twine diameter of 1.5 millimeters, a kinematic viscosity of 0.01341 cm^2/s (Zou et al., 2022) and current speeds varying between 0.5 m/s and 2.0 m/s, the Reynolds number will vary within the range of approximately 500 to 2300.

2.4. Drag Coefficient

The dimensionless quantity 'drag coefficient', C_D, is used to quantify the amount of drag or resistance an object has in a medium like water or air. A high drag coefficient indicates a significant hydrodynamic or aerodynamic resistance. The drag coefficient is dependent on various variables, including the object's surface area and its velocity relative to the fluid. Determining the drag coefficients is done by measuring the drag force F_D in an experiment where the object is exposed to an incoming flow. The function of the particular drag force is given by:

$$F_D = \frac{1}{2}\rho A C_D v^2 \tag{2.5}$$

From this equation, the drag coefficient can be computed:

$$C_D = \frac{2F_D}{\rho A v^2} \tag{2.6}$$

Where F_D is the measured force in [N], ρ the density of the fluid in [kg/m^3], A the frontal area of the object in [m^2] and v the velocity of the fluid in [m/s] (Niño et al., 2020).

In an experimental setup, the net panel can be placed in a perfect perpendicular angle relative to the current. However, in many cases, like in The Ocean Cleanup systems, most of the time, the angle of attack of the flow relative to the net panel is not perpendicular to the free stream velocity. As a result, the total drag force can be decomposed into the normal drag force F_D, n and the tangential drag force F_D, t, often referred to as the lift force F_L:

$$F_D, n = \frac{1}{2}\rho A C_D v_n^2 \tag{2.7}$$

$$F_D, t = \frac{1}{2}\rho A C_t v_t^2 \tag{2.8}$$

V_n is the velocity component normal to the net panel and v_t is the velocity component parallel to the net lines. This is visualised more clearly in Figure 2.7 (Zhan et al., 2006).

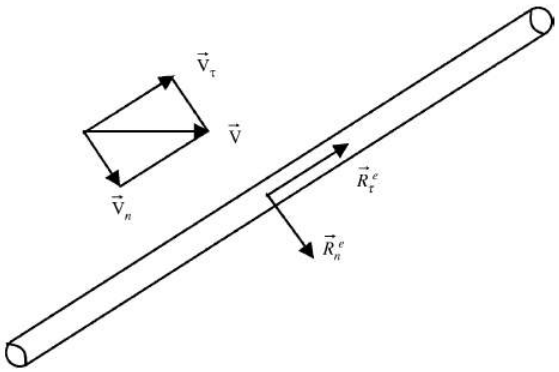

Figure 2.7: Drag force components on net line (Zhan et al., 2006)

The drag factor used in The Ocean Cleanup's 3D OrcaFlex model is based on (Naumov et al., 2013). The formula used for the calculation of the drag coefficient for flat netting in perpendicular flow is:

$$C_D = A * \left(\frac{2 * S_n}{Re}\right)^n \tag{2.9}$$

However, this equation is only correct in a certain range of Reynolds numbers. Because the drag coefficient cannot be accurately described by a single formula across all Reynolds numbers, Naumov conducted an experiment to establish different areas and critical Reynolds numbers (Re_L and Re_K). This approach allows for more precise calculations of the drag coefficient as a function of Reynolds number and solidity, resulting in the following equation (Jiménez et al., 2023):

$$C_D = \begin{cases} 19.4 * \left(\frac{2*S_n}{Re}\right)^{0.36}, & Re < 400 * S_n \\ 9.3 * \left(\frac{2*S_n}{Re}\right)^{0.22}, & 400 * S_n \leq Re < Re_K \\ 1.41 + 1.70 * S_n, & Re \geq Re_K \end{cases} \tag{2.10}$$

$$Re_K = 2S_n \left(\frac{9.33}{1.41 + 1.7S_n}\right)^{4.63} \tag{2.11}$$

Applying this to The Ocean Cleanup System 03 net with a solidity of 0.179 and current velocities of 0.5 m/s and 2.0 m/s, Re_K equals 913. At 0.5 m/s, the Reynolds number is approximately 550, placing the drag coefficient in the middle range of Equation 2.10. At 2.0 m/s, the Reynolds number increases to around 2200, requiring the use of the third row in Equation 2.10 to determine the drag coefficient. This means for these net properties, the drag coefficient formula shifts from the second to the third row of Equation 2.10 at a current velocity of about 0.82 m/s.

2.5. Deformation

The result of an incoming current on a net is tension distributed over the twines of the net. The incoming current interacts with the net, causing it to deform into a specific shape, such as the catenary curve when the net is fixed between two endpoints. The tension in the twines could also lead to an elongation of the material. The relationship between the elastic elongation of the twines and the tension in the twine is given by Equation 4.6 (Wu & Cao, 2016).

$$\varepsilon = \frac{l - l_0}{l_0} = \frac{T}{EA} \tag{2.12}$$

In this equation is ε the elongation of the twine, l_0 the initial length of the twine [m] and l the deformed length [m], T the tension force in the twine [N], E the Young's Modulus [Pa] and A the area of the twine calculated by the nominal diameter [m^2]. The Young's Modulus is dependent on the type of material and indicates to what extent the material deforms. For steel E is around 200 GPA, for polyethylene around 1 GPA, and for Dyneema, the material that is used at The Ocean Cleanup, E is approximately 109 - 132 GPA (Sanborn et al., 2014). With a measured tension in the GPGP of about 1 MN spread over 250 twines (4 meter deep net with a mesh size of 16mm) with a twine diameter of 1.5mm and a Young's Modulus of about 110GPA, a rough estimation of the elongation of the net will be around two centimetres. This elongation is very small compared to a total length of 2000 meters and therefore negligible.

2.6. Influence of Solidity

As mentioned in Section 2.1, the solidity of the net is the ratio between the projected area by the net normal to the net plane to the outline area of the entire net panel. This means that the higher the solidity ratio, the lower the flow through the net is, and intuitively, the higher the drag coefficient when positioned perpendicular to the incoming flow. However, when the net panel is placed parallel to the incoming flow, the opposite occurs. In general cases, the higher the solidity ratio, the lower the drag coefficient.

To illustrate the impact of solidity ratio on drag, consider high-speed cyclists that are using closed rear wheels when riding a time trial for example. The closed wheel causes less disturbances in the incoming flow which makes them more aerodynamic. The benefits of this closed rear only work if the wheel is placed perfectly parallel to the incoming flow. Therefore, cyclists do not use a closed front wheel, because this wheel is used for steering. On top of that, it is prohibited to use closed front wheels because of the increased instability due to the large area catching a lot of wind. To still reduce the drag as much as possible, the solidity ratio is increased by increasing the height of the rims. As Zdravkovich proved in his paper published in 1992, the use of splitter plates inhibits the vortex shredding and with that, reduces the drag coefficient (Zdravkovich, 1992).

Figure 2.8: High-speed cycling with aerodynamic wheels (Colless, 2019)

In combination with the solidity ratio, the Reynolds number influences the drag on a panel. In the two graphs shown in Figure 2.9, one can see the drag coefficient as a function of the Reynolds number in two cases: incoming flow normal to the panel (left) and incoming flow parallel to the panel (right). Again, the fact is shown that the higher the solidity ratio, the higher the drag when the inclination angle is 90 degrees (panel perpendicular to the flow), and the higher the solidity ratio, the lower the drag, when

the inclination angle is 0 degrees (panel parallel to the flow) (Tang et al., 2017). A second interesting aspect of the graphs is the observation that the drag coefficient decreases at higher Reynolds numbers, particularly when looking at the left graph with the net panel perpendicular to the incoming flow. These results are confirmed by the experiments conducted by H. Shimizu and by J.M. Zhan (Shimizu et al., 2018), (Zhan et al., 2006). This phenomenon can be explained by considering the definition of the Reynolds number as shown in Equation 2.4. This equation shows that a low Reynolds number means the viscous forces are relatively high compared to the inertial forces which means the inertial forces have to fight a bigger viscous flow, causing a higher drag. On the contrary, a high Reynolds number means higher inertial forces fighting lower viscous forces, resulting in lower drag.

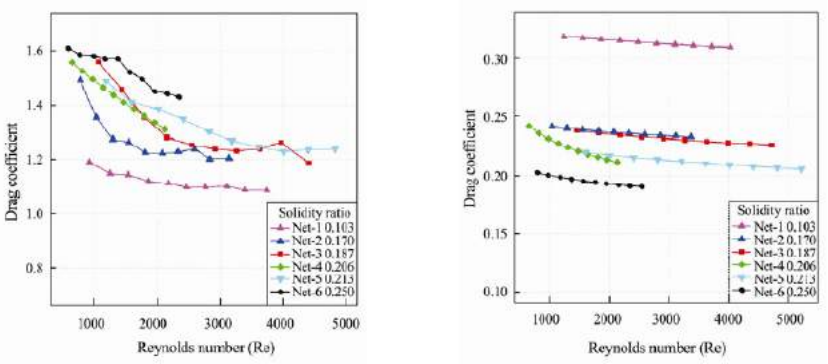

Figure 2.9: Drag coefficient as a function of Reynolds number for various solidity ratios. Left: panel perpendicular to the flow, right: panel parallel to the flow (Tang et al., 2017)

2.7. Influence of Shielding

As mentioned in Section 2.1 shielding is a phenomenon that occurs when a flow reaches a net panel under a certain inclination angle. Due to the angle of attack, the incoming flow can be disturbed by the first twine before reaching the second twine and so on. The leading twine is basically acting like a shield for the following twines which can drastically influence the drag coefficients by disturbing the flow. These disturbances can turn laminar flow into turbulent flow for example and influence in this way the drag on the system.

Looking at Equation 2.13 and Equation 2.14, introduced by Løland (Løland, 1993), the forces are dependent on the angle of attack θ in the following way:

$$F_D = \frac{1}{2}\rho C_D \theta A v^2 \tag{2.13}$$

$$F_L = \frac{1}{2}\rho C_L \theta A v^2 \tag{2.14}$$

Because the drag coefficient is a function of solidity ratio, mesh type, and Reynolds number, it is not possible to find a general expression for the drag coefficients as a function of S_n and Re for all combinations of these parameters. However, Geir Løland stated an estimated functional relationship in his paper (Løland, 1993):

$$C_D = 0.04 + (-0.04 + 0.33S_n + 6.54S_n^2 - 4.88S_n^3)\cos(\theta) \tag{2.15}$$

$$C_L = (-0.05S_n + 2.3S_n^2 - 1.76S_n^3)\sin(2\theta) \tag{2.16}$$

Important to notice here, Løland defined the angle of attack in a different way, namely, theta is the angle between the normal vector of the net and the incoming current, making it 90 degrees off of the attack angle definition of this report as discussed in Section 2.1. In Equation 2.15 the factor 0.04 is introduced as the drag on a net panel parallel to the flow. The equation makes the drag coefficient in this case independent of the solidity ratio, which is an approximation.

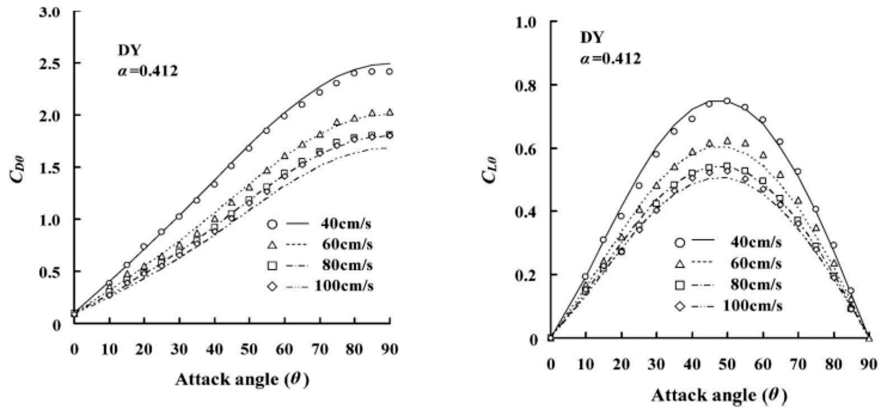

Figure 2.10: Drag coefficient $C_{D\theta}$ and lift coefficient $C_{L\theta}$ of Dyneema netting (solidity is $\alpha = 0.412$) in varying attack angle (Kumazawa et al., 2012)

When comparing Equation 2.15 and Equation 2.16 to the results of the flume tank experiments conducted by Taisei Kumazawa (Kumazawa et al., 2012), an interesting observation emerges. In the published paper, experiments on Dyneema netting are discussed. The solidity of the netting is 0.412 and with this solidity, the drag coefficients and lift coefficients on different angles of attack and current velocities are determined. In Figure 2.10, one can see the increasing drag coefficient with increasing attack angle and the parabolic curve in lift coefficient with increasing angle of attack. However, filling in the solidity of 0.412 from Taisei's experiment and the angles of attack results in the same shape, but in lower values for drag coefficient and lift coefficient. A possible conclusion of the difference between the results is that other properties also influence the drag and lift coefficient, like material, velocity, or mesh shape.

Drag reduction over length

As mentioned above, the interaction of the first twine with incoming flow can cause a reduction of the drag on the second twine and so on. However, because a net has a large amount of vertical twines, it is important to investigate on how this shielding influences twines over a longer distance. For this investigation, another comparison can be made with the aerodynamics of a high-speed cyclist.

In this comparison, every cyclist in the centerline of the peloton represents one vertical twine in the net towed through water. Wind tunnel tests performed in the Wind Tunnel Laboratory at Eindhoven University of Technology show the results as depicted in Figure 2.11 (Blocken et al., 2018). The figure expresses the measurements of the drag on the nine cyclists in the vertical center plane of the peloton. As the plot shows, the drag reduction from cyclist one to cyclist two is significant. The further back in the peloton, the lower this drag reduction is compared to the predecessor until the trend stabilises at a certain drag.

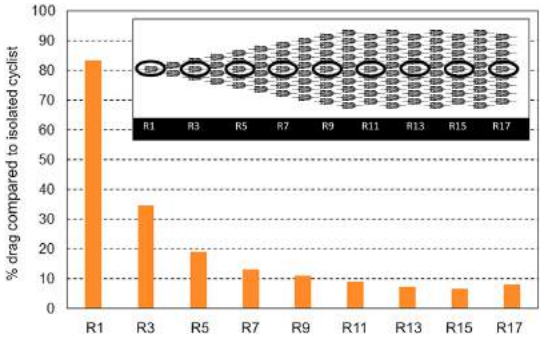

Figure 2.11: Wind tunnel results, expressing a percentage of the drag of an isolated cyclist riding at the same speed (Blocken et al., 2018)

3

Experiment

As the objective of the research is to develop a simple, yet accurate model that simulates the physical behaviour of a high length-to-depth ratio net towed through water, it is important to thoroughly understand how a net behaves during an operation. The forces required to drag a system through the water must be well understood in order to get accurate results from the model. To quantify the behaviour of nets, an experiment has been devised at MARIN. MARIN is a world renowned institute for maritime research, catering to the needs of the maritime sector, governments, and societies globally. It offers various facilities and tools, including basins, simulators, and software, to support comprehensive research in the maritime industry.

First, the experiment is introduced in Section 3.1. Next, the objectives of the experiment are outlined in Section 3.2. The experimental setup and test matrix are presented in Section 3.3. The conducted experiments are discussed in Section 3.4. Following this, the data processing steps are depicted in Section 3.5. Finally, the results and an evaluation of the experiment are presented in Section 3.6.

3.1. Experiment Introduction

As outlined in the problem statement, there is a lack of knowledge regarding the behaviour of the net when subjected to various angles of attack and the extrapolation of this behaviour from a net panel to a long net. On the left side of Figure 3.1, a schematic top view of The Ocean Cleanup system is presented. This figure clearly illustrates that different sections of the net encounter flow at different angles of attack. However, the inclination angles observed in the top view are not the only relevant angles in the system. The underwater cross-sectional shape of the net is also exposed to currents at varying inclination angles, creating a three-dimensional system where the net extends to a depth of four meters. These four meters are subjected to incoming flow, causing the net to curve and form a C-shape cross-section between the surface floater and the weighted cable at the bottom. This C-shape is more clearly visualised on the right side of Figure 3.1. By adjusting the tow-bar connected to the endpoints of the net, the C-shape can be altered into a J-shape or an inverted J-shape. In these configurations, parts of the net are exposed to incoming flow at specific angles of attack, which must be taken into account. Understanding the net behaviour under these varying angles of attack, both vertically and horizontally, is crucial. This experiment aims to contribute to this understanding.

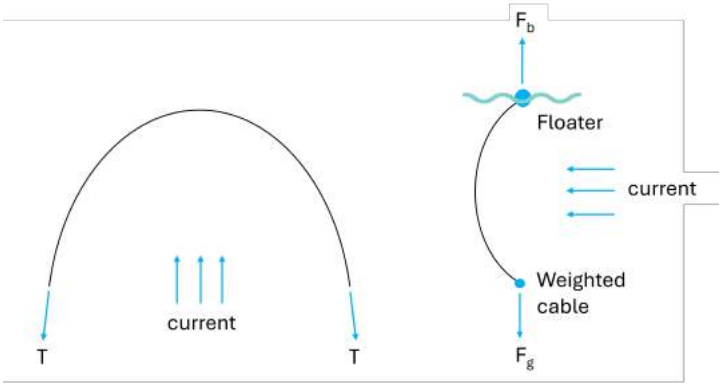

Figure 3.1: Left: Top view of whole net, Right: Side view of net showing the C-shape. T: tension [N] applied by towing vessels, F_g: gravity force [N], F_b: buoyancy force [N]

3.2. Objectives

The objectives of the experiment are:

- Experimentally measure and quantify hydrodynamic forces on the net during various towing conditions. This includes measurements on nets from earlier systems to quantify historical hydrodynamic forces and testing on possible future nets.
- Analyse the effect of net design parameters. By studying the responses on varying net parameters, as will be discussed in the methodology, internal knowledge gaps can be filled.
- Enrich and validate Digital Twin and currently used models. By validating the models and completely understanding the system's behaviour, it is eventually possible to scale up and predict the behaviour of future systems.

Looking at the problem statement as presented in Chapter 1, the main goal of the experiment is to gain knowledge on the shielding effect and on the extrapolation of forces on a small net to a large net.

3.3. Setup of Experiments

To conduct research on forces exerted on a net in water, a large towing tank is essential. This facility is provided by Maritime Research Institute Netherlands (MARIN) in Wageningen. This section outlines the setup of the experiment and the test matrix.

For this research, the Seakeeping and Manoeuvring Basin is selected as the location. With dimensions measuring 170 m x 40 m x 5 m, this basin provides enough space to achieve a constant speed and force while pulling the net through the basin. The net can be attached to the carriage which runs over the total length of the basin with a maximum speed of 6 m/s. The carriage comprises a main frame that extends across the entire width of the basin, with a subframe that moves along the main frame's width at a maximum speed of 4 m/s. Additionally, researchers have the option to generate waves using wave generators or simulate wind using wind fans within the basin. Figure 3.2 shows an image of the Seakeeping and Manoeuvring Basin.

Figure 3.2: Seakeeping and Manoeuvring Basin, MARIN

For the experiment, a custom-made structure has been built by MARIN, designed to rigidly attach the net to the carriage. This frame can be connected to the carriage under different angles, relative to the moving direction of the main carriage. Additionally to the straight movement of the mainframe, the subframe can move along the mainframe to create a diagonal movement through the basin. The moving direction of the mainframe, the moving direction of the subframe and the orientation of the structure connected to the carriage determine the angle of attack of the flow on the net.
At the top and bottom of the net, a sleeve is attached to connect the net to bars. These bars are connected to the structure at the right heights. Furthermore, the sleeves are pinned to the bars at the right width of the net. Force measurements are conducted using force sensors attached to each of the four corners of the net. Measuring the horizontal force in X and Y directions, every test results in eight force signals. The measuring frequency of the sensors is 200 Hertz. Other signals are the X and Y position and velocity of the carriage and the current measured by a flow meter connected to the structure. The measuring frequency of the carriage velocity and the current velocity is 200 Hertz and 100 Hertz, respectively.
Figure 3.3 shows the experimental setup.

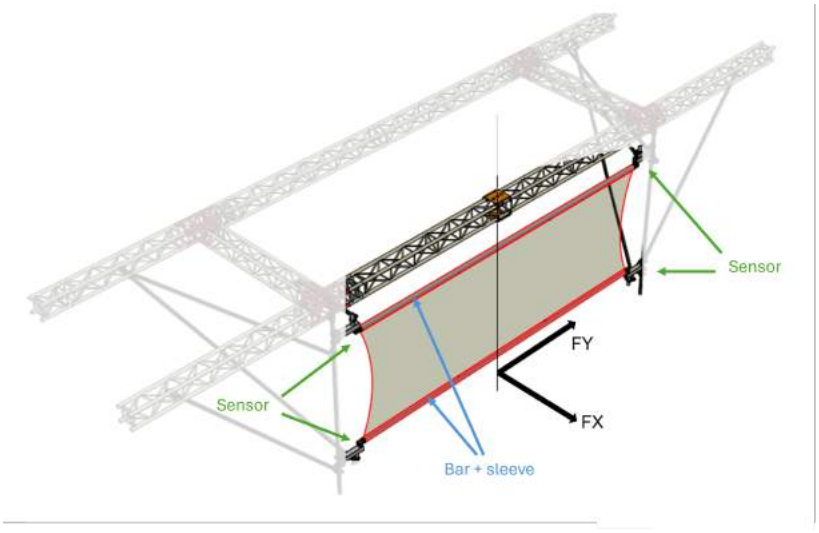

Figure 3.3: Experimental setup

One of the parameters in the drag coefficient calculation is the area of the net. When the net is installed in the frame, the frontal area of the net changes slightly due to the tension applied to the net. Half-circular indentations form on both sides, reducing the surface area. This is illustrated in Figure 3.4. By measuring the dimensions of the net, the estimated areas have been determined and are about 3.3 m^2 and 10.5 m^2 for the 2-meter and 6-meter long net respectively.

Figure 3.4: Picture of the net installed in the system showing half-circular indentations

To fulfill the objectives of the experiment, a test matrix was developed in close cooperation with The Ocean Cleanup and MARIN. This matrix aims to investigate various topics of interest. The purpose of the matrix is to gather sufficient information through the proposed tests to meet all the requirements outlined in the objectives. To save money and time, the test matrix is designed to maximize the amount of information gathered while minimising the number of tests required. In this test matrix, as shown in Table 3.1 and Table 3.2, all the different test configurations are presented. Table 3.1 shows all the test configurations for the net with a length-to-depth ratio of 1.

In this case, this means the net has a depth of two meters and a length of two meters. Table 3.2 shows all the test configurations for the net with a length of six meters and a depth of two meters, resulting in a length-to-depth ratio of three. The first net that is proposed to test, is the one from the system that is currently in use, called 'S03'. This net is used in the most recent campaigns, making it possible to compare measurements from the campaigns with results from the experiment. The other two nets are possible future nets called 'N1' and 'N2'. Nets N1 and N2 differ from net S03 in mesh size and twine diameter and are tested to investigate on possible nets for future systems. The solidity of nets S03, N1 and N2 are 0.179, 0.115, 0.102 respectively. The net dimensions are presented in Table 3.3. For the experiments, the length and depth of the Ratio 1 net are 2m x 2m, and the dimensions for the Ratio 3 net are 6m x 2m. Figure 3.5 illustrates how the frame with the net is placed at the four angles of attack.

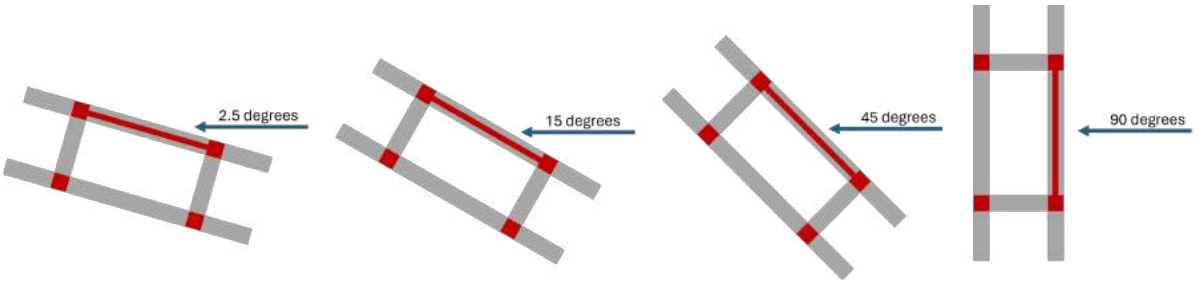

Figure 3.5: Top view of the frame and net at the four angles of attack

Ratio 1	V = 0.75 m/s				V = 1.5 m/s			
	AoA [deg]				AoA [deg]			
	2.5	15	45	90	2.5	15	45	90
S03	1	0	0	1	1	0	0	1
N1	1	0	0	1	1	0	0	1
N2	0	0	0	0	0	0	0	0

Table 3.1: Test matrix, net ratio 1

Ratio 3	V = 0.75 m/s				V = 1.5 m/s			
	AoA [deg]				AoA [deg]			
	2.5	15	45	90	2.5	15	45	90
S03	1	1	1	1	1	1	1	1
N1	1	1	1	1	1	1	1	1
N2	0	0	0	1	0	0	0	1

Table 3.2: Test matrix, net ratio 3

Name	S03	N1	N2
Twine diameter [mm]	1.5	1.7	2.1
Mesh size [mm]	16	28.5	40
Solidity	0.179	0.115	0.102

Table 3.3: Net dimensions

To gather information about the shielding effect, the test matrix includes tests on net behaviour at four angles of attack using the Ratio 3 net. To investigate the relationship between net behaviour and angle of attack efficiently, these tests are only conducted on net S03 and net N1. Tests on net N2 are conducted solely at a 90-degree angle, assuming that the relationship comes clear from the S03 and N1 tests. The tests at a 90-degree angle are specifically conducted on the Ratio 3 net and not on the Ratio 1 net, as it is assumed that the influence of the frame holding the net is less significant for the larger net compared to the smaller net.

In order to understand how to extrapolate the net behaviour of small nets to large nets, it is necessary to compare the forces on the large net to the forces on the small net at the same conditions (angle of attack and velocity). Therefore, the test matrix includes experiments for both net dimensions at the smallest and largest angle of attack. In all cases, the assumption is made that the tests on S03 and N1 are sufficient to understand the relations. To keep the test matrix as efficient as possible, only 90-degree tests are proposed for net N2 with Ratio 3.

3.4. Experiments

One of the lessons learned from the experiment is that things never go as planned which resulted in some slight changes in the test matrix. Due to problems in the manufacturing of net N2, the test matrix is reduced to only net S03 and net N1. In the original test matrix, net N2 was only planned to test on Ratio 3 at an angle of 90 degrees for the two velocities. Because of the limited tests for this net, the manufacturing problems should not influence the experiment results too much.

Another change in the test matrix is the smallest angle of attack. The original test matrix shows an angle of attack of 2.5 degrees. However, looking at the videos of the first few tests, showed that the frame creates a disturbance in the water in a v-shaped wave at an angle of about 2.5 degrees. To still measure the forces on the nets in undisturbed water, the angle of attack is slightly increased to five degrees.

The third and last change in the test matrix is an extra velocity of 2.25 m/s. After noticing the time to conduct an experiment is relatively way less than the time it takes to adjust the setup to a new angle, the decision is made to add an extra velocity. For the Ratio 3 nets, the extra velocities are used for an extra test at the smallest angle of attack. This extra data can be used to see the influence of the velocity on the behaviour of the net. For the small nets of Ratio 1, the extra velocity is tested at an angle of attack of 90 degrees. However, after the test of net S03 at a velocity of 2.25 m/s and an angle of attack of 90 degrees, it turned out the forces on the system were high. During the run, water overwashed over the top bar of the system and the bottom bar moved. Because of this unpredictable behaviour, this test is not repeated for the N1 net.

The mentioned changes result in the final test matrices as presented in Table 3.4 and Table 3.5.

Ratio 1	**V = 0.75 m/s**				**V = 1.5 m/s**				**V = 2.25 m/s**	
	AoA [deg]				**AoA [deg]**				**AoA[deg]**	
	5	**15**	**45**	**90**	**5**	**15**	**45**	**90**	**5**	**90**
S03	1	0	0	1	1	0	0	1	0	1
N1	1	0	0	1	1	0	0	1	0	0

Table 3.4: Test matrix, Ratio 1

Ratio 3	**V = 0.75 m/s**				**V = 1.5 m/s**				**V = 2.25 m/s**	
	AoA [deg]				**AoA [deg]**				**AoA[deg]**	
	5	**15**	**45**	**90**	**5**	**15**	**45**	**90**	**5**	**90**
S03	1	1	1	1	1	1	1	1	1	0
N1	1	1	1	1	1	1	1	1	1	0

Table 3.5: Test matrix, Ratio 3

Figure 3.6 and Figure 3.7 below depict the on-board and under-water views of the net during one of the experiments. The on-board view illustrates the disturbance of the water caused by the net, creating a small amount of whitewash and a trailing wave. The under-water view shows the deformation of the net due to the forces acting on it.

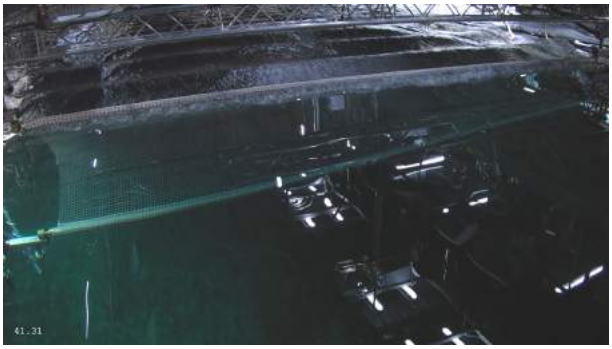

Figure 3.6: On-board view on net

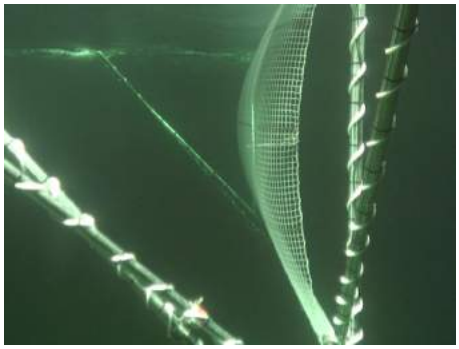

Figure 3.7: Under-water view on net

During the tank tests, sensors measure the loads on the entire system. However, to understand the loads specifically on the net, the loads on the frame must be subtracted from the total measured load, as they contribute to the overall load. After completing the tank tests outlined in the test matrix, the net was removed from the system, leaving only the sleeves encasing the bars. This modified configuration allowed for assessing the drag on the system itself at four angles of attack and two velocities. By processing the results this way, the measured loads on the frame alone can be subtracted from the total system loads, providing a clearer picture of the loads on the net.

3.5. Experimental Data and Processing

In each test case as presented in Table 3.4 and Table 3.5, a raw data signal is generated by summing the readings from the four force sensors. Following this, the individual X and Y forces are combined to produce the overall force magnitude. To illustrate, one of the cases is considered and presented in Figure 3.8: 2-meter net, labeled as N1, at a 90-degree angle and a velocity of 0.75 m/s.

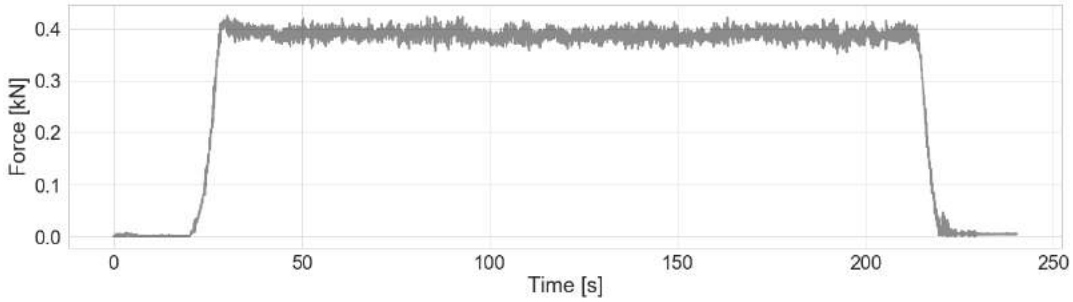

Figure 3.8: Total force

Phase definition

Looking at this signal, it can be divided into three stages: acceleration, constant velocity, and deceleration. The first step in the processing of the data is to determine where exactly the start and end point is of this period with constant velocity. These time points are determined by applying a filter to the raw force signal, followed by assessing the gradient of this filtered force signal.

To determine the start point and end point of the constant velocity phase, a lowpass filter is used to filter out higher frequencies. The result of conducting a Fourier analysis of the continuous force signal over time is a description of how the power of the signal is distributed over frequency. The unit of this power is the unit of the signal squared per Hertz, so in this case the unit is N^2/Hz. A Power Spectral Density plot of the raw signal is presented in Figure 3.9. This plot clearly shows a high peak at a frequency very close to zero. This peak represents the increase in load and the decrease in load at the beginning and at the end. This is the frequency that is interesting in defining the time point of this occurrence. As the plot shows more peaks at frequencies starting at two Hertz, the lowpass filter cutoff frequency is set at two Hertz, meaning that the frequencies above two Hertz are filtered out.

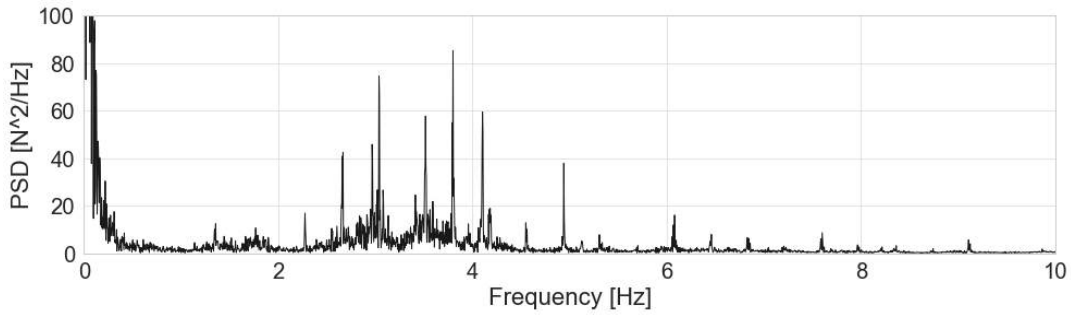

Figure 3.9: Power Spectral Density

After implementation of the low-pass filter, the force signal of the test case looks like as presented in Figure 3.10.

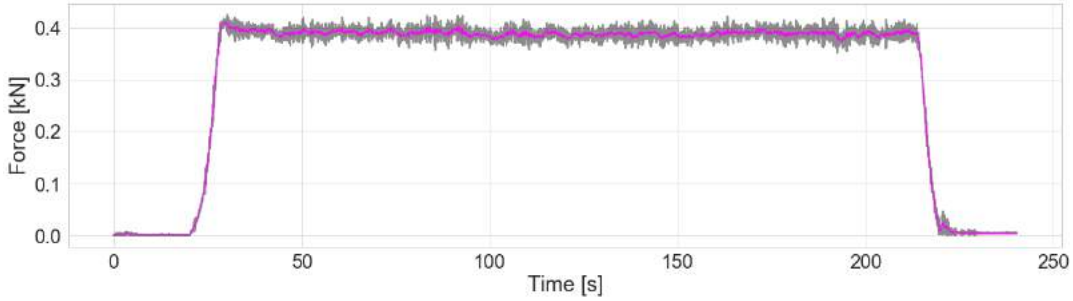

Figure 3.10: Total force after implementing low-pass filter

In order to define the range with constant velocity, a plot depicting the gradient of the filtered signal is utilised and this plot is depicted in Figure 3.11. The gradient plot shows two prominent peaks, representing the acceleration and deceleration phases of the experiment. In between the peaks, the gradient is close to zero, meaning that the filtered signal remains on a constant force. The start and end-point of this constant force period are visualised using two vertical red lines. These points are then implemented in the force plot as shown in Figure 3.12. The horizontal red line shows the median gradient value, which should be close to zero in all cases.

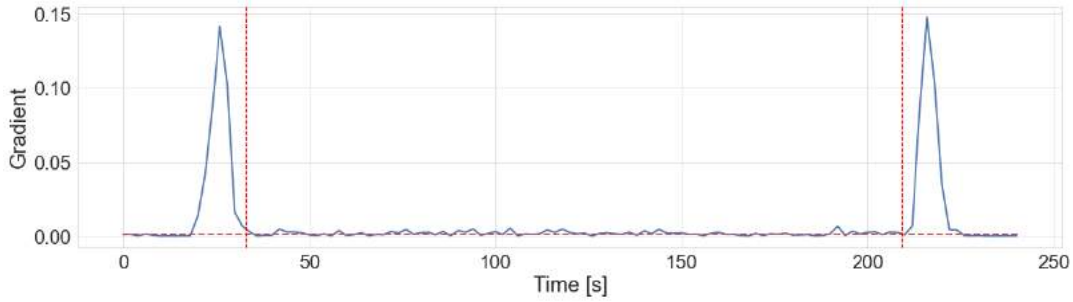

Figure 3.11: Gradient

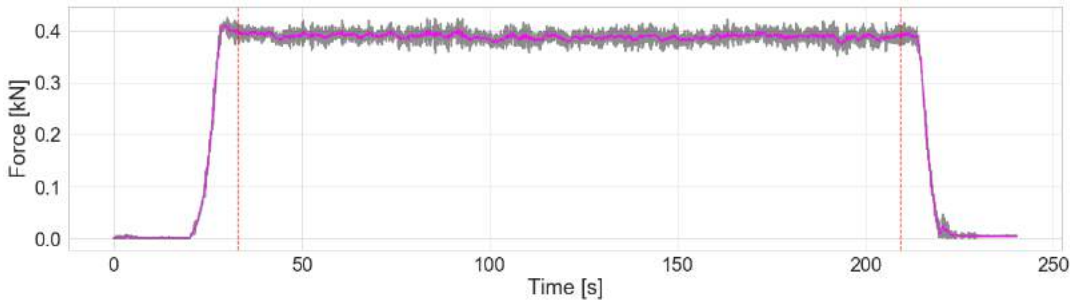

Figure 3.12: Total force

Now that the time period of constant velocity is defined, the measured loads in this range can be assessed. To do this, all raw load signals are cut off at the start point and end point of the constant-velocity phase.

Load definition

During the acceleration of the carriage from standstill to 0.75 m/s, the force on the net increases. After the system reaches 0.75 m/s, it remains at this constant velocity, causing the force on the system to stabilise. However, during this period of constant velocity, the signal exhibits high-frequency fluctuations. These fluctuations are clearly presented in Figure 3.13.

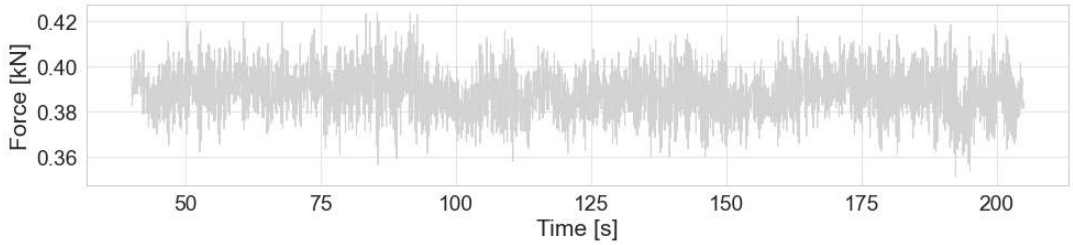

Figure 3.13: Total force

The presented fluctuations are hypothesised to stem from vortex-induced vibrations generated by the frame. Vortex-induced vibrations occur when a structure interacts with an incoming flow, causing motion. The irregularities in the external flow passing over the system's frame or the net itself could trigger the shedding of vortices in a periodic manner, resulting in a repetitive, high-frequent, pattern of motion. To make an estimation of the frequency of these fluctuations, the Strouhal number (St) is utilised. This Strouhal number can be determined by using the Reynolds number for the vertical and the horizontal bars of the frame. By looking at the Reynolds numbers for the horizontal and vertical bars at 0.75 m/s and 1.5 m/s, the Strouhal number is about 0.2 (Ivanco, 2009). Equation 3.1 presents the equation to calculate the frequency of the fluctuations. The diameter of the horizontal and vertical bars is 80 mm and 48 mm respectively. Table 3.6 shows the outcomes of using these values to calculate the frequencies.

$$f = St * \frac{v}{D} \tag{3.1}$$

	0.75 m/s	**1.5 m/s**
Horizontal bar	1.9 Hz	3.8 Hz
Vertical bar	3.1 Hz	6.3 Hz

Table 3.6: Estimated frequencies for fluctuations

To assess whether the high-frequency fluctuations in the signals are vortex-induced vibrations generated by the frame interactions with the fluid, the PSD plot of the full test setup (Figure 3.16) is compared to the PSD plot of the same test excluding the net (Figure 3.15). In this case the two-meter S03 net at 90 degrees at 1.5 m/s is compared to the frame with the two-meter sleeves at 90 degrees and 1.5 m/s (Figure 3.14). Initial observations indicate that the power distribution across the frequency spectrum is slightly different when comparing the two PSD plots. As stated in Table 3.6, the expected vibration frequencies of only the frame are at 3.8 and 6.3 Hertz. The two peaks as observed in the plots are close to these expected peaks. Some inaccuracies can stem from inaccurate calculations of the Reynolds number and Strouhal number. Also, the wires around the vertical and diagonal bars and the sleeves around the horizontal bars can influence the locations and magnitudes of the peaks in the plots.

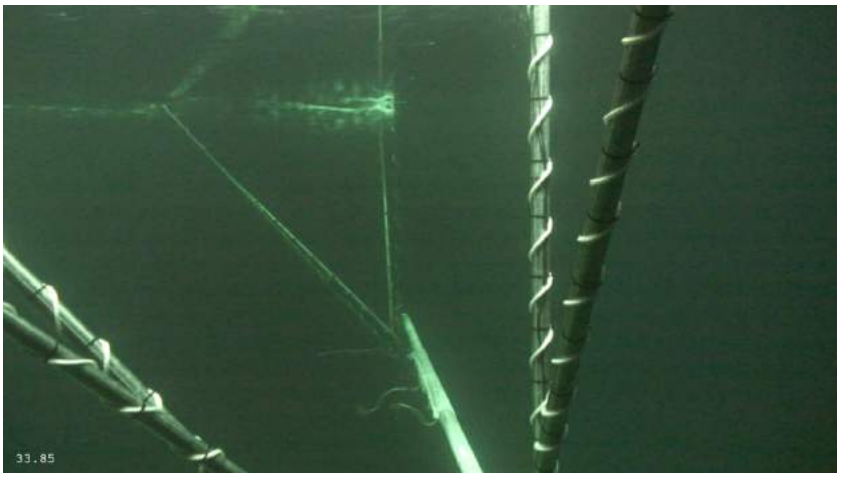

Figure 3.14: Horizontal bar with sleeve and vertical grooved bars

In the experimental setup, it is notable that a small cable encircles the vertical bars, aimed at mitigating vortex-induced vibrations. Z. Hao conducted a study comparing vortex-induced vibrations on a bare cylinder with those on a grooved cylinder similar to the vertical bars in the frame (Hao et al., 2022). This research revealed a reduction of approximately 36% in vortex-induced vibration peak amplitudes when comparing the bare cylinder with the grooved one.

In a study by Ramzi, the suppression of vortex-induced vibrations of a cylinder wrapped in a flexible net was investigated (Ramzi et al., 2022). The findings of the study revealed a significant reduction in the peak amplitude of vibrations, reaching up to 90.42%. Consequently, the anticipated vibrations around 3.0 Hertz might not be as powerful as they would be without the sleeves.

In addition to the horizontal and vertical bars that induce vibrations, diagonal bars are installed in the frame for added stiffness. However, these diagonal bars can also play a role in generating vortex-induced vibrations, which might explain the presence of additional small peaks observed in the Power Spectral Density plots.

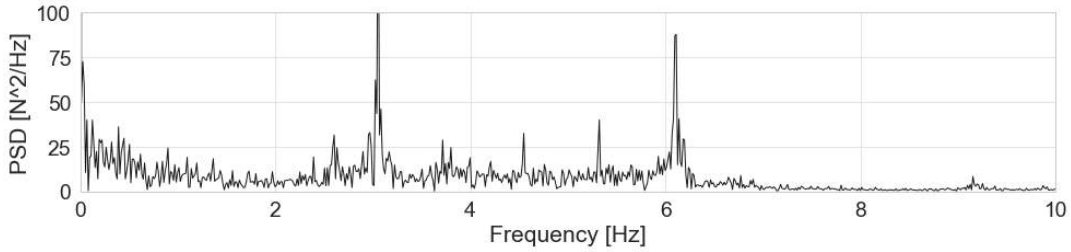

Figure 3.15: Power Spectral Density of load on test setup excluding net

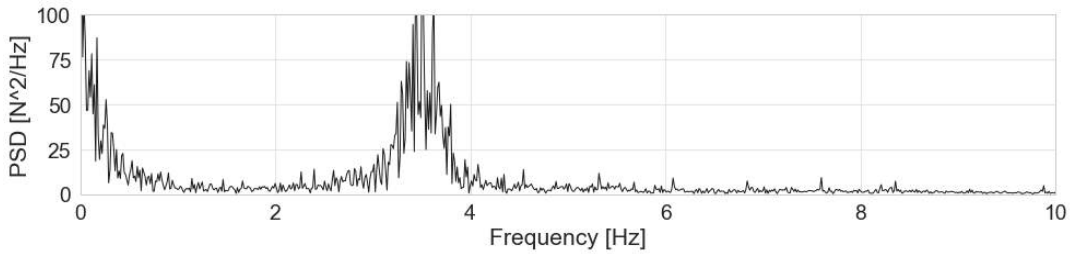

Figure 3.16: Power Spectral Density of load on full test setup

When comparing the PSD plot in the situation without the net in Figure 3.15 to the PSD plot in the situation with the net in Figure 3.16, a significant difference is noticeable. Vibrations around 6.3 Hertz are almost entirely mitigated. Additionally, the frequencies of vibrations expected from the horizontal bar are slightly increased. These changes can be attributed to the installation of the net within the frame. The pretension in the net introduces additional stiffness to the system, which slightly elevates the frequency of vortex-induced vibrations and helps reduce the vibrations caused by the vertical bars. This damping of the vortex-induced vibrations because of the pretension in the net is even better visible when assessing a test of the six-meter net. The following plot shows the power distribution for the six-meter S03 net at an angle of attack of 90 degrees and a towing velocity of 1.5 m/s (Figure 3.17). The plot shows that the pretension of the long net and the coverage of the bar almost fully mitigates the vortex-induced vibrations generated by the horizontal bar and vertical bars.

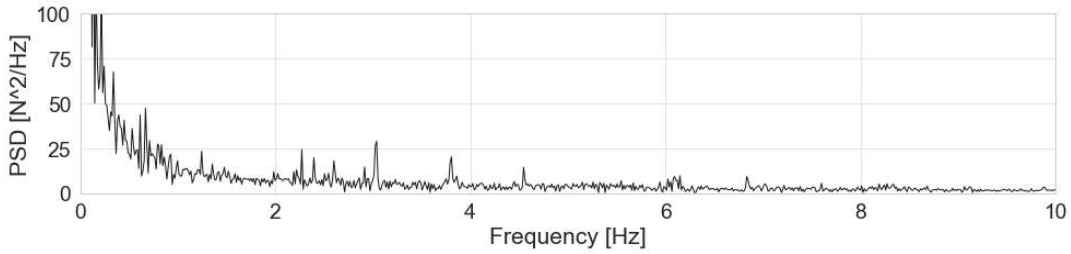

Figure 3.17: Power Spectral Density of load on net: N1, 6m, 90 degrees, 1.5m/s

3.6. Results

The mean total force is determined for each case by analysing the load-signal within the designated time frame. Figure 3.18 illustrates the mean forces across all test cases. The dashed line represents the trend of the force acting on the entire system. Respectively, the plots show the Ratio 1 net at slow speed, the Ratio 3 net at low speed, the Ratio 1 net at high speed and the Ratio 3 net at high speed.

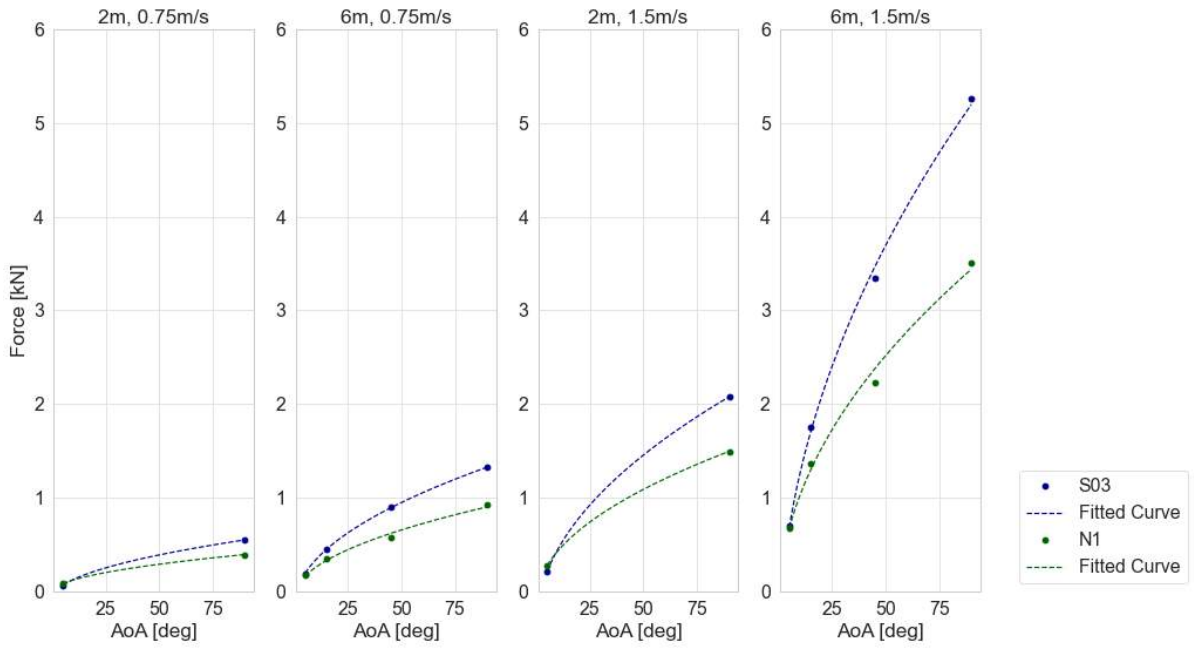

Figure 3.18: Total mean forces

Because the frame itself can influence the flow and with that, the drag on the net, tests are conducted on the system itself, excluding the net. These results are presented in Figure 3.19.

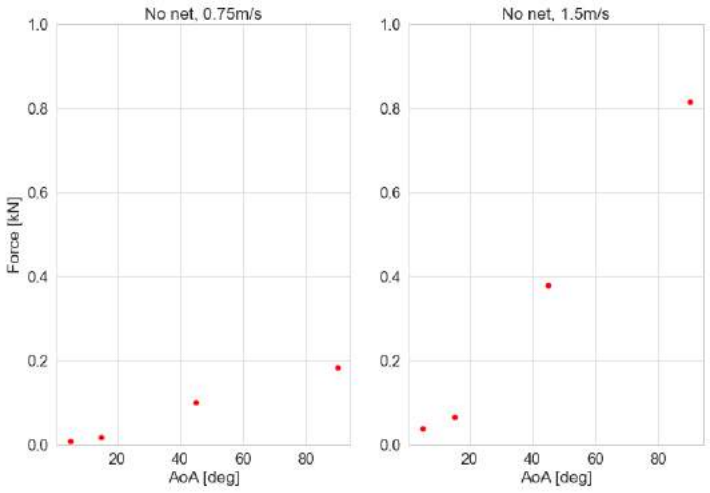

Figure 3.19: Total mean forces, no net

After subtracting these values, the drag force on solely the net remains. This is depicted in Figure 3.20.

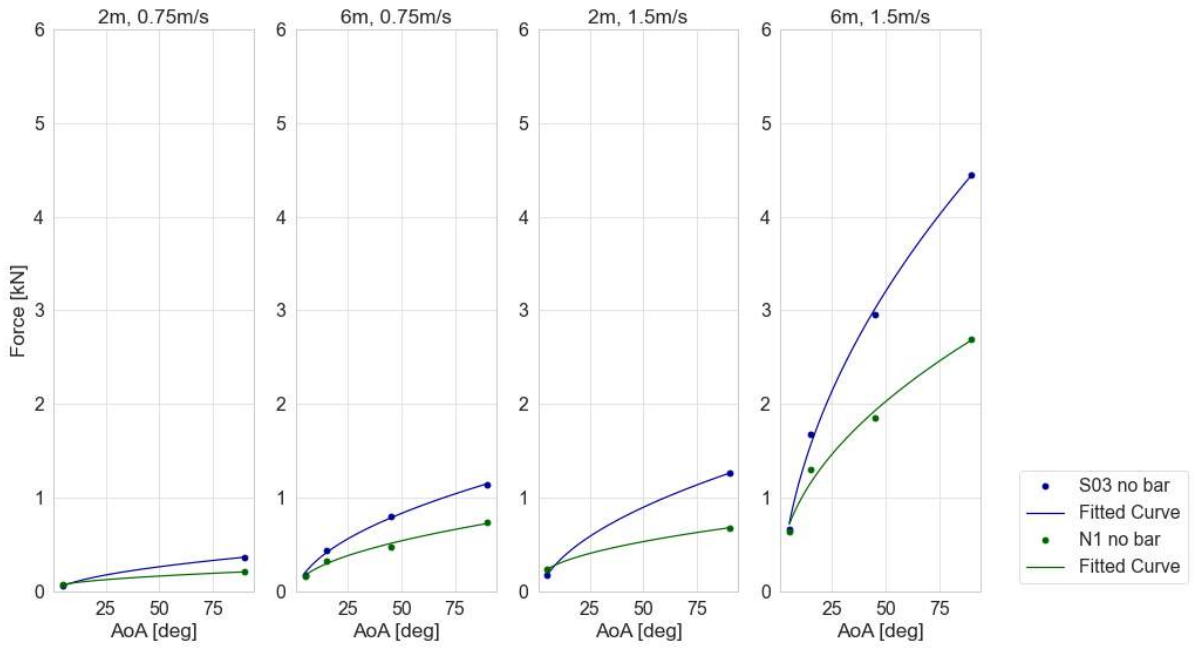

Figure 3.20: Mean forces on the net

3.6.1. Shielding and Extrapolation

For a comprehensive comparison between the various angles of attack and net lengths and thereby get a better understanding of the net behaviour, Figure 3.21 provides a close-up view of the drag forces acting on the net. In these plots, all forces are normalised by dividing each force by the maximum force on the system at the given velocity, which corresponds to the measured force of the 6-meter net at a 90-degree angle of attack.

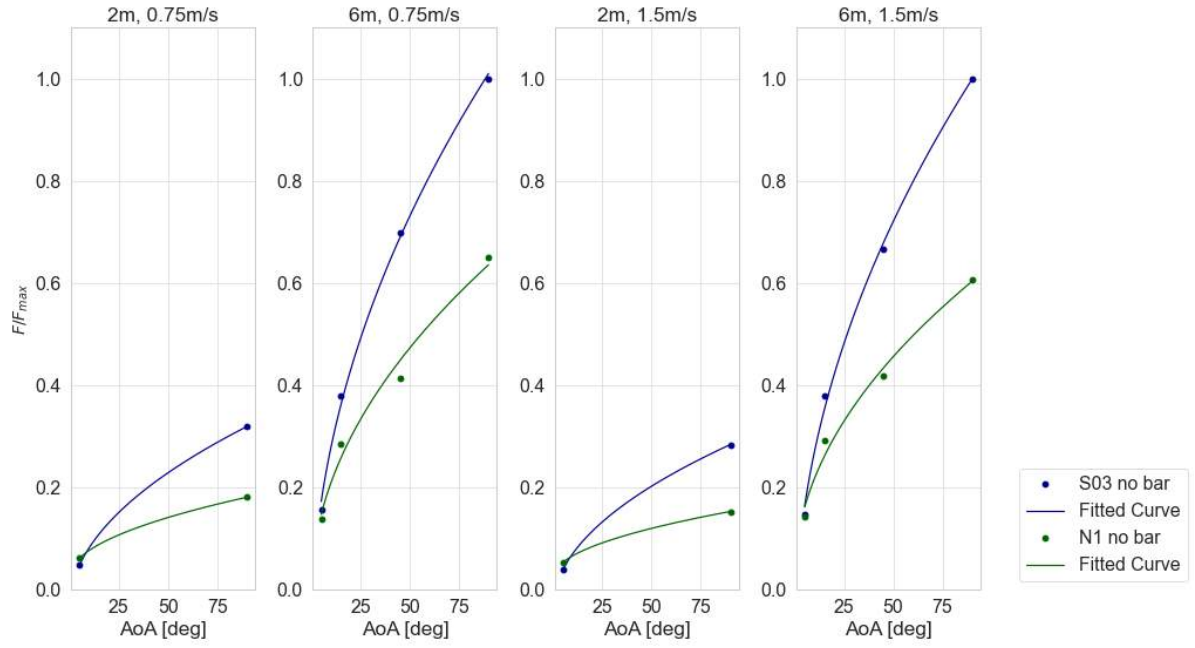

Figure 3.21: Normalised force on net

First, a closer look is taken at the angle of attack of 90 degrees. In all cases, the net N1 has a significantly lower force compared to the S03 net. The clear reason for this is the solidity of the nets. As introduced in Section 2.6, a higher solidity means a higher projected area, resulting in a higher drag

force when placed at an angle of attack of 90 degrees. As the solidity of net S03 is 0.179 and the solidity of net N1 is 0.115, the drag on S03 is higher.

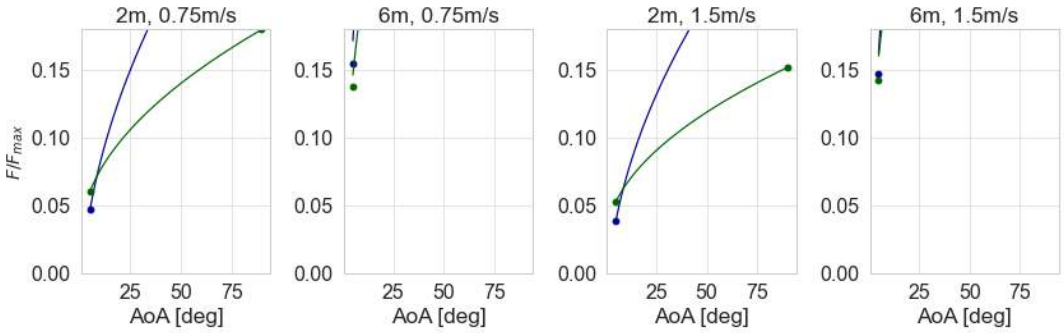

Figure 3.22: Close-up view on normalised force on net

Zooming in on the results at an angle of attack of 5 degrees shows more interesting results. Figure 3.22 provides a close-up perspective of Figure 3.21. Specifically, when focusing on the 2-meter nets, it's notable that the forces acting on net S03 are approximately 30% lower than those on the 2-meter N1 net. This unexpected reduction in drag on the S03 net can be attributed to the phenomenon known as shielding. The higher solidity of net S03, stemming from its smaller mesh size, results in the front twines partially shielding the subsequent twines from the incoming flow, leading to a diminished drag force on the overall net. A more extensive explanation can be found in Section 2.7.

However, contrasting results emerge when analysing the 6-meter nets. In these instances, S03 exhibits slightly higher loads compared to the N1 net. As elaborated in Section 2.7, the shielding effect induces a significant decrease in resistance for twines immediately following the first twine. Because of the shielding effect being stronger for higher solidity, the force on net S03 is lower at this small angle of attack. Nonetheless, it's crucial to note that this shielding effect is contingent upon the length of the net and may not hold for extended lengths. As observed in Figure 2.11, the shielding effect stabilises after a certain number of components. Consequently, the heightened drag on the initial twines becomes less influential on the total drag, with the amount of material towed through the fluid becoming governing again. For this stabilised part, a higher solidity results in a higher load. Therefore, the S03 net experiences a higher load compared with the N1 net.

In the figure below, Figure 3.23, the normalised load is plotted versus the net length at an angle of attack of five degrees. The lines in the plot of 0.75 m/s cross at a net length of about 3.8 meters. This point means the point where the shielding on the first part does not compensate for the stabilised part of the net anymore at this velocity. For 1.5 m/s, this point has shifted to the right to approximately 5 meters. This means a higher velocity results in a shielding effect reaching longer distances. The third plot shows the results of the tests at 2.25 m/s and the points get even closer meaning the point of intersection is close after 6 meters for this velocity.

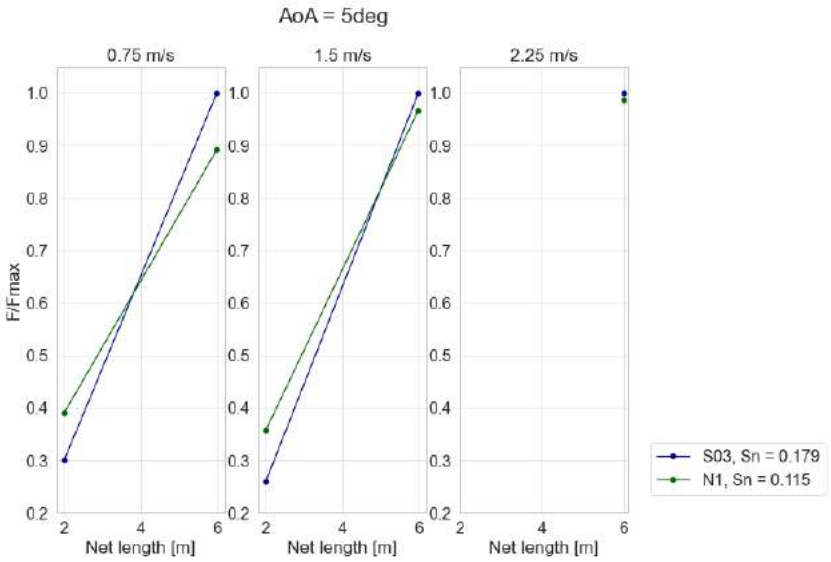

Figure 3.23: Experiment results for AoA = 5 degrees

Because only two net lengths are tested, the exact relation between load and net length is unknown. Therefore, there is a linear line between the two lengths, giving an indication of the intersection point.

As the results have shown, the shielding effect primarily affects shorter sections of the net. Since The Ocean Cleanup System 03 uses a net of over 2000m, for now, further calculations will be based on the results obtained from the 6-meter nets.

3.6.2. Drag Coefficients

Now that the total drag force is determined, the drag equation can be used to determine the corresponding drag coefficients. This equation is presented once more in Equation 3.2.

$$C_D = \frac{F_D}{\frac{1}{2}\rho A S_n v^2} \tag{3.2}$$

Using the measured drag forces, areas, and velocities, the drag coefficients are calculated. These coefficients are illustrated in Figure 3.24.

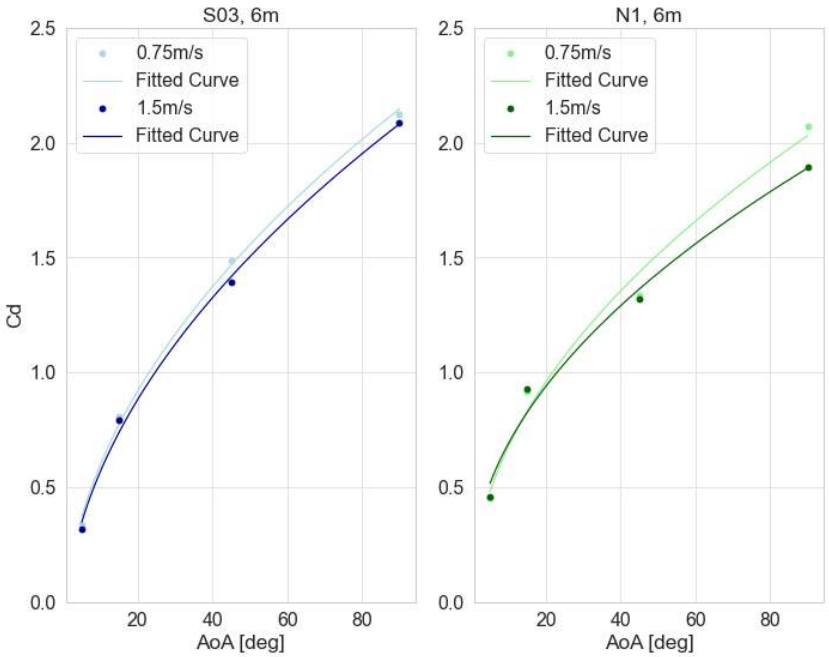

Figure 3.24: Drag coefficients, 6m

In the plot, the light blue and light green line show the calculated drag coefficients at a velocity of 0.75 m/s. The dark blue and dark green line show the calculated drag coefficient at high speed. For the model input, the used drag coefficients are the mean of the two lines. These drag coefficients are shown in Table 3.7.

AoA	**5**	**15**	**45**	**90**
S03	0.33	0.80	1.44	2.11
N1	0.45	0.92	1.33	1.98

Table 3.7: Input drag coefficient

4

Model

A computer model is a representation of reality that utilises mathematical algorithms and computational techniques to simulate the real world. An effective model maintains simplicity while ensuring accuracy is not compromised.

This chapter starts with the introduction of the 3D Finite Element model as utilised by The Ocean Cleanup in Section 4.1. Next, a step-by-step explanation of the 2D simplified model is presented in Section 4.2. Lastly, the estimated drag coefficients used in the model and the wave implementation are treated in Section 4.3 and Section 4.4, respectively.

4.1. 3D Finite Element Model

The Morison equation is used in OrcaFlex to model forces on a structure generated by fluid flow. The application of this equation to the 3D model is discussed in Subsection 4.1.1. The model is then used to generate results under various conditions, which are presented in Subsection 4.1.2.

4.1.1. Modelling Approach

Morison Equation

OrcaFlex is a software that is used for dynamic analysis of offshore marine systems. In this case, it is used to model a Digital Twin (DT) of The Ocean Cleanup system as described in Section 1.3. The Digital Twin in OrcaFlex can be used for simulating the behaviour of the complex system under different environmental conditions such as waves, currents, and wind. Morison's equation (Morison et al., 1950) and potential flow serve as the bases for modelling the forces on a structure generated by fluid flow. In the equation, as stated in Equation 4.1, added mass, fluid inertia force and drag force are taken into account.

$$f_{OF} = m_f \left(C^*_{M,OF} \frac{d\mathbf{u}}{dt} - C^*_{A,OF} \frac{dv_b}{dt} \right) + \frac{1}{2} \rho_f C^*_{D,OF} A |\mathbf{u}_r| \mathbf{u}_r \tag{4.1}$$

Here $C^*_{M,OF}$, $C^*_{A,OF}$ and $C^*_{D,OF}$ represent the drag coefficient for the body, the added mass coefficient for the body and the inertia coefficient for the body, respectively. Furthermore, m_f, $\mathbf{u}$, v_b, ρ_f, A and $\mathbf{u}_r$ represent mass of the fluid displaced by the body, fluid velocity relative to the earth, the velocity of the body relative to the earth, the density of the fluid, the drag area and the fluid velocity relative to the body. The OrcaFlex drag force is presented in the second term of this equation (Jiménez et al., 2023). The drag force is split up into three components: two components normal to the considered line and one tangential to the considered line. The equations for the three components are as follows:

$$f_{Dx,OF} = \frac{1}{2} \rho_f C^*_{Dx,OF} d_s l_s \mathbf{u}_x |\mathbf{u}_n| \tag{4.2}$$

$$f_{Dy,OF} = \frac{1}{2} \rho_f C^*_{Dy,OF} d_s l_s \mathbf{u}_y |\mathbf{u}_n| \tag{4.3}$$

$$f_{Dz,OF} = \frac{1}{2}\rho_f C^*_{Dz,OF} d_s l_s \mathbf{u}_z |\mathbf{u}_n| \tag{4.4}$$

Here $\mathbf{u}_n$ is the normal component of the fluid velocity relative to the line. The z-component is the axial component. d_s represents the diameter of the line and l_s the length of the line.

Application to the 3D Finite Element model

The stated equations for the drag force calculations are applied to the 3D model in OrcaFlex. The net of The Ocean Cleanup system is converted into equivalent horizontal lines, connected by vertical links. This is drawn in Figure 4.1. The reason for this conversion to equivalent lines instead of twine-by-twine modelling is the reduction of computational demand. Modelling a net of two-and-a-half kilometer net results in millions of elements, requiring significant computational power. Therefore, the twines are replaced by equivalent consistent net elements. The entire system is divided in these elements of ten meters. At both ends of the net, vertical steel pipes are modeled, mirroring their real-world counterparts that help keep the net open and connect it to the towing lines. The calculated drag on all the lines is an equivalent representation of the drag of the real-world data. To calculate the total drag on the entire system, the drag contribution of each segment is added. The normal drag coefficient is determined as proposed by Naumov (Naumov et al., 2013) and is introduced in Section 2.4. Images of the OrcaFlex model are shown in Figure 4.5.

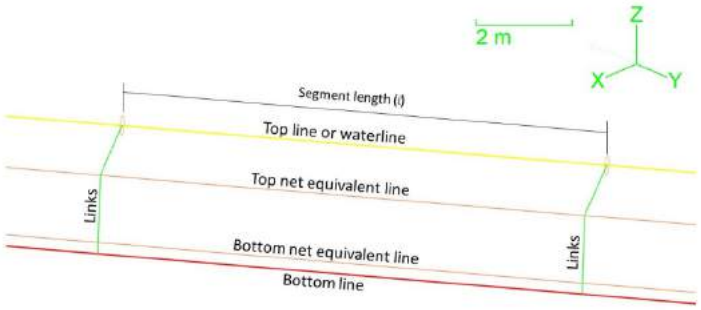

Figure 4.1: Wing section OrcaFlex model (Jiménez et al., 2023)

The approach resulted in limitations in the 3D model, namely: no shielding included in the model due to the way of modelling using equivalent lines and no possibility to calculate the drag twine by twine. To overcome these limitations, AquaSim and Basilisk are used in extra validation rounds. After a third validation cycle, the used drag coefficients, dependent on the angle of attack, are presented in Table 4.1.

θ (°)	0	1	2	3	5	10	20	30	45	90
C_D	0.4614	0.4732	0.4849	0.5253	0.6076	0.8492	1.2649	1.3822	1.5589	1.5967

Table 4.1: OrcaFlex Drag Coefficients

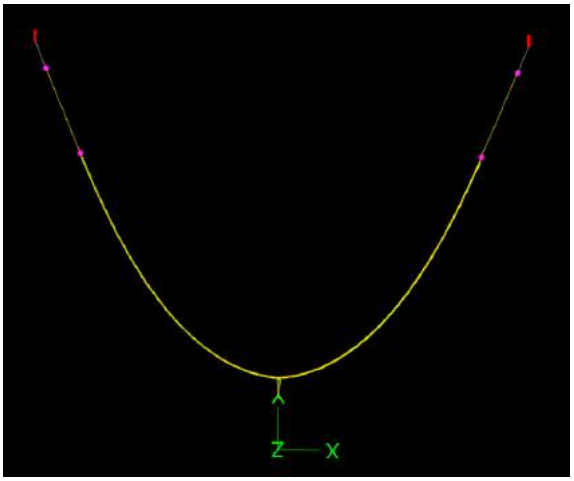

Figure 4.2: Full system

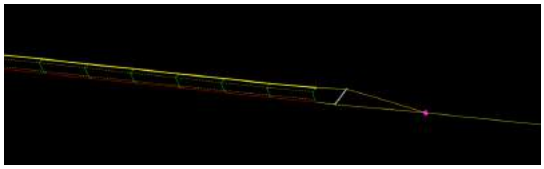

Figure 4.3: End point with steel pipe

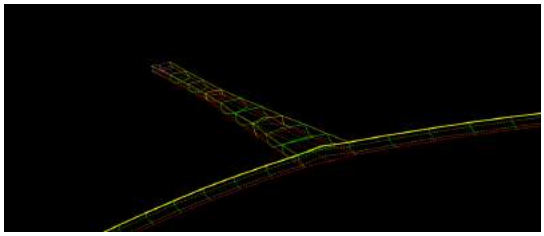

Figure 4.4: Retention zone

Figure 4.5: OrcaFlex Model

4.1.2. 3D Finite Element Model Results

As mentioned, The Ocean Cleanup utilises OrcaFlex to conduct simulations of the entire system, predicting forces under various conditions. Analyses have been done using the 3D model, running multiple simulations to investigate the influence of different parameters on the loads experienced by the system. In Table 4.2, the input variables for the used simulations are presented, including the calculated mean force exerted on the system. The table presents the velocity v, the span S, the significant wave height Hs and the calculated mean tow load F.

v [m/s]	S [m]	Hs [m]	F [kN]
0.5	1000	0	103.2
0.75	1000	0	226.0
0.5	1400	0	132.1
0.75	1400	0	285.1

v [m/s]	S [m]	Hs [m]	F [kN]
0.5	1000	2	154.4
0.75	1000	2	288.5
0.5	1400	2	186.2
0.75	1400	2	352.9

Table 4.2: 3D Finite Element model simulations

By utilising the calculated outputs, a regression line can be established. For the establishment of the regression line, one should look at the different factors and how they scale with the load. The first two terms are defined by looking at the drag equation in Equation 2.5. Firstly, a term is introduced that scales with the load, namely ($span * velocity^2$). Because only this term is not enough to describe the loads' dependence on span and velocity accurately, a second term is added: ($span * velocity$). To account for wave loads, the third term is the significant wave height. All three terms are multiplied with a specific coefficient. Lastly, a constant is added to compensate for the errors. The regression line is as follows:

$$Load = 0.486 * S * v^2 - 0.132 * S * v + 29.5 * H_s + 48.5 \tag{4.5}$$

Based on this regression analysis, the current System 03 is developed by The Ocean Cleanup and deployed in the GPGP. This 3D Finite Element model regression line acts as the 'competitor' of the 2D simplified model and they will be compared in Chapter 5.

Regression analysis validation

This regression analysis is based on data from eight different simulations. To validate the analysis, it is applied to a separate dataset derived from another set of eight simulations. The input values for these

simulations are processed using OrcaFlex to estimate loads, and the outcomes are then compared with the predictions from the regression analysis. The inputs, alongside the results from both the OrcaFlex simulations and the regression analysis, are detailed in Table 4.3.

v [m/s]	S [m]	Hs [m]	$F_{OrcaFlex}$ [kN]	$F_{Regression}$ [kN]	Error [%]
0.5	1000	4	224.4	221.9	-1.1
0.5	1400	4	255.3	244.1	-4.4
0.75	1000	4	376.9	340.9	-9.6
0.75	1400	2	330.9	351.8	6.3
0.75	1400	4	399.0	410.7	2.9
1.0	1000	0	396.4	402.9	1.6
1.0	1000	2	466.2	461.8	-1.0
1.0	1000	4	565.8	520.7	-8.0

Table 4.3: Loads generated by OrcaFlex simulations versus regression analysis

As indicated in the final column, the error for all validation simulations remains at an average of 4.4%, confirming the validity of the regression analysis.

4.2. 2D Simplified Model

As previously stated, a computer model serves as a representation of reality, wherein only the important aspects are incorporated. The simplifications within the 2D model are outlined in Subsection 4.2.1. Subsequently, an exposition of the model is provided in Subsection 4.2.2, presenting the procedural steps within the model.

4.2.1. Simplifications

As mentioned, one of the main disadvantages of the 3D model is the high computational demand for calculations and simulations due to the very large number of elements. To develop a model that, on the one hand, is capable of accurately predicting forces and net behavior in operation, but on the other hand is usable for fast calculations, it requires simplifications.

The first simplification involves disregarding the dynamics of the system's motions. This is feasible because, due to the system's size and inertia, all movements are inherently slow. The system's inertia prevents it from reacting significantly to dynamic forces, such as short-period waves. Additionally, dynamic modeling of the system is unnecessary since the system does not operate in extreme weather conditions. High waves, for example, can cause 'overtopping,' where plastics are forced over the net, reducing operational efficiency. Given the minimal benefits of a dynamic model, a quasi-static model is sufficient. In a quasi-static model, it is assumed that the motion of the system is linear between two static positions during a given time step, and the loads on the system are considered constant. Lastly, the model will be validated using measurement data gathered from real-life campaigns in the GPGP. This data, which provides 5-minute averages for each signal, averages out dynamic effects. Therefore, implementing dynamics in the model cannot be validated using this data.

The second simplification involves creating a two-dimensional model instead of a three-dimensional one, significantly reducing the number of elements and, consequently, the computational demand. In this simplified model, the horizontal and vertical twines are replaced with a single horizontal line that represents the combined drag of the floater, the entire depth of the net, and the weighted bar at the bottom. The Ocean Cleanup conducted tests on the floater's drag, revealing that the ratio between the

floater's density and the water's density is approximately 0.1. This suggests the floater is only slightly submerged, and the drag generated by this small submerged volume is considered negligible. Therefore, the equivalent line must represent the drag of both the net and the weighted bar at the bottom.

The two proposed approaches are established for the model from this point onwards. Through validation, it will be determined whether these approaches are sufficient to make the model both simple and accurate.

4.2.2. Model Explanation

This chapter presents a step-by-step explanation of the 2D simplified model. The model utilises the Newton-Raphson method to establish the equilibrium between internal and external forces within the net at a specific point in time. This involves making an initial guess and then iteratively refining it until convergence is achieved. Convergence indicates that the system has reached equilibrium, accounting for external influences, internal forces, deformations, and the shape of the system. The residual force is compared to the external force. If the ratio between the two is below a predefined threshold ϵ, the system is defined as 'converged'. Figure 4.6 shows the flowchart of the process.

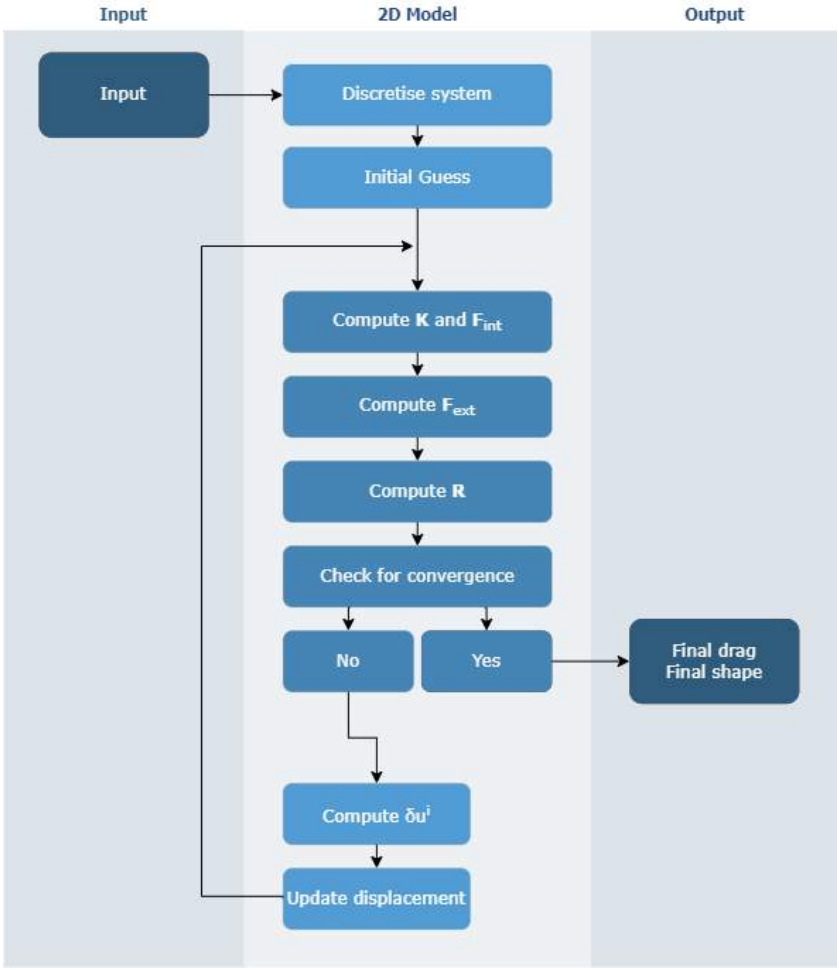

Figure 4.6: Flowchart of 2D simplified model

Model input variables

The first step in the model is defining the essential inputs. As the model starts with defining the shape of the model at a specific point in time, parameters such as the length of the system, the positions of the vessels and the direction of the speed through water (STW) are important. After the definition of the shape of the model, this shape serves as the basis for the calculation of the drag experienced by the system while moving through water. In this calculation, key input variables are the dimensions of

the net, the different drag coefficients for different angles of attack (AoA) and the speed through water magnitude. The dimensions of the net are depicted in the net depth, the twine diameter and the mesh size. Additional information such as wave height and wave period contributes to incorporating an additional force generated by the waves. Lastly, the number of segments and the maximum number of iterations play an important role in the model's functionality and computational efficiency. Increasing the number of segments and raising the maximum number of iterations enhance the model's accuracy, though this also extends the computational time.

The input variables are as follows:

- Net length: the length of the net on the water surface excluding the towing cable length [m]
- Net depth: the depth of the net in the water [m]
- Net mesh size: the distance between two consecutive twines [m]
- Net twine diameter: the diameter of twine [m]
- Net material stiffness: the resistance of the net material to deformation [Pa]
- Towing cable length: the length of the cable used to tow the net [m]
- Towing cable stiffness: the resistance of the towing cable to deformation [Pa]
- Vessel positions: the locations of the vessels towing the net
- Speed Through Water magnitude: the speed of the vessel relative to the water [m/s]
- Speed Through Water direction: the direction of the vessel's movement relative to the water [degrees]
- Wave height: the vertical distance between the crest and trough of a wave [m]
- Wave period: the time it takes for two consecutive wave crests to pass a fixed point [s]
- Water density: the mass per unit volume of seawater [kg/m^3]
- Drag coefficients per Angle of Attack: coefficients that describe the resistance experienced by an object moving through water at various angles
- Number of segments: the number of discrete sections the net is divided into
- Maximum number of iterations: the maximum number of times the model's calculations are repeated to refine results

System discretisation

Now that all variables are defined, the system can be discretised. Looking at the total length of the net and the segment length, the net is divided into a number of segments of equal lengths, with a node on both sides. In this discretisation step, a matrix is generated containing specific information per segment such as the left and right nodes' numbers, the segment mass, net material stiffness multiplied by the cross-sectional area (EA) and segment length. While the first four variables in this matrix are consistent across all segments, the segment length may vary based on its position. Since forces in the system do not have to be evenly distributed, one segment's deformation may differ from another's, resulting in slight variations in their lengths.

Initial guess

The next step in the process is to make an initial guess which requires the vessel positions and the discretised system. The initial guess can be any shape that satisfies the boundary conditions, however, an initial guess that is close to the final equilibrium shape will take fewer iterations to solve the system. A predefined sag value is used to create a parabolic line starting at vessel one, passing through the sag value to vessel two. The starting and ending points of the line are fixed, while the other nodes have two degrees of freedom and can move in both X and Y direction until an equilibrium is found. An example of this initial guess is visualised in Figure 4.7.

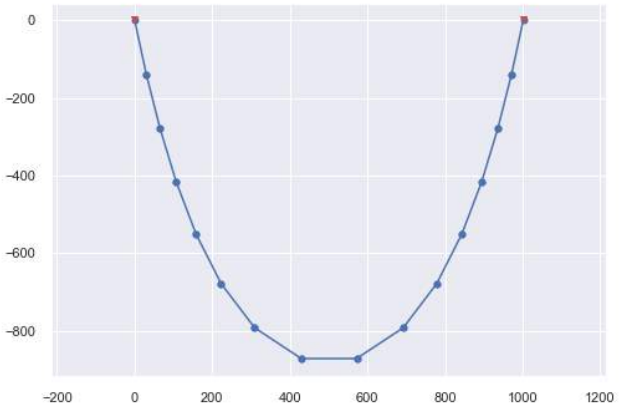

Figure 4.7: Initial guess

Compute stiffness matrix and internal force vector

Looking at the length of each segment, the elongation e of the segment can be determined compared to the initial length l_0. To do this, Equation 4.6 is used. In this equation, l is the new length in m.

$$e = \frac{l - l_0}{l_0} \tag{4.6}$$

Using this elongation and the stiffness properties of the net, the tension in the segment can be calculated using Equation 4.7. In this equation, T represents the tension in N, E is the Young's Modulus in Pa and A is the cross-sectional area in m^2.

$$T = EA * e \tag{4.7}$$

Subsequently, the stiffness matrix can be computed in local coordinates followed by a transformation of a local to a global coordinate system using Equation 4.8 and Equation 4.9.

$$\mathbf{K_{local}} = \frac{1}{l_0} * \begin{bmatrix} EA & 0 & -EA & 0 \\ 0 & T & 0 & -T \\ -EA & 0 & EA & 0 \\ 0 & -T & 0 & T \end{bmatrix} \tag{4.8}$$

$$\mathbf{K_{global}} = \mathbf{TKT}^T \tag{4.9}$$

The internal force vector, which will be used later to determine the residual force, is computed from the internal force matrix which is computed by Equation 4.10.

$$\mathbf{F_{int}} = T * \begin{bmatrix} -cos & -sin \\ cos & sin \end{bmatrix} \tag{4.10}$$

This interior force matrix represents the internal forces in the x- and y-direction. The components will be used to construct the internal force vector F_i.

Compute external force vector

The next step is to determine the external force vector. The basis for this vector is the drag equation as introduced in Section 2.4. In this equation, the water density ρ, area A, drag coefficient C_D and velocity v are combined to calculate the drag on an object. This is shown in Equation 4.11.

$$F_D = \frac{1}{2} * \rho * A * C_D * v^2 \tag{4.11}$$

This equation is applied to each individual segment looking at the properties of that particular segment. This involves considering the specific length of the segment and at what angle it is oriented relative to

the incoming current. For the area used in the equation the length, depth and solidity are of importance. Because of the force acting on the net, an elongation occurs which can influence the area. However, looking at Equation 4.12, using an elongation factor in which the initial length is compared with the new length, cancels out the new length from the equation.

$$A = d * l * \left(\frac{l_0}{l}\right) * S_n \tag{4.12}$$

To determine the right drag coefficient for each segment, the orientation of the segment relative to the incoming current is of importance. This angle of attack determines the drag coefficient that is used for that segment, based on the provided input values.

Compute residual force

An equilibrium occurs when the external forces are equal to the internal forces. This disparity is depicted by the residual force. The residual force compares the force generated by the stretching of the net, the internal force, with the external force acting on that segment. This is done by examining the x- and y-components separately. The comparison is depicted in Equation 4.13. In this equation, R is dependent on **u**, which is the vector containing all locations of the nodes of the system.

$$\mathbf{R}(\mathbf{u}) = \mathbf{F_{ext}} - \mathbf{F_{int}} \tag{4.13}$$

Check for convergence

Now that the difference between external and internal force has been determined, it can be examined whether the system is in equilibrium. To do this, the residual force is compared to the external force. If the ratio between the two is below a predefined threshold ϵ, the system is defined as 'converged'. The value of ϵ influences the accuracy of the model, and hence the computational demand of the model. A very low threshold means the system has to loop through many iterations to find the exact equilibrium state, making it more accurate but with a high computational demand. A higher threshold reduces the computational time but results in a less accurate model. The threshold ϵ is set to $2e-3$. For illustration, if the external force on the system is 35 tonnes, the inaccuracy would be 0.07 tonnes. Equation 4.14 presents the equation to calculate the convergence.

$$CONV = \frac{||\mathbf{R}(\mathbf{u^i})||_\mathbf{2}}{||\mathbf{F_{ext}}||_\mathbf{2}} \leq \epsilon \tag{4.14}$$

In the case the convergence ends up being higher than the threshold, it means there is no equilibrium in the current state. For the next iteration in finding the equilibrium, a slight change in the current system shape is computed.

Compute increment & update displacement

As the system is not in equilibrium yet, it requires a slight change in shape for the next iteration. This adjustment involves utilising the stiffness matrix and the residual force vector corresponding to the specific shape, as depicted in Equation 4.15.

$$\delta\mathbf{u^i} = \mathbf{K}(\mathbf{u^i})^{-\mathbf{1}}\mathbf{R}(\mathbf{u^i}) \tag{4.15}$$

Inverting the stiffness matrix may lead to problems in the model because of singularity in the matrix. A matrix being singular means that the determinant of the matrix is zero which makes it impossible to invert the matrix. This leads to error in the Python code. When this occurs, no outcome is generated, and the specific case is skipped. To increase the robustness of the model, the number of failed cases should be as low as possible. To minimise this number of failed cases, a check is implemented to see whether the stiffness matrix is singular. If it proves non-invertible, a small amount of noise is added to the matrix. This noise, while negligible in its impact on the final results, enables the computation of increments for following iterations.

Subsequently, this $\delta\mathbf{u^i}$ is added to the original location vector, resulting in a new u-vector, showing the locations of all nodes in the new situation. This is depicted in Equation 4.16. Using the new shape of the system, a new iteration can be started by jumping back to 'Compute Stiffness matrix and Internal

Force vector' followed by the repitition of all subsequent procedures. This iterative loop continues until an equilibrium state is achieved.

$$\mathbf{u}^{u+1} = \mathbf{u}^{i} + \delta\mathbf{u}^{i} \tag{4.16}$$

Model output

After convergence, the model is ready to show the output for the given timestep. Figure 4.8 shows the solution for a timestep with a vessel separation of 1500 meters, a current speed of 0.8 m/s in negative y-direction, a cable length of 600 meters each and a system length of 2000 meters. The second situation, as depicted in Figure 4.9 has a vessel separation of 1250 meters and a current speed of 0.8 m/s under a different angle of attack. The plots show the number of iterations it took to reach convergence and the lengths after deformation are depicted.

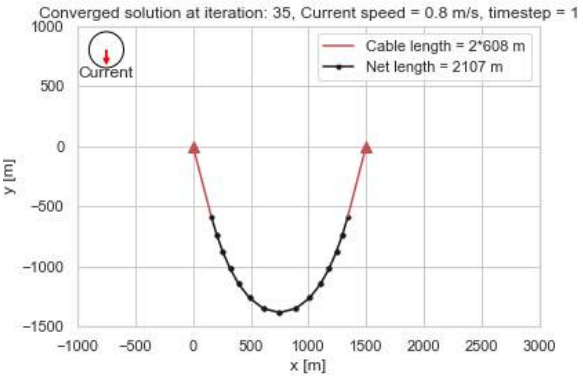

Figure 4.8: Model output situation 1

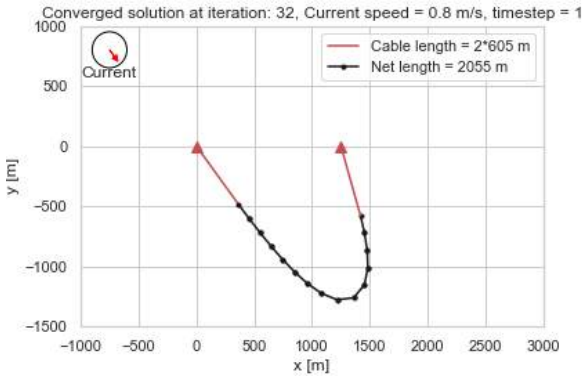

Figure 4.9: Model output situation 2

Besides generating a plot of the current situation, the total drag on the system is stored in a dataframe. The calculated drag force on the system in situation 1 is 79.2 tonnes. The total drag force in situation 2 is 58.5 tonnes. This difference is caused by the difference in shape. In situation 2, bigger parts of the net are in small angles of attack, meaning the drag on these segments is lower compared to the drag on the segments in situation 1.

4.3. Drag Coefficients Before Experiment

As the modelling phase is independent of the experimental phase, an estimation of drag coefficients needs to be done first. These estimates will inform the testing process and initial results.

Assuming that the net is towed through the water at an angle of attack of 90 degrees, all vertical and horizontal twines are towed perpendicular through the water. As stated in (Jiménez et al., 2023), the normal drag coefficient is estimated at 1.71. When the net is towed through the water at an angle of attack of zero degrees, there is a difference between the drag on the horizontal and the vertical twines. The horizontal twines are pulled in parallel through the water, undergoing forces dependent on the drag coefficient at an angle of attack of zero degrees. However, all vertical twines, being small cylinders, are still towed perpendicularly through the water, independent of the angle of attack. The assumption is that the vertical twines do not influence each other, meaning there are no shielding effects.

Using this principle, an angle of attack of 90 degrees, means 100% of the twines generate a drag dependent on a drag coefficient of 1.71. An angle of attack of zero degrees means only the vertical twines generate drag depending on a drag coefficient of 1.71. The other twines, the horizontal twines, generate a drag dependent on the tangential drag coefficient of a cylinder. This tangential drag coefficient is estimated at 0.011([DNV], 2014). Depending on the angle of attack, the drag coefficient for the horizontal twines will approach 1.71 as the angle of attack increases. For the vertical twines, it remains constant at 1.71. For an angle of attack of zero degrees, this results in a drag coefficient of $1.71/2 + 0.011/2 = 0.86$. This relationship is depicted in Table 4.4, presenting the angles of attack, the

contribution of the normal drag coefficient (x) and the matching drag coefficient. The result is visualised in Figure 4.10.

AoA	90	...	AoA	...	0
x	1	...	$\frac{1+sin(AoA)}{2}$	...	0.5
C_d	1.71	...	$1.71 * x + 0.011 * (1 - x)$	...	0.86

Table 4.4: Drag coefficient per angle of attack assumed prior to experimental testing

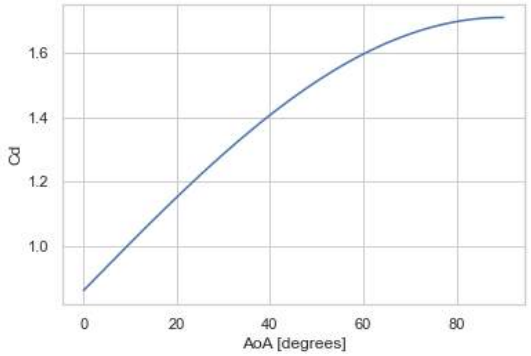

Figure 4.10: Drag coefficient assumed prior to experimental testing

4.4. Wave Implementation

Zooming in on waves shows that a wave consists of particles following a circular path with a velocity in positive direction in the crest of the wave and a velocity in negative direction in the trough of the wave. This is very noticeable at sea: if you are located at the trough of the wave, you are pulled back towards the incoming crest, when the crest arrives it throws you back in the direction of propagation. The shape of this circular motion depends on the water depth. In deep water, the wave is not influenced by the seabed which results in a circular motion. In shallow waters, the seabed forces the circular motion to a more orbital rotation as shown in Figure 4.11.

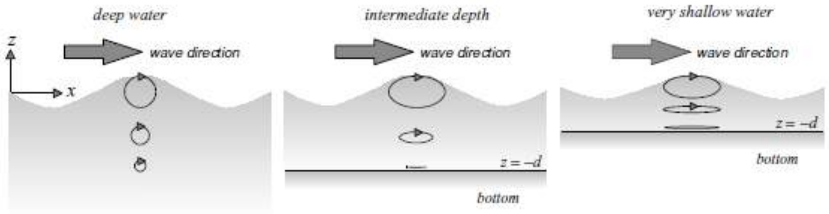

Figure 4.11: The orbital motion of water particles in deep water, intermediate-depth water and shallow water (Holthuijsen, 2007)

The particle velocities in the wave can be determined using the velocity potential function of a propagating wave as shown in Equation 4.17 where ω is the angular frequency of the wave in $[s^-1]$, a is the wave amplitude in $[m]$, k is the wavenumber in $[m^-1]$, d is the depth in $[m]$ and z is the depth at the point of interest. The derivation of this velocity potential results in the horizontal and vertical particle velocities, denoted as u_x and u_z respectively. The derived results are presented in Equation 4.18 and Equation 4.19.

$$\phi = \hat{\phi} * cos(\omega t - kx) \quad with \quad \hat{\phi} = \frac{\omega a}{k} \frac{cosh[k(d+z)]}{sinh(kd)} \tag{4.17}$$

$$u_x = \hat{u_x} * sin(\omega t - kx) \quad with \quad \hat{u_x} = \omega a \frac{cosh[k(d+z)]}{sinh(kd)} \tag{4.18}$$

$$u_z = \hat{u_z} * cos(\omega t - kx) \quad with \quad \hat{u_z} = \omega a \frac{sinh[k(d+z)]}{sinh(kd)} \tag{4.19}$$

Because the operations happen in very deep water, the assumption can be made that $kd \to \infty$. This simplifies the equations for both u_x and u_z to $u_x = u_z = \omega a$, and therefore $u_x = \frac{2\pi a}{T_p}$. In this equation, a equals two times the significant wave height in $[m]$ and T_p represents the wave period in $[s]$. This results in the formula to determine the particle velocity as stated in Equation 4.20.

$$u_x = H_s * \frac{\pi}{T_p} \tag{4.20}$$

The orbital motions of water particles causes that a net pulled through water experiences different velocities at different water depths. These velocities result from a combination of the speed through water (current speed and sailing velocity) and the particle velocity. Combining these velocities yields a relatively higher velocity at the water surface ($stw + u_x$) and a lower velocity at the bottom of the net due to the particle velocity in the opposite direction ($stw - u_x$), as illustrated in Equation 4.21. In the drag formula, as presented in Equation 2.5, this velocity is squared. Therefore, taking only the average speed through water leads to incorrect values. Consequently, the velocity is integrated over the depth of the net as depicted in Equation 4.22, to obtain the velocity across the entire depth of the net.

$$V = stw + u_x \left(1 - \frac{2z}{d}\right) \tag{4.21}$$

$$\int_0^d V^2 \, dz = \int_0^d \left(stw + u_x \left(1 - \frac{2z}{d}\right)\right)^2 dz = d\left(stw^2 + \frac{1}{3}u_x^2\right) \tag{4.22}$$

Operations of System 03 only happen when the environmental conditions fall within certain predefined limits (max H_s of about two meters) to prevent high loads on the system and to ensure that plastic does not overtop the system. However, there are always waves that can influence the system. The presence of waves can cause varying loads on the system, dependent on their wave height and wave period. These environmental conditions, like significant wave height and wave period, are considered in the model.

The implementation of the wave loads in the 2D model is conducted by using the final drag formula as stated below in Equation 4.23.

$$F_d = \frac{1}{2}\rho C_d S_n l_0 d \left(stw^2 + \frac{1}{3}\left(H_s \frac{\pi}{T_p}\right)^2\right) \tag{4.23}$$

5

Model Integration and Validation

Now that both the modelling and experimental phases have been completed, the results of these two phases can be integrated. This integration process is discussed in detail in Section 5.1. Before utilising the model, it is essential to validate it by comparing real-life situations with simulations generated by the model. To quantify this validation, various validation methods are discussed in Section 5.2. The data used for this validation is introduced in Section 5.3. Section 5.4 presents the model results and compares them with measurements as well as the results obtained from the 3D Finite Element model. Finally, Section 5.5 presents the validation and summary of the results.

5.1. Integration

For the integration of the modelling phase and the experimental phase, the results from both phases are combined. The experimental results will be integrated into the 2D simplified model. Firstly, the drag coefficients as presented in Subsection 3.6.2 are used as a model input. Before the experiment, an estimation for drag coefficients has been done as discussed in Section 4.3. Because the experimental angles of attack are determined starting from 5 degrees, a drag coefficient of 0.011 is used for angles of attack between 0 and 5 degrees, assuming fully parallel flow. This is the same as in the case of the estimated drag coefficients. Figure 5.1 shows a plot of the estimated drag coefficients and the drag coefficients from the experiment.

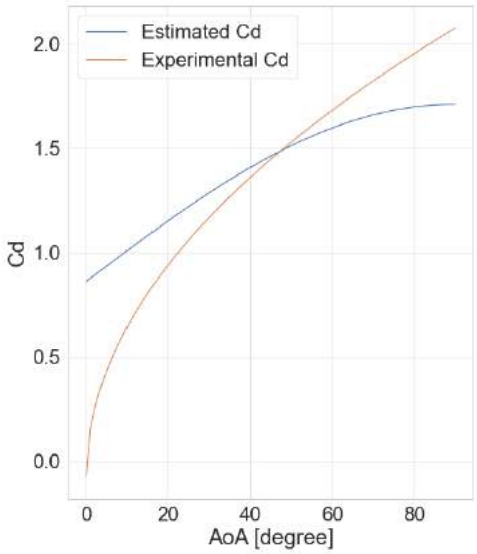

Figure 5.1: Estimated drag coefficients and experimental drag coefficients

As observed in the plot, there are differences between the estimated and experimental drag coefficients.

At lower angles of attack, the estimated drag coefficient exceeds the experimental values. This difference can be attributed to the exclusion of the shielding effect in the estimated drag coefficients. This shielding effect reduces the drag coefficient at low angles of attack.

Now that the experimental drag coefficients are implemented in the model, the results can be generated and compared with validation data and OrcaFlex results. The input data and validation data that is utilised are elaborated on in the following section.

5.2. Validation Method

In order to make an objective comparison between the 3D finite element model and the 2D simplified model, both models will be compared with the measurements done in the Great Pacific Garbage Patch. Three different methods to compare the error between the measurements and the predicted values are the Mean Absolute Error (MAE), the Root Mean Square Error (RMSE) and the Mean Absolute Percentage Error (MAPE).

The Mean Absolute Error quantifies the average absolute differences between the measured and the predicted values as shown in Equation 5.1 (Hodson, 2022). In this equation y_j^m and y_j^p represent the measured and predicted values, respectively. n is the total number of predictions. The method works intuitively and gives equal weight to all errors, therefore it is less sensitive to outliers.

$$MAE = \frac{1}{n}\sum_{j=1}^{n}|y_j^p - y_j^m| \tag{5.1}$$

The Root Mean Square Error is computed as in Equation 5.2 (Hodson, 2022). This equation squares the differences between the measured and the predicted values, giving it a more significant weight to larger errors. This method penalises large errors more heavily than smaller errors, therefore it is more sensitive to outliers.

$$RMSE = \sqrt{\sum_{j=1}^{n}\frac{(y_j^p - y_j^m)^2}{n}} \tag{5.2}$$

The Mean Absolute Percentage Error expresses the error between the measured and the predicted value as a percentage of the measured value. If the measured values are small, the MAPE will be relatively large and therefore sensitive to outliers in these cases. So errors at low measured values will significantly impact the MAPE resulting in a misleading result. The MAPE is computed as in Equation 5.3 (Khair et al., 2017).

$$MAPE = \frac{1}{n}\sum_{j=1}^{n}\left|\frac{y_j^p - y_j^m}{y_j^m}\right| * 100\% \tag{5.3}$$

Because of this misleading result, MAPE will not be taken into account, leaving the decision between the MAE and RMSE. As previously indicated, the RMSE squares the difference between the measurement and the predicted value resulting in a significant influence of large errors. Because both the developed model and the OrcaFlex model are simplifications of reality, certain aspects that are not included in the models may cause a large error which will increase the total RMSE significantly. For instance, a period with high, short waves can cause peak loads in the measurements that remain unacknowledged in the model outputs. To compensate for an increase in the total error, the MAE will be employed that gives equal weight to all errors.

5.3. Input and Validation Data

Throughout the operations of The Ocean Cleanup's system in the Great Pacific Garbage Patch, various sensors collected data. This section introduces the two distinct datasets acquired. On the one hand, sensors on board the vessels collected data regarding vessel motions and environmental data. On the other hand, sensors are installed on the system itself, collecting data such as coordinates. In both datasets, the information is presented in five-minute timesteps, reflecting the 5-minute averages. However, the time signal is not this continuous throughout the entire dataset. This is associated with the execution of the operational procedures. Factors such as bad weather forecasts or encountering

regions with a low plastic density may necessitate the crew to temporarily suspend the system operations. These periods are used to transport the system from A to B or to safeguard the system against severe weather conditions. Sensor deactivation during these downtime intervals induces gaps in the time signal. In order to facilitate clear signal visualisation, these gaps are disregarded in the subsequent plots within this chapter and the following chapters, potentially leading to a discontinuous time signal on the x-axis.

Vessel data

The first dataset is a combination of information about the system configuration, environmental information and vessel information. The dataset starts in November 2022 and ends in September 2023, including trips 12, 13, 14, 15, 16_S2c, 16_S3 and 17. Key signals that are used as input for the model are for example the length of the system, the vessel separation, the speed through water and the significant wave height. The data used to validate the model outputs include the measured loads on the winches aboard the vessels. A comprehensive overview with descriptions of all input signals can be found in Appendix A.

Below, Figure 5.2 present the results of the measurements conducted in the Great Pacific Garbage Patch during trip 17. The probability density functions for significant wave height, wave period, speed through water, effective span and the load on the winch are presented. These PDFs illustrate the probability distribution of each variable, showing the relative likelihood of observing different values based on the collected data. In the last plot, the load on winch is plotted versus the speed through water. This is an important plot for the validation of the 2D simplified model. The validation data for the other trips can be found in Appendix A.

As shown in the plot, the most common speed through water for Trip 17 is approximately 0.75 m/s, which is typical for all trips. The typical wide span is evident at around 1300 meters, or 60% of the system length, and is consistent across all trips. The environmental conditions during the trips are calm, with a predominant wave height of about one meter and long wave periods of approximately 13 seconds.

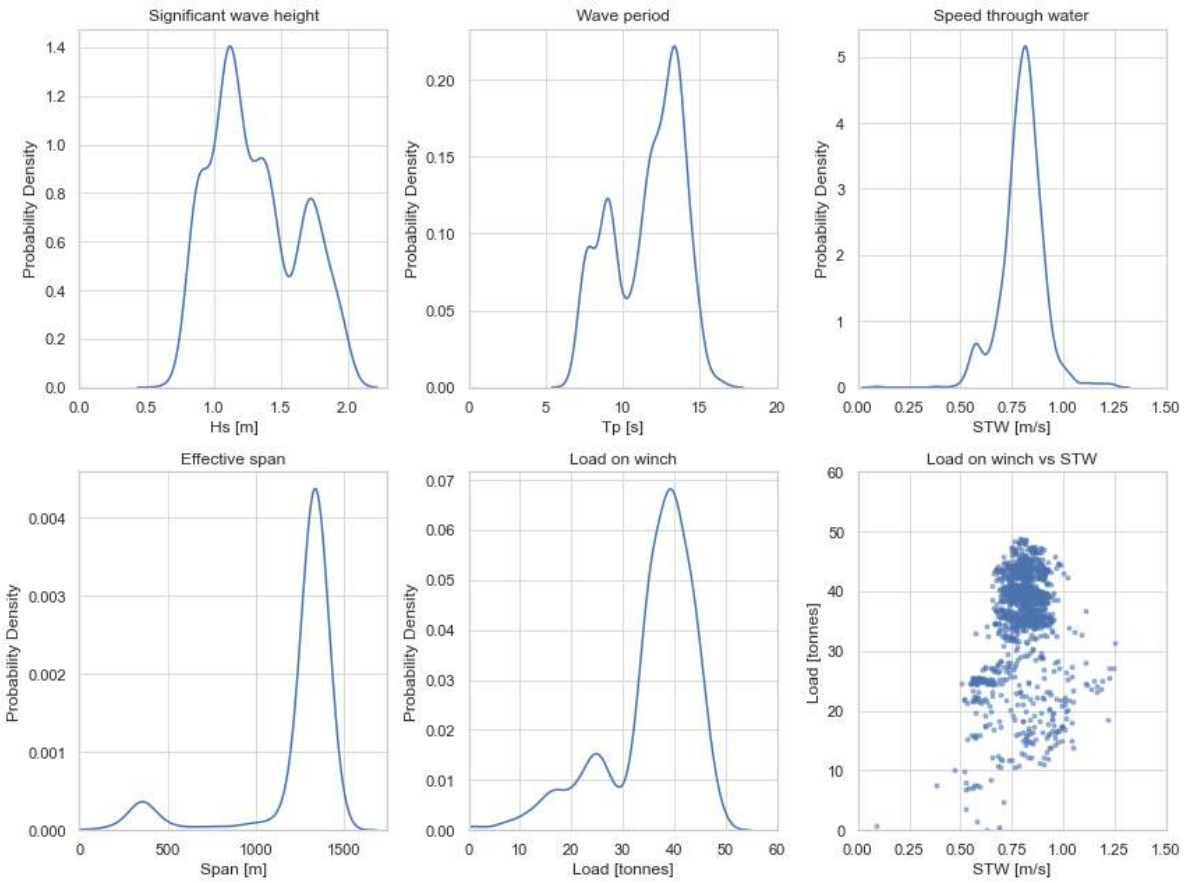

Figure 5.2: Trip 17 GPGP measurements

Tracker data

Since the deployment of System 002, the system has been equipped with tracker sensors logging the location of the system. The tracker data set starts in August 2021 and ends in November 2023 and presents the coordinates of the system in a five-minute interval. The trackers are deployed at three points: the opening of the retention zone and at the front of the first wing module on both wings. At every timestep, a longitude and a latitude coordinate for each tracker is presented, serving to validate the model shape through comparison with the tracker data after conversing the coordinate to a distance in meters by multiplying it with 111,319, based on the Great Circle Distance as in (Carter, 2002).

5.4. Results

Prior to commencing the validation process, the model resolution is defined in Subsection 5.4.1. Subsequently, Subsection 5.4.2 presents the results of Trip 17, while Subsection 5.4.3 provides an overview of all results combined.

5.4.1. Model Resolution

Before presenting the results of the 2D simplified model, a decision has to be made on the resolution of the model. The trade-off between computational time and accuracy is an important parameter in the functioning of the model. The higher the resolution, the higher the accuracy, but also the higher the simulation time. Figure 5.3 presents the result of Trip 17, showing a clear increase in simulation time per time point for an increasing number of segments. The error of the model decreases slightly with an increase in the number of segments. The presented error is the MAE divided by the mean load in the trip. As depicted in the plot, an increase in simulation time occurs after a total of 15 segments. For this reason, the following plots show the results where the input for the model is a total number of segments of 15.

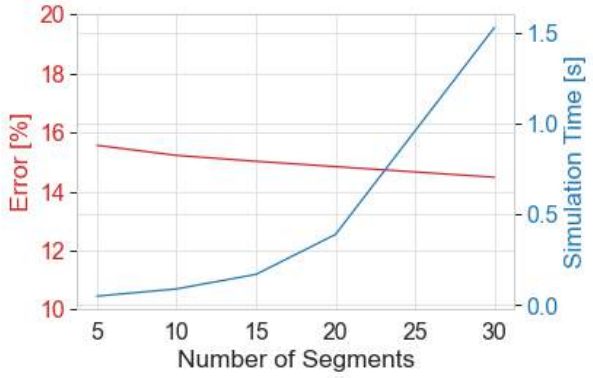

Figure 5.3: Error and simulation time versus number of segments

5.4.2. Trip Results

By utilising the GPGP measurement data as input for the 2D model, the total loads on the system are computed. These calculated loads can then be compared to the measured loads at specific time points, as well as to the results obtained from the OrcaFlex regression analysis as introduced in Section 4.1.

As an example, the results of one individual trip are shown first. For a clear comparison, the calculated loads are plotted against the speed through water, as depicted in Figure 5.4. In this plot, the blue dots represent the measured loads on the winch on board one of the vessels using a Running Line Monitor (RLM). The orange dots represent the calculated 3D Finite Element model results divided by two and the green dots the 2D model results divided by two. By dividing the total calculated loads by two, the total load is averaged over the two winches. Subsequently, this averaged load is compared with the measured load on one of the winches on board the vessel.

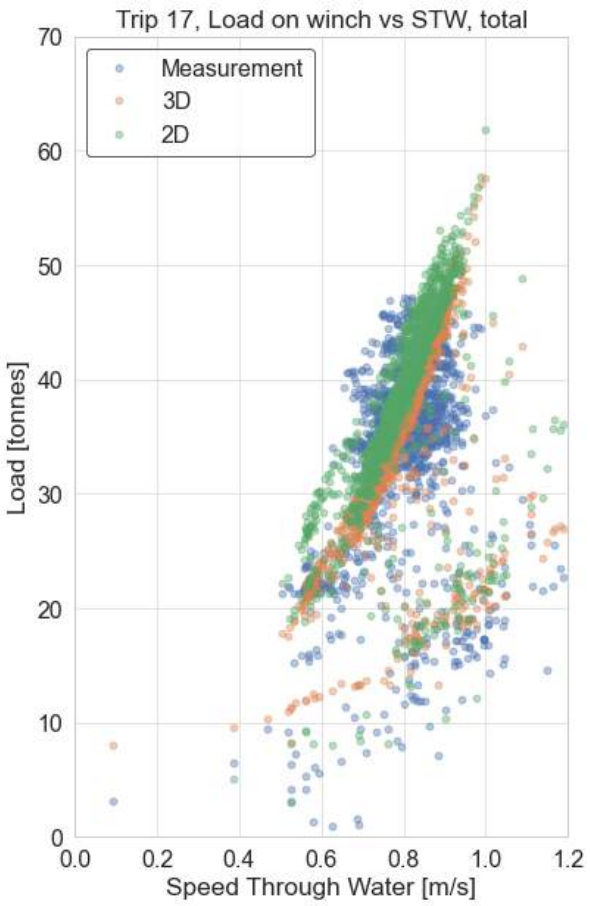

Figure 5.4: Trip 17, comparing results of GPGP measurements, OrcaFlex model and Python model

The following plot depicts the probability density function of the measured loads and calculated loads from the 3D finite element model and the 2D model.

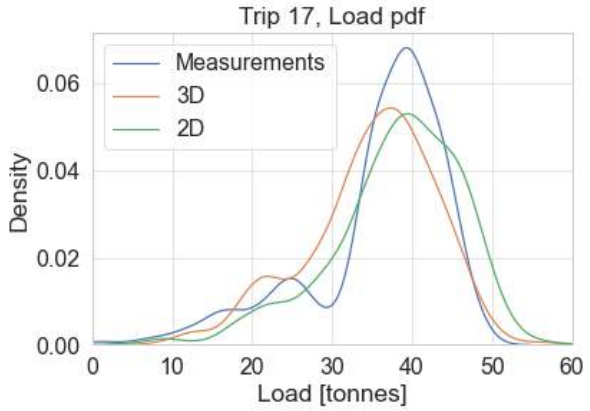

Figure 5.5: Probability Density Function of the load of Trip 17

To get a better understanding of the dots in the first plot, the data points from Trip 17 are divided over small span and wide span. Figure 5.6 shows the probability density function of the span during Trip 17. The graph clearly shows two situations occurring the most: operation in small span at around 300 meters and operation at wide span at around 1340 meters. Looking at this graph and at the PDF's of the spans of the other trips, as plotted in Appendix B, the separation between small and wide spans is determined at a span-over-length ratio of 0.35.

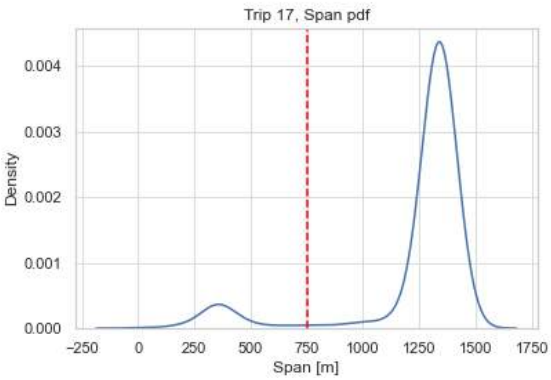

Figure 5.6: Probability Density Function of the span of Trip 17

This separation results in the following two plots showing model results per span range:

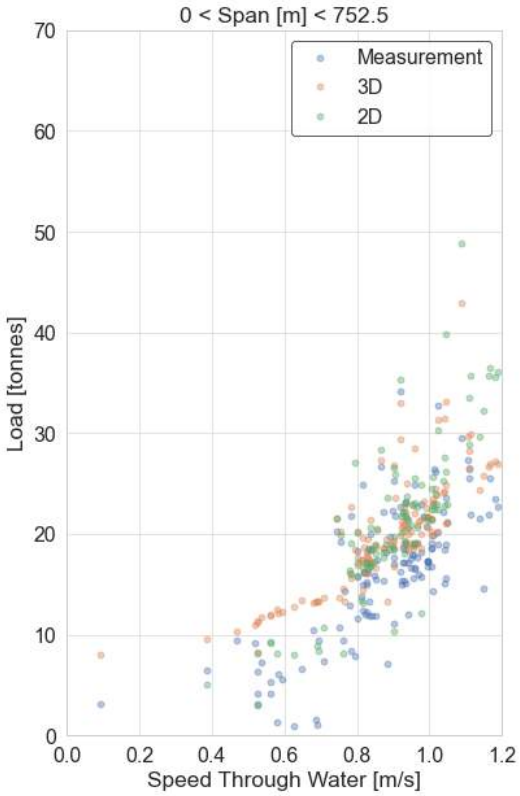

Figure 5.7: Trip 17, small span results

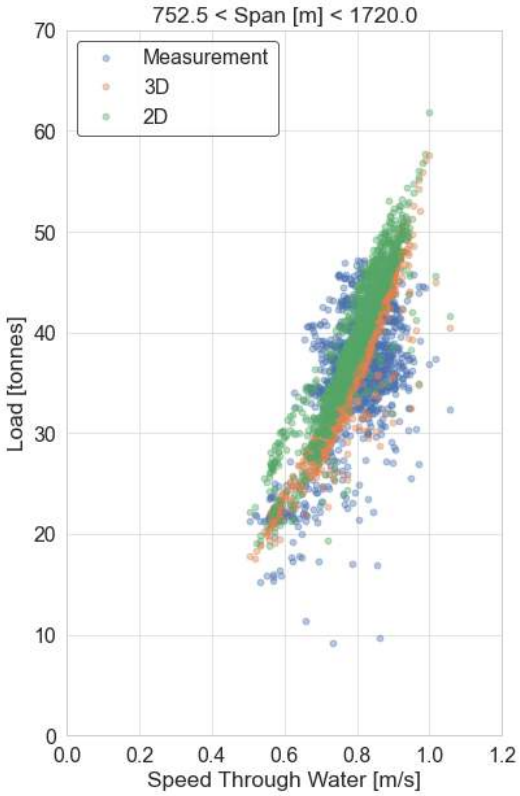

Figure 5.8: Trip 17, wide span results

5.4.3. Results Overview

As The Ocean Cleanup System 03 operated multiple times in the GPGP, multiple trips are recorded as mentioned before. After a normalisation of the calculated loads, the results of all trips combined are shown in the PDF of Figure 5.9.

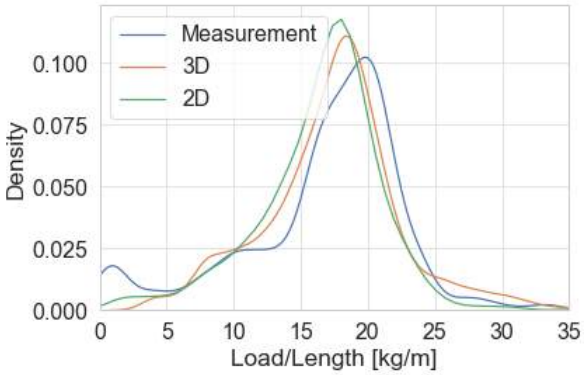

Figure 5.9: Probability Density Function of load per length, all trips combined

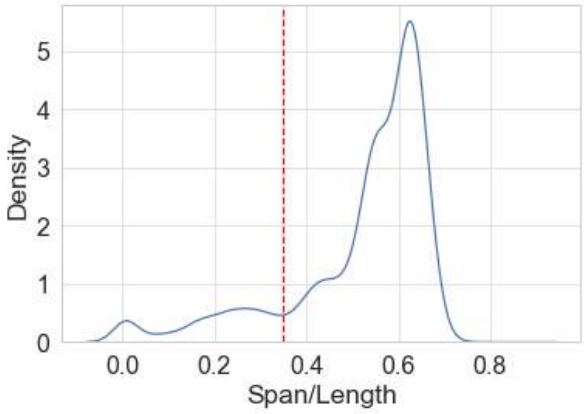

Figure 5.10: Probability Density Function of span-over-length, all trips combined

Figure 5.10 shows the PDF of the span-over-length of the results of all trips combined. As depicted in this plot, the governing span-over-length ratio is about 0.6. This means for example for Trip 15, where the system length is 1773 meters, the most occurring system configuration is at a span of around 1050 meters. The separation between small and wide span is set at 0.35 as mentioned above. The normalised loads for small span and wide span are depicted in Figure 5.11 and Figure 5.12, respectively.

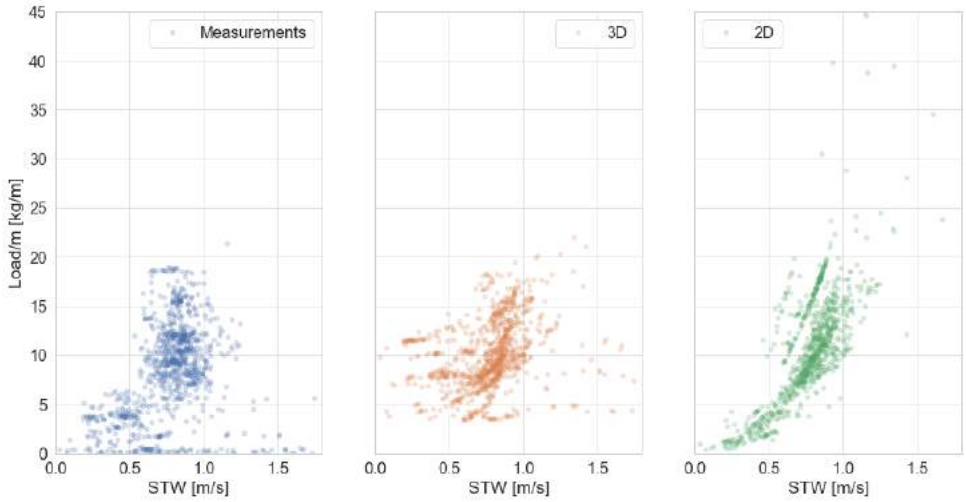

Figure 5.11: Small span results

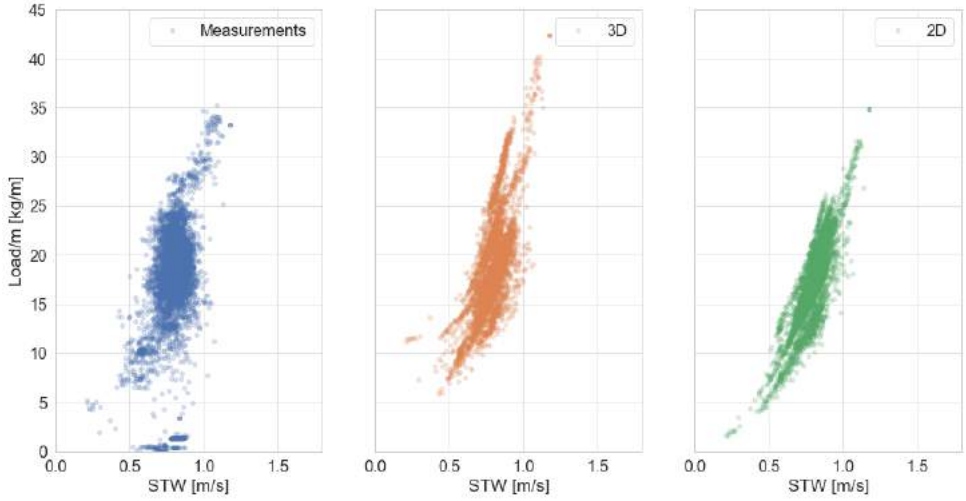

Figure 5.12: Wide span results

5.5. Validation

As introduced in Section 5.2, the Mean Absolute Error is a way to quantify the functioning of the model and to make a comparison between the 3D results and the 2D results. To combine all the different trips with varying system lengths and with that varying loads, the errors are presented as Mean Absolute Error as a percentage of the mean load for each trip. These errors are presented in Table 5.1.

	3D	**2D**
MAE Total span	22.1 %	21.9 %
MAE Small span	49.0 %	64.8 %
MAE Wide span	20.1 %	18.7 %

Table 5.1: Mean Absolute Error as a percentage of mean load

The table shows that the models perform similarly over a total number of cases of 7026. The results show that the errors for small span end up relatively high in comparison to wide span. This discrepancy is mainly due to the difficulty in accurately predicting loads on the system in small span using the models. The preferred operational configuration is to sail in wide span at steady speed and in calm weather

conditions. However, in the event of changing weather conditions, the need for system manoeuvring, or when the system has to transport from point A to point B at higher velocities, sailing in small span might become necessary. However, such actions could induce asymmetry in the system or lead to unpredictable situations, resulting in divergent loads. The wide span errors are significantly lower where the 2D and the 3D models perform similarly.

For a comprehensive understanding of the error distribution in both models, the errors are depicted in Figure 5.13. The green lines represent the errors of the 2D model, while the orange lines represent those of the 3D model. These errors reflect the difference between the predicted load per meter and the measured load per meter, enabling a comparison across various system lengths. As can be seen in the plot for low speed through water, the errors of the 3D model are larger than for the 2D model. This observation is consistent with the findings in Figure 5.11 and Figure 5.12. Both graphs illustrate that as velocity approaches zero, the trend of the measured loads converges to zero as expected. This trend is also observed in the plots for the 2D simplified model. However, for the 3D Finite Element model, the predicted loads at low speeds through water do not converge to zero as closely as expected based on the trend. This discrepancy is clearly illustrated in Figure 5.13.

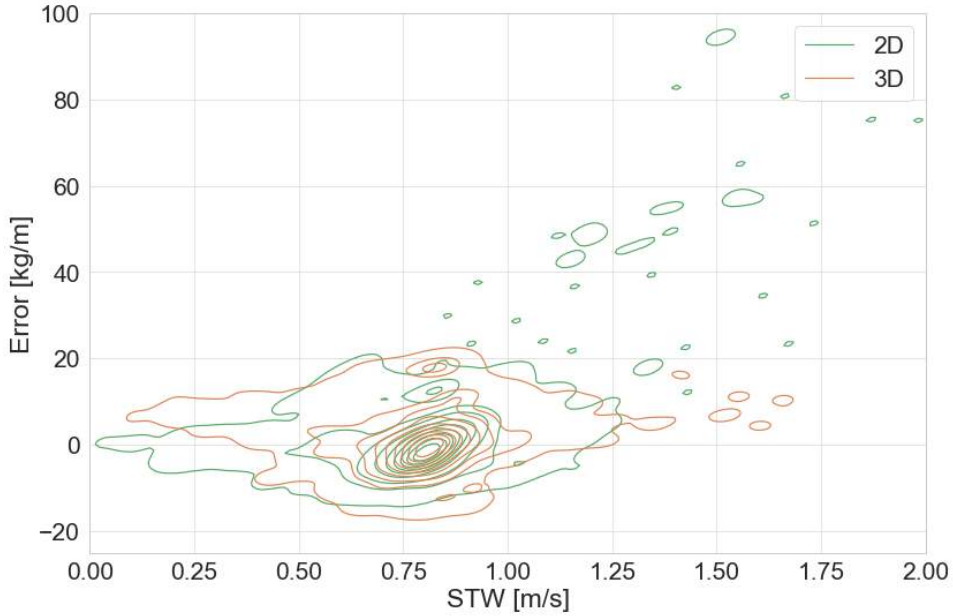

Figure 5.13: Predicted load - measured load in kg/m versus speed through water

However, the accuracy of the 2D model diminishes significantly when the speed through water exceeds approximately 1.25 m/s. This loss of precision is likely due to the elongation of the system in the 2D model at these higher velocities, which depends on the stiffness settings implemented. As the speed increases, loads rise exponentially, leading to greater elongation and an increase in the projected area. However, at higher velocities, the growth in the measured loads tends to shift from exponential to linear, as can be seen in Figure 5.12. This shift occurs because the increased tension in the net at high speeds causes the net to deform, lifting the lower bar and thus reducing the projected area, leading to lower loads. This phenomenon is not accounted for in the 2D model, leading to increased errors at higher velocities. On the other hand, the errors in the 3D model remain consistently low across various speeds. This suggests that while the 2D model is more effective at lower speeds, the 3D model provides better performance at higher speeds. Nevertheless, at speeds ranging from 0.5 to 1.0 m/s, which are the predominant operating velocities, both models show comparable levels of error.

Shape validation

The shape of the system determines the angle of every segment relative to the incoming current and with that, the shape is important for the total drag force. The expected shape in general circumstances is the catenary shape. This is a U-shape that perfectly divides the loads on the net over the entire

system. Figure 5.14 shows an image of the radar on board one of the towing vessels during a trip in the GPGP. The yellow shape is compared with the perfect catenary shape in black. As seen in the plot, the shapes match perfectly. This is in the case that the system is sailing in a straight line under calm environmental conditions. However, manoeuvring or side currents for example can change the perfect catenary shape.

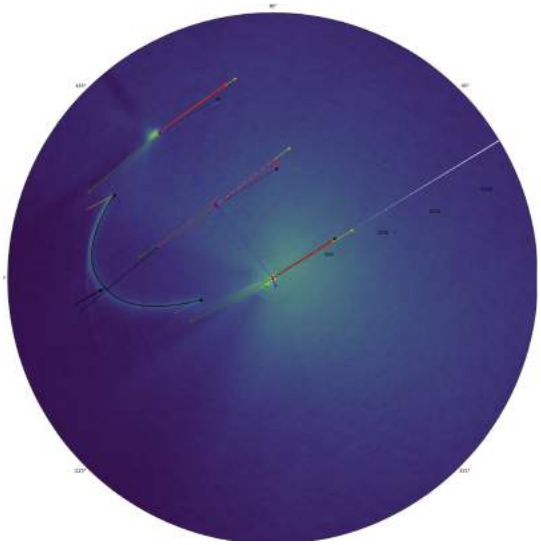

Figure 5.14: Image of radar on board of The Ocean Cleanup towing vessel comparing System 03 with the catenary shape

Tracker data is used to compare the real-life situation to the output of the model. For a clear comparison, two angles are introduced: γ_p and γ_s. These angles are a result of drawing an imaginary triangle from the opening of the retention zone to the front of the first wing module at starboard and at portside. The formed triangle shows γ_p at portside and γ_s at starboard as illustrated below.

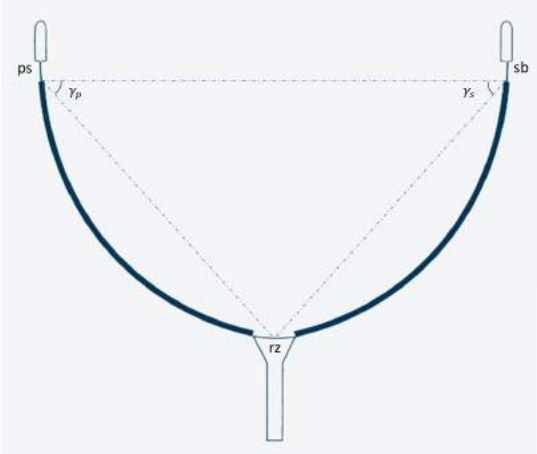

Figure 5.15: The definition of γ_p and γ_s

The two defined angles from Trip 17 as calculated from the tracker measurements are presented in Figure 5.16a. When comparing the angles with the angles from the model, as presented in Figure 5.16b, a slight difference can be seen. The model results show small differences between γ_p and γ_s, meaning the system is modelled close to symmetry in most of the cases. The tracker data shows a slight angle difference for most of the cases, meaning the system is not completely symmetric. Reasons for this could be side winds, side currents, manoeuvring or slack in the cable.

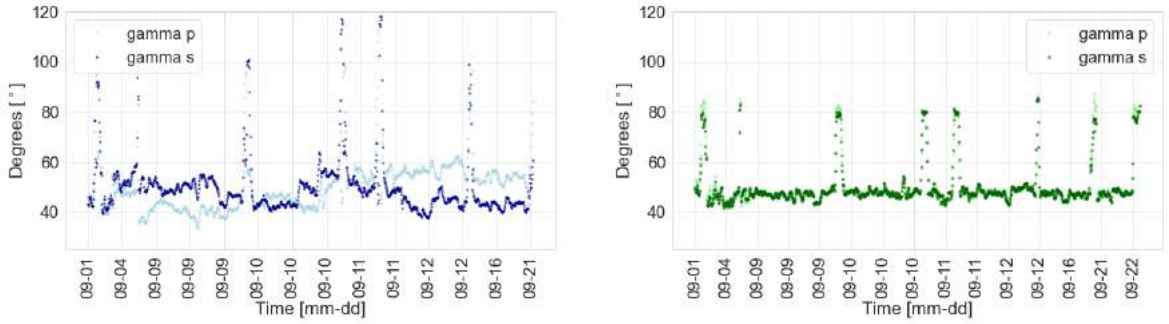

(a) Tracker data

(b) Model output

Figure 5.16: Shape validation by comparing γ_p and γ_s for tracker data and model output

Robustness

As mentioned in Chapter 4, the robustness of the model is important for the reliability of the model. A high robustness means that for all inputs, the model generates a prediction of the loads. Table 5.2 presents the number of 'successful cases'. For all the cases that are not 'successful', singularity in the matrix could have caused an error in the code, or the system could not converge to an equilibrium in the given maximum number of iterations. The table shows higher robustness for wide span and lower robustness for the less common situations in small span.

	Total cases	**Successful cases**	**%**
Small Span	1017	954	93.8
Wide Span	6139	6072	98.9
Total	7156	7026	98.2

Table 5.2: Successfull cases of 2D simplified model

Regarding the robustness of the 3D model in OrcaFlex, a regression analysis provides results for all cases, allowing only a few situations to be simulated. These results are then used to predict outcomes in other scenarios. While OrcaFlex generates results for these selected cases with 100% robustness, many situations remain unsimulated.

Simulation time

In the results shown, the predicted loads generated by the 3D Finite Element model in OrcaFlex are compared with the predicted loads generated by the 2D simplified model in Python by looking at the error. Another interesting aspect to look at in comparing the two methods is by looking at the simulation time. As presented in Appendix C, the average simulation time of one simulation for the 2D model takes 0.14 seconds. This means simulating an entire trip takes a couple of minutes. A simulation in OrcaFlex consumes more time. Before a simulation can start, the 3D model needs to be modelled by implementing the required properties of the system. For the next step multiple simulations can run at the same time, taking approximately one week. By looking at the gathered results in these simulations, a regression analysis can be conducted to get the results as presented in the plots. All together takes about three weeks for the results of one net type. In the case that for example, the net type changes or the depth of the net increases, a new three weeks is required for a new regression analysis. This means the simulation time and flexibility of the 2D simplified model are way more beneficial than for the 3D model.

5.5.1. Results Summary

Before drawing conclusions, an overview of the model results for all trips is presented. A total of 7149 cases are simulated using the 2D simplified model. To execute the total of 7156 cases, 1012 seconds

are required, resulting in an average simulation time of 0.14 seconds per case. As mentioned in Chapter 4, it's important to note that the model's robustness is not at 100%. Occasionally, due to exceeding the maximum number of iterations or encountering singularity in the stiffness matrix, a particular case may be skipped, resulting in no generated result. Out of the total number of cases, 7026 were successfully completed, accounting for 98.2% of all cases.

The Mean Absolute Error is calculated as a percentage of the mean load and results in 21.9% and 22.1% for the 2D simplified model and the 3D Finite Element model, respectively. For the cases where the span over length ratio is smaller than 0.35, the small spans, the errors are 64.8% and 49.0% for 2D and 3D respectively. For the wide spans, the 2D model performs slightly better with an error of 18.7% where the 3D model scores an error 20.1%. As mentioned, the errors for small span are significantly higher than for wide span. This is due to the difficulty of predicting loads in small span, because of odd environmental conditions or manoeuvring operations. The results of all individual trips can be found in Appendix C.

Total number of cases	**Total simulation time**	**Simulation time per case**
7156	1012 s	0.14 s

Overall successful cases	7026	**2D error**	21.9%	**3D error**	22.1%
Small span successful cases	954	**2D error**	64.8%	**3D error**	49.0%
Wide span successful cases	6072	**2D error**	18.7%	**3D error**	20.1%

Table 5.3: Model results

6

Case Study and Results

The validation has demonstrated that the constructed model is both accurate and capable of rapid calculations, yielding quick results. For illustration, one of the trips is examined using this model. Section 6.1 delves into the details of Trip 17 and presents the model results. In Section 6.2, these results are analysed. Finally, Section 6.3 applies the model to determine the system limits necessary for offshore operations. This final step is applied not only to the current system but also to a potential future system.

6.1. Trip 17 Summary

Now that the model has been validated, the first steps can be taken towards the application of the model. As an example, in this chapter, one of the trips is highlighted and analysed in detail using the model. As Trip 17 is the most recent trip with the longest net length and a lot of data points, this is the trip that will be analysed in this chapter.

Trip 17 started at the first of September 2023 and ended at the 22^{nd} of September. In these three weeks, System 03 with a length of 2150 meters sailed around, catching plastics in the Great Pacific Garbage Patch. The location of the trip is presented in Figure 6.1.

Figure 6.1: Trip 17 location

Plastic extractions

During the trip, five extractions took place, meaning the retention zone was emptied on board five times. In these five extractions, a total of 45,848 kg of wet waste was removed from the ocean. This waste is categorised into three types: rigid plastics, fibrous plastics, and other waste. Of the total extracted wet weight, approximately 30% is rigid plastic, 58% is fibrous plastic (such as old fishing gear), and the remaining 12% is other waste. By dividing this total weight by the total run time, the extracted mass

per extraction run time is found to be 71.2 kilograms per hour. With an average speed through water of 0.74 m/s, ranging between 0.5 and 1.1 m/s, a total area of about 1500 square kilometres is swept, averaging 2 square kilometres per hour. In this area, the extracted mass per square kilometer of the swept area is 30 kilograms.

Key Performance Indicators

In Chapter 1, the Key Performance Indicators are introduced being: the costs per kilogram of extracted plastic and the carbon emissions per kilogram of extracted plastics. The Trip 17 data presents the following two results:

- Costs in euros per kilogram of extracted plastic: 103 €/kg
- Carbon emissions in tonnes per tonne of extracted plastic: 162 t/t

The mentioned costs include both operational expenses (OPEX) and capital expenditures (CAPEX). OPEX encompasses costs related to vessel charter, fuel, port fees, crew costs, and the operation of the coordination centre. CAPEX covers expenses such as the fabrication of the cleanup system, initial setup costs for the vessel, and the establishment of the coordination centre. Carbon emissions are estimated by multiplying the fuel consumption by a factor of 3.2, which represents the emissions in tons per ton of fuel consumed.

System span

During the three-week trip, environmental conditions varied, as detailed in Section 5.3. Consequently, it was sometimes inadvisable to operate, and the system had to be retracted for short periods. These retraction periods are not represented in the dataset. The dataset includes 1471 data points, providing information on vessel positions, current velocities, wave heights, system spans, and more, with each timestep's data used as input for the model. Figure 6.2 shows the effective span of the system during the three weeks, primarily operating at about 1300 meters. At certain points, the span briefly reduces to a very small value and then immediately increases again, indicating the periods when the system was retracted.

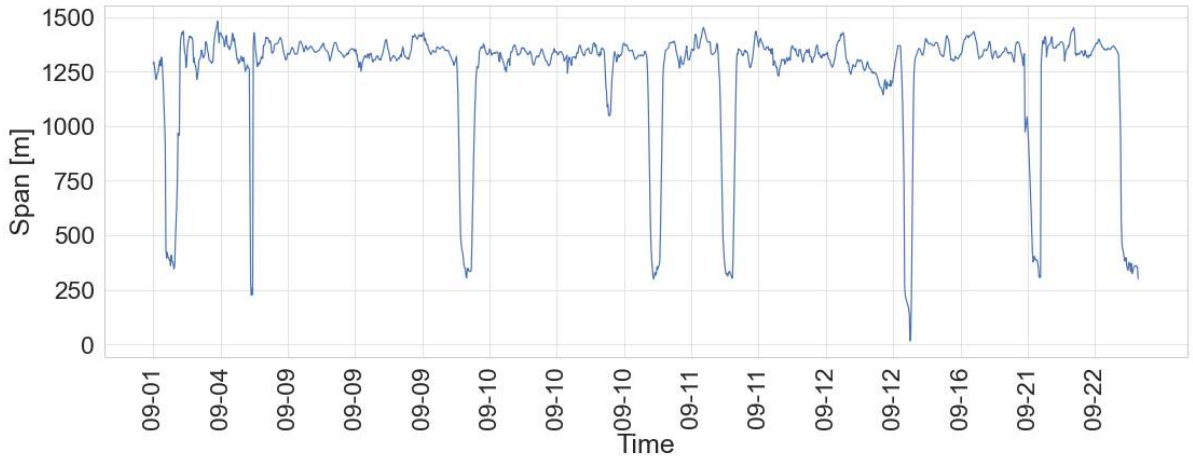

Figure 6.2: System span Trip 17

Input variables overview

Before running the model, some standard input variables are defined. These variables are dependent on the net, the towing cable properties and the preferences in the functionality of the model. The predefined input variables for Trip 17 are presented in Table 6.1.

Variable	Value
Net length	2150 m
Net depth	4 m
Net solidity	0.179
Net mesh size	16 mm
Net twine diameter	1.5 mm
Net material stiffness	120 GPa

Variable	Value
Towing cable length	600 m
Towing cable stiffness	184 GPa
Towing cable diameter	50.8 mm
Drag coefficients per angle of attack	deg: [5, 15, 45, 90] Cd: [0.33, 0.80, 1.44, 2.11]
Number of segments	15
Maximum number of iterations	100

Table 6.1: Input variables Trip 17

Running all of the 1471 cases results in a time trace showing the load on the winch at each individual time step. This time trace together with the measurement results and the 3D results are shown in Figure 6.3. In this plot, the blue line represents the measured load on the winch at one of the towing vessels in Trip 17. The orange line represents the regression line as explained in Section 4.1. Lastly, the green line represents the results generated by the 2D simplified model. Table 6.2 shows the information of Trip 17, regarding simulation times, Mean Absolute Errors and Mean Absolute Error as a percentage of the mean load for all data points combined, for only small span and for only wide span.

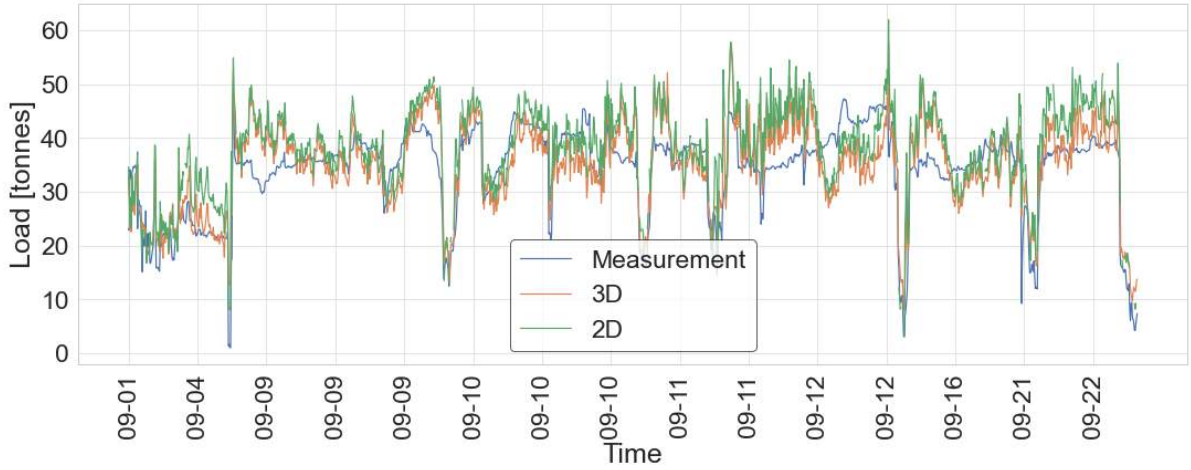

Figure 6.3: Time trace Trip 17

Trip 17			
# Segments	**# Cases**	**Sim.time per case [s]**	**Sim. time [s]**
15	1471	0.22	322

Total: load = 36.66 t	**3D**	**2D**
MAE [t]	5.47	5.70
Error [%]	15.1	15.7

Small: load = 18.61 t	**3D**	**2D**
MAE [t]	3.81	4.98
Error [%]	20.7	26.7

Wide: load = 37.74 t	**3D**	**2D**
MAE [t]	5.60	5.75
Error [%]	14.8	15.2

Table 6.2: Trip 17 results

The measured load signal can be used to identify the natural frequency of the system, which is the frequency at which the system tends to oscillate. By applying the Fourier transform, this natural frequency can be determined, as it is where the system exhibits resonance, leading to significantly higher loads. The Fourier transform on the 5-minute average measured loads on the winch results in the frequency spectrum as presented in Figure 6.4.

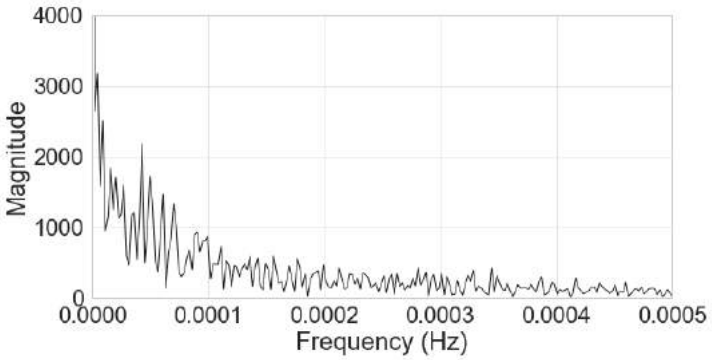

Figure 6.4: Frequency spectrum of the loads on System 03 during Trip 17

The frequency spectrum reveals higher energy at extremely low frequencies, specifically between 0 Hertz and 0.0001 Hertz. Given the system's large size and substantial inertia, it naturally resonates at these very low frequencies. However, these frequencies fall outside the wave regime, suggesting that the system will not resonate due to wave interaction. Other forces that could excite resonance in the system include wind and vessel course corrections. Nevertheless, none of these forces operate in the <0.0001 Hz range.

Going back to the time trace in Figure 6.3, a clear correlation can be observed between the predicted forces of the 3D model and the 2D model. At many points, there is also a good match between the models and the measured forces. However, there are some deviations between the predicted and measured forces. These deviations can be attributed to factors such as asymmetry, manoeuvring, or varying environmental conditions. To identify the sources of these errors, the next chapter will analyse these deviations in detail, aiming to determine their causes.

6.2. Analysis

As depicted in Figure 6.3, there is a clear matching trend between the 3D and 2D model. The 2D model tends to estimate slightly larger loads than the 3D model, resulting in a slightly larger mean absolute error (MAE) for this trip. When comparing both models to real-life measurements taken in the GPGP, the estimations align well with the measured loads. However, some discrepancies between the measurements and model estimations are noticeable. These differences can be complex and influenced by various external factors, making it difficult to pinpoint a single cause for the errors. This section examines the time range with the highest errors as an example. Figure 6.5 shows the absolute error between the measured loads and the loads estimated by the 2D model. The circle highlights the peak error, which will be analysed to identify possible causes.

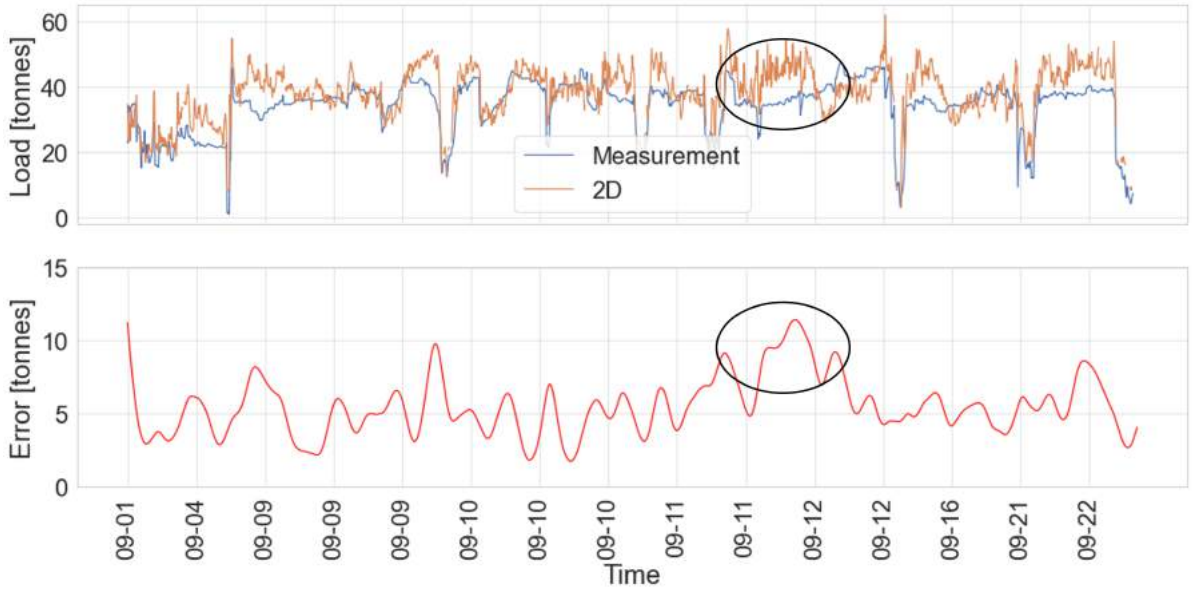

Figure 6.5: Estimated and measured loads on winch (top); Absolute error (bottom)

As many aspects could influence the loads on the system, an analysis is conducted to search for correlations between the error and other measured data from Trip 17. This should give insights into what aspects cause larger errors between the measured loads and the estimated loads using the 2D model. Examples of these aspects could be a sudden change in environmental conditions (wind direction, current speed, wave height) or human aspects like sudden manoeuvring of the vessels causing asymmetry, acceleration of the entire system or a change in system span. To keep the 2D model simple, not all aspects are taken into account, meaning that these aspects could result in errors.

Figure 6.6 zooms in on the period around the time points with the highest absolute error. After analysing all available signals and looking at small phase differences, the clearest correlation can be seen in the significant wave height in combination with the wind direction. Here an increase in wave height and a rotation of the wind correlates with an increased error.

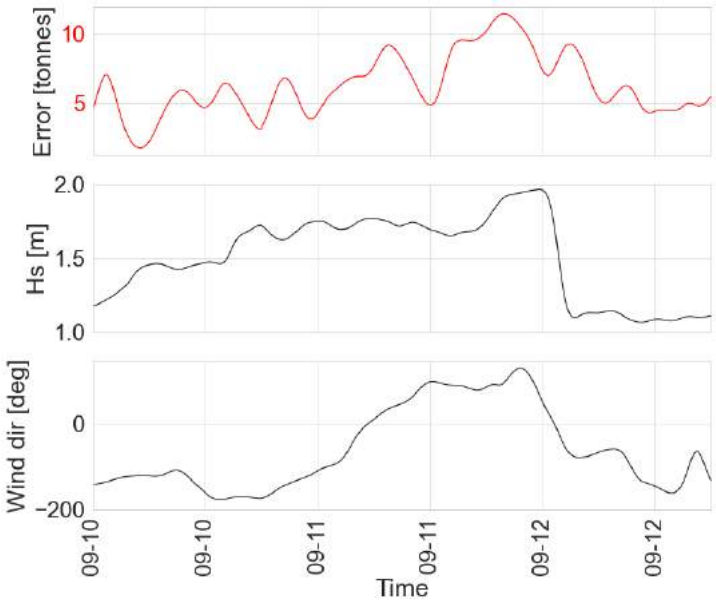

Figure 6.6: Error (top); Significant wave height (middle); Wind direction (bottom)

Not only do environmental conditions affect the loads exerted on the system, such as higher waves or wind speeds, but they could also influence the steering strategy. Constant on-board monitoring of the conditions determines the operational strategy and on-board decisions during the campaigns. For example, bad weather forecasts could convince the captain to increase velocity, change direction and decrease the system span. All of these factors can impact the forces acting on the system. Due to the objective of keeping the model simple, not all of these factors can be incorporated. Consequently, they may contribute to errors, making it challenging to pinpoint the exact origins of the errors.

6.3. Model Application

Now that the 2D simplified model has been validated with real-life data and proven to produce accurate results, it can be applied to the real-life operations of System 03. One useful application of the model is determining the maximum speed through water under specific environmental conditions.

For the system configuration of Trip 17, Figure 6.7 illustrates the maximum speed through water for varying wave heights and wave periods. In this analysis, the maximum load on one of the winch is set at 71.25 tonnes, and for the span, the typical 'wide span' is utilised, which is 0.6 times the system length.

Hs [m] \ Tp [s]	4	6	8	10	12	14	16
0	1.28	1.28	1.28	1.28	1.28	1.28	1.28
0.5	1.26	1.27	1.28	1.28	1.28	1.28	1.28
1	1.20	1.23	1.26	1.27	1.27	1.27	1.28
1.5	1.09	1.20	1.23	1.25	1.26	1.27	1.27
2	0.91	1.13	1.20	1.23	1.23	1.24	1.26
2.5	0.60	1.03	1.15	1.20	1.22	1.24	1.25
3	0	0.91	1.09	1.16	1.20	1.22	1.23
3.5	0	0.72	1.01	1.11	1.17	1.20	1.22
4		0.43	0.91	1.06	1.13	1.17	1.20
4.5		0	0.78	0.99	1.09	1.14	1.16
5		0	0.60	0.91	1.03	1.09	1.15

Max load [t]	71.25
span/length	0.6
length [m]	2150
span [m]	1290

Figure 6.7: HsTp table, illustrating maximum speed through water [m/s] in varying environmental conditions

In completely flat water, a maximum speed of 1.28 m/s can be achieved. As wave height increases, this maximum speed decreases accordingly. Additionally, the wave period plays a crucial role in the system's performance. Shorter wave periods amplify the impact on the system, further reducing the maximum achievable speed through the water. At a certain combination of wave height and wave period, the wave steepness exceeds the maximum wave steepness as presented in Equation 6.1 ([DNV], 2011). In this equation, S_{max} represents the maximum wave steepness, H_b the maximum wave height, and λ the wavelength, which can be determined using the wave period. The non-existent combinations of wave height and wave period in the lower left corner are marked in grey.

$$S_{max} = \frac{H_b}{\lambda} = \frac{1}{7} \tag{6.1}$$

As presented in Figure 5.13, the results may become inaccurate for velocities starting from 1.25 m/s. However, the model tends to overestimate the loads at higher velocities, making the values in the table conservative.

The presented table is valuable for offshore operations using the current system. Due to the flexibility of the 2D model, a similar table can easily be generated for a potential future system. As an example, a new system has been developed using the N1 net with a total length of 2500 meters. By adjusting the net parameters (solidity, length, drag coefficients), the same table can be generated for this potential future net, as shown in Figure 6.8.

Hs [m] \ Tp [s]	4	6	8	10	12	14	16
0	1.50	1.50	1.50	1.50	1.50	1.50	1.50
0.5	1.48	1.49	1.49	1.49	1.49	1.49	1.50
1	1.43	1.47	1.48	1.49	1.49	1.48	1.49
1.5	1.33	1.43	1.46	1.46	1.48	1.48	1.49
2	1.19	1.37	1.43	1.45	1.47	1.47	1.48
2.5	0.98	1.28	1.39	1.43	1.45	1.45	1.47
3	0.63	1.19	1.33	1.39	1.43	1.44	1.46
3.5	0	1.06	1.27	1.36	1.40	1.43	1.44
4		0.87	1.19	1.31	1.37	1.40	1.43
4.5		0.63	1.10	1.25	1.33	1.38	1.41
5		0	0.98	1.19	1.28	1.35	1.39

Max load [t]	71.25
span/length	0.6
length [m]	2500
span [m]	1500

Figure 6.8: HsTp table, illustrating maximum speed through water [m/s] for potential future net

The second table shows a higher maximum speed through water compared to the values in Figure 6.7. Despite the increased net length and span, the maximum speed through water surpasses that of the current system. This improvement is due to variations in solidity and drag coefficients at different angles of attack. On average, the speed through water increases by approximately 25%. With this increased speed and extended span using the new net, the total swept area reaches about 2180 square kilometers within the same time frame that Trip 17 covered 1500 square kilometers. Given that the extracted mass per square kilometer of swept area is 30 kilograms, the total wet weight of the extracted mass in this hypothetical scenario is about 65,400 kg. Assuming that costs do not increase significantly, since the loads on the system remain relatively constant, the estimated KPIs are as follows:

- Costs in euro per kilogram of extracted plastic: 73 €/kg
- Carbon emissions in tonnes per tonne of extracted plastic: 114 t/t

Using the 2D simplified model enables predictions about loads in specific scenarios and system limitations, such as determining the speed through water. Applied to the hypothetical case with certain assumptions, the results indicate an approximate 29% reduction in the cost per kilogram of extracted plastic and a similar 29% decrease in carbon emissions when using the hypothetical system configuration.

7

Discussion

This chapter aims to provide a comprehensive evaluation of various aspects of this research. It is divided into two sections. Firstly, the experiment discussion in Section 7.1 delves into the methodology of the experiment and seeks explanations for the observed results. Next, the developed model is discussed in Section 7.2. This section commences with an analysis of the input data, followed by an examination of the model's limitations, providing reasons for potential errors in the model.

7.1. Experiment Discussion

The experiment conducted at MARIN provided a comprehensive understanding of net behaviour in water and contributed to the accuracy of the 2D model. However, the following paragraphs present some reservations that can be made about the experiment.

Test matrix

In the experiment, a total of 27 tests were conducted, varying net types, net lengths, angles of attack, and velocities as presented in the test matrix. Despite the variation in test parameters, some information is missing, meaning that specific assumptions could not be verified. Examining the relationship between net length and drag force, as presented in Section 3.6, a linear trend line was drawn between the two measured data points. The figure is presented once more in Figure 7.1. The point where the lines of nets S03 and N1 intersect indicates the length at which the shielding effect becomes insignificant compared to the drag caused by the amount of material towed through the water. However, it's important to note that the relationship between net length and drag force is likely not linear. While the expectancy is that the trend is similar to that of the drag coefficient versus the angle of attack, the limited data, only two tested net lengths, means this relationship remains unknown. Introducing a third tested net length could alter the trend of the lines, and consequently, the point of intersection. Nevertheless, this point is expected to remain somewhere between two and six meters.

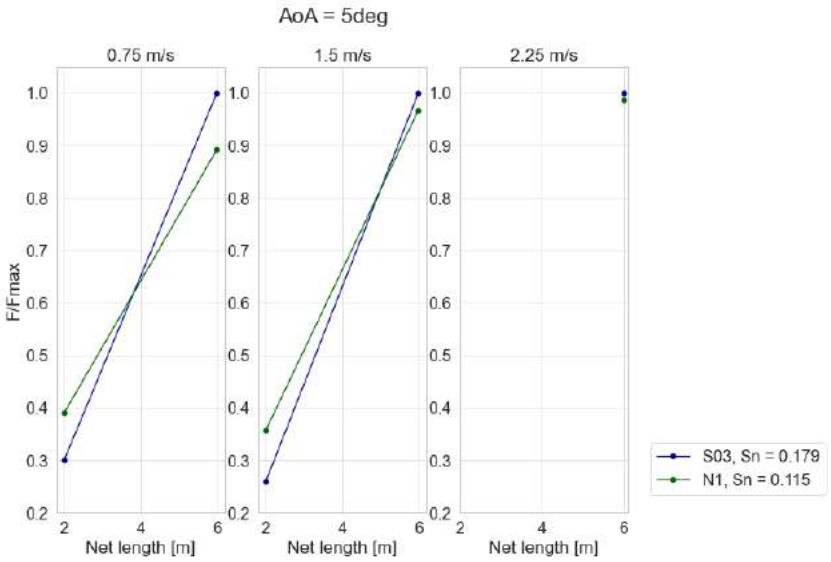

Figure 7.1: Experiment results for AoA = 5 degrees

Tests have been conducted on the net currently used by The Ocean Cleanup, as well as on net N1, which may be used in one of the future systems. However, since only two types of nets have been tested, the relationship between solidity and drag force remains unknown. Testing a third type of net, representing a different solidity, could confirm whether the point of intersection depicted in Figure 7.1 remains at the same net length, or whether it would change with a different solidity.

Finally, the smallest angle of attack presented in the test matrix is five degrees. For angles smaller than this, the frame disrupted the flow too much to obtain reliable results. Consequently, the drag coefficient for zero degrees is sourced from the literature. However, for wide-span cases, zero percent of the net is at an angle of attack smaller than five degrees. In contrast, for a span-to-length ratio of 0.2, about 50% of the net is at an angle of attack of less than 5 degrees, however, this is very rare.

Hydrodynamic drag

Hydrodynamic drag can be separated into form drag, viscous drag and wave drag. In the experiment, the measured drag is generated by towing a 2-meter deep net through the basin. From these measurements, the drag coefficients for varying angles of attack are calculated. However, because form drag and wave drag are dependent on water depth, there might be a difference in drag coefficients when the tests are repeated for a net that is not two, but four meters deep. The net of The Ocean Cleanup System 03 is 4 meters deep, however, what if future systems go even deeper than that? Can the drag coefficients of the experiment still be used or is the water depth playing a significant role in the drag?

Firstly, the viscous drag is assessed. Viscous drag is generated by the surface of the net moving through the fluid. The formula of viscous drag is stated in Equation 7.1:

$$R_s = \boldsymbol{f} S v^m \tag{7.1}$$

In this equation, the resistance R_s is determined by a frictional coefficient *f*, the wetted surface area S, the velocity v and an exponent m with a value of approximately 1.83 (Froude, 1877). Since the net is fully submerged, all variables in the equation are independent of water depth. Consequently, the viscous drag does not affect the drag coefficients when comparing nets with different depths, such as a two-meter and a four-meter deep net.

Secondly, the form drag is assessed. The form drag is influenced by the depth of immersion. As the depth increases, the hydrostatic pressure exerted by the weight of the water increases due to the force of gravity. Hydrostatic pressure is commonly measured in bars, with the pressure at sea level being 1 bar. For every 10 meters of depth, the pressure increases by an additional 1 bar. At greater depths,

the increased pressure may have a slight influence on the drag coefficient. However, since both the tested and operational nets are used at depths of only up to 4 meters, any increase in form drag would be negligible.

Thirdly, wave drag is assessed. As observed in the experiments, towing a net through the basin generates a wave behind it. This wave drag arises from the energy required to create surface waves as the net moves through the water. The net disturbs the water, displacing it and causing the formation of waves at the surface, which results in a resistance force opposing the net's motion. The Computational Fluid Dynamics (CFD) analysis conducted by L. Novais reveals that wave drag is highest just below the surface and decreases with increasing depth, stabilising at around 0.75 meters deep (Novais et al., 2012). R. Vennell's research supports this, showing that an object towed at the surface experiences up to 2.4 times more drag than when fully submerged. At a velocity of 1.7 m/s, wave drag is the dominant component, accounting for 50-60% of the total drag (Vennell et al., 2006). For a two-meter net, wave drag constitutes a significant portion of the total drag. However, for deeper nets, wave drag becomes less significant. Consequently, the effective drag coefficient of a four-meter net will be slightly lower than that of a two-meter net, potentially leading to a slight overestimation of the loads.

The investigation into three types of hydrodynamic drag yields the following conclusions: Firstly, viscous drag remains independent of depth, thus having no influence on the drag coefficient. Secondly, while form drag increases slightly with greater depths, this increase is insignificant for operational nets due to their shallow operating depths, up to 4 meters. Thirdly, wave drag decreases with depth. Near the surface, wave drag is highest, decreasing until approximately 0.75 meters depth. Because wave drag plays a larger role for the two-meter net than for the deeper four-meter net, the drag coefficient for the four-meter net will be slightly lower than for the two-meter net. Overall, the drag coefficients used from the experiment could lead to a slight overestimation of the loads.

Vortex Induced Vibrations

The experiment results show a clear acceleration phase, a constant velocity phase and a deceleration phase. As discussed in Chapter 3, a low-pass filter is applied to remove high-frequency fluctuations from the signal during the constant velocity phase. After filtering out these fluctuations generated by the frame moving through the water, a constant force remains that is used to determine the drag coefficients. However, the high-frequency fluctuations that have been filtered out in this case for the sake of model simplicity may be very significant in other situations. These 'vortex-induced vibrations' cannot be simply ignored in the construction of many structures. For example, vortex-induced vibrations play a crucial role in the development of structures like wind turbines.

7.2. Model Discussion

Although the developed 2D simplified model meets the, in the objective stated requirements, the following aspects should be taken into consideration.

7.2.1. Input Data

Sampling frequency

The developed model uses input data from the campaigns to simulate real-life scenarios and predict system loads. These predicted loads are then validated by comparing them with the measured loads on the winches aboard the two vessels. The measurement signals used include vessel positions, current speeds, sailing velocities, wave periods, and wave heights. The data is sampled every 5 minutes. Due to the system's high inertia, this 5-minute average data is sufficient for determining the model's shape while considering vessel positions. However, to gain better insight into the wave loads exerted on the system, a higher sampling frequency is necessary. With 5-minute average data, sudden high waves are averaged out, even though these waves could have the greatest impact on the system.

Load measurements

The second discussion point regarding the input data concerns the measurements conducted on the winches. The measurement of loads exerted on the winches aboard the vessels commenced in November 2022 during Trip 12, utilising Running Line Monitor devices (RLM). RLMs are sensors that measure

tension in the line. However, due to issues with the RLM on one of the vessels, this data was discarded from The Ocean Cleanup's analysis. As a result, the RLM data from the other vessel is consistently used as the reference for the entire system. Under 'normal' circumstances, when the system sails in a straight line without any environmental impact altering its shape, the loads are evenly distributed between the two winches. However, due to environmental impacts and the manoeuvring of the system, asymmetry can occur, resulting in unequal loads on the winches and rendering this reference inaccurate. Due to this asymmetry and the fact that only the loads on one side of the system are known, the total load on the system can only be estimated. Trip 17 marked the transition from using RLMs to conducting winch measurements, as these new measurement devices became available starting from this trip onwards. To ensure a comprehensive comparison between all trips (12 to 17), the data collected using the RLMs is utilised for all trips.

7.2.2. Model Limitations

Model simplifications

Before explaining step-by-step how the 2D model functions in Section 4.2, the model simplifications are outlined. These simplifications are necessary to achieve low simulation times without compromising the accuracy of the model. However, simplifications also introduce limitations to the model.

The first limitation is that one 2-dimensional line represents the entire drag of the net, including the net itself, the top floater, and the weighted bar at the bottom. However, the drag coefficients used in the model only account for the net itself, based on experimental results. To assess the influence of the top floater, The Ocean Cleanup conducted tests on the floater itself. The results of this experiment indicate that the ratio of the density of the floater to the density of the water is approximately 0.1, suggesting that the floater is only slightly submerged in the water. The drag generated by this small submerged volume is assumed to be negligible. Estimating the amount of drag generated by the weighted bar at the bottom is more challenging and this number is currently unknown. The presence of this floater and weighted bar could potentially increase the drag on the system, leading to an underestimation of the loads by the model. An assessment of the drag of the bottom line in OrcaFlex resulted in the conclusion that the drag on the weighted bar is negligible compared to the drag generated by the net.

Asymmetry

As mentioned earlier, the measured loads are only available for one side of the system. However, the model calculations provide a value that represents the drag on the entire system. To compare the measured load on one of the winches with the predicted load, the total load is divided by two. This assumes that the total load is evenly distributed over the two winches. However, due to environmental impacts or manoeuvres of the system, this may not be the case. These asymmetric results are also evident in the blue cloud of data points representing the measured loads of Trip 17, as shown in Figure 7.2.

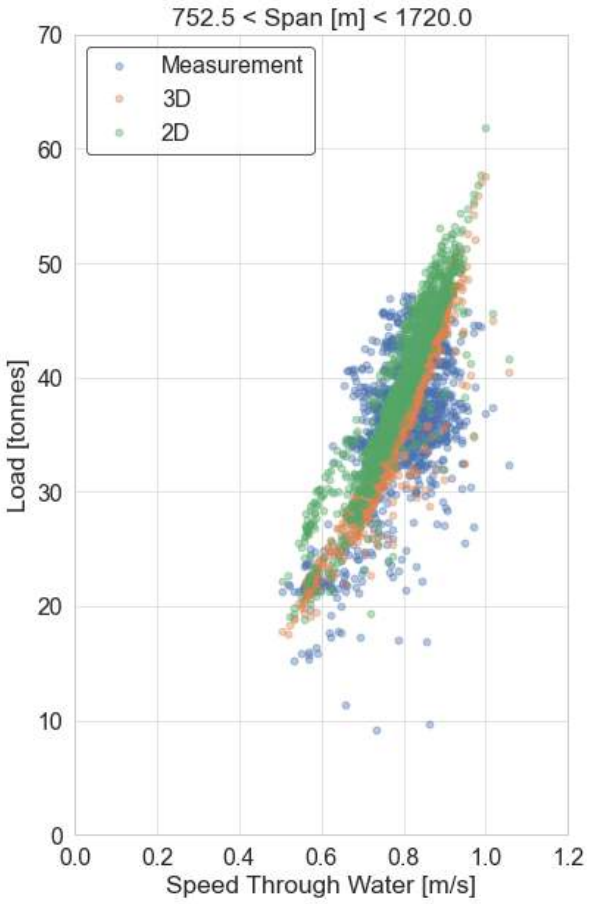

Figure 7.2: Trip 17 results, depicting asymmetric measured loads

This plot illustrates the wide-span results for Trip 17, comparing the measurements with both the 2D and the 3D models. The predicted loads by the 2D and 3D models exhibit a clear trend following the square of the speed through water (stw^2) from the drag equation. However, the measured data points are more widely distributed, forming a cloud instead of a line. This is because, in asymmetric cases, the load on one measured winch is higher compared to the other winch, while in other cases, it could be the opposite. Although the total load might follow the exact trend, this total measured load is not available. Therefore, the averaged predicted loads are compared to the measured loads on one of the winches.

Environmental conditions

Not only the asymmetry could be the cause of the distributed measured loads. Environmental conditions impacting the behaviour of the system could also generate results deviating from the expected trend. Wave-generated loads are a prime example of this. Waves are currently incorporated into the model as rotating particles, which slightly increase the speed through water. This is achieved by considering the significant wave height and the wave period. However, it's not just the wave height and period that are important for the load exerted on the system; the direction of the wave also plays a crucial role. Waves heading directly opposite to the system's sailing direction result in an increase in the load on the system upon impact. For waves aligned with the sailing direction, the opposite may occur. Waves impacting from the back of the system may cause a slight decrease in the tension measured at the winch. Additionally, waves hitting from the side may alter the shape of the system, generating loads that deviate from the expected trend. The wave direction is not taken into consideration in the 2D model, which may lead to over- or underestimation of the load.

Besides the wave direction not being included and the waves being a 5-minute average representation, also the wind is not taken into consideration in the development of the 2D model. To have enough

buoyancy to counter the weight of the net and the weighted bar, the volume of the floaters is high. Only a small part of the floater is submerged in the water, leaving a large volume above the water surface exposed to wind. The same as for waves, the drag generated by the wind can cause increases or decreases in the measured load and the shape of the system can be altered by side winds. Not taking the wind loads into account in the model may lead to over- or underestimation of the load.

Simulation time versus accuracy

Achieving complete accuracy and high speed simultaneously in a computer model is an impossible task. Since the goals of the 2D simplified model are to be both quick and accurate, a trade-off must be made between simulation time and accuracy. The results presented in this report are generated using a system containing a total of 15 segments. Increasing this number of segments leads to an exponential increase in simulation time, however, the accuracy increases as well. In the case the 2D model is to be used in offshore operations for swift decision-making, the number of segments could be reduced, resulting in slightly higher errors. However, in situations such as the development of a new system, where accurate results are crucial and simulation time is less of a concern, the number of segments could be increased, albeit at the cost of higher computational demand.

3D model validation

In this report, the accuracy of the developed 2D simplified model is compared to the accuracy of the 3D Finite Element model results. However, in contrast to the 2D model, the 3D model results are based on a regression analysis. Unlike the 2D model, which calculates results for each combination of input variables independently, the 3D model uses a regression analysis based on eight specific input combinations. These eight simulations support a regression line that predicts loads for different combinations of variables. As a result, the loads predicted by the regression model may vary from those obtained in a full simulation with the same inputs. Chapter 4 details the validation of this regression analysis, comparing its results against eight new simulation results. This comparison reveals an average absolute error of 4.4%, affirming the reliability of the regression line derived from the original simulations for predicting loads under various conditions. Despite the low error rate, a more precise comparison could involve matching the predicted loads from the 3D model directly with those from the 2D model. However, due to the extensive simulation times required by the 3D model, regression analysis offers a practical alternative for load prediction.

8

Conclusion

The main research question of this thesis is:

What is the physical behaviour of a high length-to-depth ratio net towed through water?

To address this question, experiments were conducted to gain a comprehensive understanding of the physical behaviour of a high length-to-depth ratio net towed through water. This understanding was then used to develop a model capable of accurately simulating the net's behaviour. The developed model was validated using real-life measurements and compared with an existing Finite Element model.

The overall conclusion is: the developed 2D simplified model is a simple, yet accurate model to simulate the physical behaviour of a high length-to-depth ratio net towed through water at operational speeds. Due to its simplicity and low simulation times, the model can be easily employed for offshore operations. It can assist in developing offshore steering strategies and determining environmental condition limits for the current system. A comprehensive understanding of the system's behaviour can significantly contribute to The Ocean Cleanup's progress toward its goal:

To reach 90% reduction of floating ocean plastic by 2040.

In order to get to this conclusion, six sub-questions are answered during the project. To answer the first two sub-questions about determining drag factors experimentally, several tests were conducted. In these experiments, two types of nets of varying lengths were towed through a basin at two different velocities and at various angles of attack. The measured loads on the nets were used to calculate the drag coefficients. The experimental drag coefficient of 2.11 for an angle of attack of 90 degrees is higher than the 1.71 reported in the literature. Additionally, the experimental drag coefficients at low angles of attack also turn out to be higher than those found in the literature.

The third sub-question concerns the influence of the angle of attack on the net panel. In line with theory, nets with higher solidity experienced higher loads at higher angles of attack. However, at low angles of attack, the opposite was observed: nets with higher solidity experienced lower loads, attributed to the shielding effect. The towing velocity determines the extent of this shielding effect. The drag reduction caused by the shielding effect is more pronounced for nets with higher solidity. At a certain point, increasing the net length does not enhance the shielding effect; instead, it increases drag due to the additional material towed through the water. Beyond the shielded area, higher solidity results in higher drag. For the nets tested, the shielding effect becomes insignificant for total drag within a specific net length range, typically between two and six meters. Beyond this range, the total drag is dominated by the drag generated by the net behind the shielded area. Given the investigation of high length-to-depth ratios and the observed limit falling between two and six meters, the drag coefficients calculated from the six-meter net were used for the model. This answers the fourth sub-question

The fifth sub-question pertains to the model predicting the behaviour of the system. To achieve this, the Newton-Raphson method is used to develop a 2D model for simulating the behaviour of a high length-to-depth ratio net towed through water. This method has proven to be both effective and efficient.

To ensure the accuracy and simplicity of the developed model, its outcomes are compared with measurement data, answering sub-question 6. The performance of the 2D model is then compared to the performance of the 3D Finite Element model by looking at the error between the predicted loads and the measured loads. Firstly, the Mean Absolute Error is expressed as a percentage of the mean load. When considering all time points from trips between September 2022 and September 2023, it is found that the 2D model performs equally well as the 3D model, with an error slightly above 20%. The time points were categorised into two groups: 'small span' (span/length < 0.6) and 'wide span' (span/length > 0.6). 'Wide span' configurations were the most common, resulting in an error of 18.7% for the 2D model and 20.1% for the 3D model.

It is concluded that 'small span' configurations present a subset of net behaviour that is much more difficult to capture both for the 2D and the 3D model. These configurations are typically employed in special cases such as high-velocity transport, extreme weather conditions, or quick manoeuvring. However, due to the infrequent occurrence of 'small span' configurations and the fact that the loads in these configurations do not approach the system's limits, they are less critical for the model's accuracy. Overall, both models perform accurately. The 2D model outperforms the 3D model at low velocities (< 0.5 m/s), while the 3D model is performing better at higher velocities (> 1.0 m/s).

The second aspect for comparing the models is the simulation time. Running a single scenario with the 3D Finite Element model in OrcaFlex takes about one week. In contrast, the 2D simplified model takes only 0.14 seconds on average for the same scenario. This represents a significant time saving compared to the 3D model, without compromising accuracy.

Thirdly, the flexibility of the models is assessed. For significant system updates, the 3D model requires approximately three weeks to obtain new results, making it inflexible and time-consuming to work with. In contrast, the 2D simplified model significantly improves efficiency. Adjusting system properties is straightforward by changing the model inputs, and running a complete set of, for example, 1400 data points takes just a few minutes. This quick calculation time makes the 2D model highly flexible and user-friendly.

The application of the validated 2D model developed in this thesis has confirmed that adjustments to the current system can enhance performance. By employing one test case, the overall efficiency of The Ocean Cleanup may be improved by changing the net type, increasing the net length, and increasing the sailing velocity. The adjustments in the system for this specific case resulted in an estimated emission saving and cost saving of about 30%. By conducting this case analysis, the model has proven not only to generate accurate results but also to be highly valuable for The Ocean Cleanup in the development of new systems and the formulation of new operation strategies.

9 Recommendations

The primary aim of conducting a research project is to acquire new knowledge and contribute to filling existing knowledge gaps. However, research often leads to the emergence of new questions and recommendations for further investigation. Below are points recommending a continuation of the current research, highlighting aspects that have not been addressed yet. Additionally, proposals for potential new research are presented.

9.1. Experiment Recommendations

- As mentioned in Chapter 7 a more extensive test matrix is recommended to get a comprehensive understanding of the net behaviour. Testing a third net length contributes to the understanding of the relation between the load on the net and the net length. Conducting these extra tests could avoid drawing a linear relation and might shift the point of intersection as presented in Figure 7.1.
- Following up on the previous recommendation, an extra solidity test could contribute to a better understanding as well. The result of the two tested nets can be implemented in the 2D simplified model, however, because only two different net solidities are tested it is unknown what the behaviour of a third net would be. A third net test could clarify the relation between net solidity and the shielding effect.
- In addition to expanding the test matrix of the experiment, similar results can be obtained through other methods. To better understand the net behaviour without incurring significant experimental costs, conducting a Computational Fluid Dynamics (CFD) analysis on the experimental results is recommended. Validating a CFD model with experimental results would enable the prediction of loads on nets of different lengths or solidities without the need for an entirely new experiment.
- A slight analysis of the observed high-frequency fluctuations during the tests has been conducted by creating a Power Spectral Density plot. However, these vortex-induced vibrations are very interesting in how structures react to incoming flow and play a significant role in the development of offshore structures. Due to resonance in these structures, vortex-induced vibrations could lead to critical loads in structures. In this research, these vibrations are filtered out, but extensive research on this phenomenon is possible.

9.2. Model Recommendations

- The simulation time of the model can be significantly reduced by using the shape from the previous case as the initial guess for the next iteration loop. Currently, the model begins each loop with the same initial guess and iterates until convergence is achieved. However, because there are typically only small changes in system shape between iterations, using the previous system shape for the new iteration loop would drastically decrease the number of iterations needed and with that, the simulation time.
- A more extensive analysis of the errors is recommended to increase the accuracy of the model. By investigating where the errors originate, the model can be fine-tuned to compensate for specific situations. For instance, if the analysis of errors reveals that the largest discrepancies occur when

the wave height exceeds a certain threshold, or when the water speed exceeds one meter per second, adjustments can be made to the model. Engineering factors can then be incorporated into the model to account for these specific cases.

- A more substantiated trade-off between accuracy and simulation time is recommended. This can be achieved by experimenting with the resolution or with the convergence threshold ϵ.
- As the goal of the model is to remain simple, some aspects have been deliberately excluded from the model. However, increased accuracy can be achieved by implementing aspects like wave direction, wind speed or wind direction. These environmental conditions influence the loads on the system but are not taken into account in the model potentially leading to errors. It should be noted that including more factors would make the model more complex, likely increasing the simulation time due to the need for more complex calculations.
- As discussed in Chapter 7, Trip 17 serves as a transition between two load-measuring methods. In this research, the model is validated by comparing the RLM data to the model output. It is recommended to also validate the model using the results from the new measurement method. It is expected that these new measurements are more accurate because the load measurements from both vessels can be combined and compared with the total predicted load. By comparing the total measured load with the total predicted load, the assumption that the load is equally distributed over the two vessels is avoided.
- Since the model has proven to generate accurate results, it can be effectively utilised in the form of a tool. The recommendation is to develop the model into a user-friendly tool that can be used on board the ships. A potential feature could include automatically determining routes based on satellite images that detect plastic hot spots.
- Further improvements of the model can be achieved by improved measurement data in future trips. Determining the most efficient type of net for capturing plastic involves assessing how much plastic slips through the net at a given solidity. By measuring the quantity of plastic that escapes past the system, one can identify which net type maximizes plastic capture. Another interesting aspect to measure is the depth of the weighted bar at the bottom of the net during operation. As the sailing speed increases, the system experiences higher loads and greater net tension. This tension can cause the net to deform, lifting the bottom bar and reducing its effective coverage area. This phenomenon is evident in Figure 5.12, where the data shows a distinct trend at speeds up to about 1.0 m/s, described by the equation STW^2. At higher speeds, the increased tensions cause a reduction in the net's projected area, moderating the rise in measured loads and shifting the growth pattern from exponential to more linear. Understanding the depth fluctuations of the net through measurements can help in refining models of its behaviour under different operational conditions.
- Despite the accuracy and quick simulation times of the 2D model, there are scenarios where the 3D Finite Element model remains advantageous. Using OrcaFlex, which incorporates dynamics along with the ability to simulate waves and wind, allows for a more detailed analysis of net behaviour in specific circumstances. Furthermore, the 3D capabilities are valuable for evaluating loads at different heights within the net. Therefore, it is advisable to use the OrcaFlex 3D model for detailed assessments in specific scenarios, while the 2D model is better suited for offshore decision-making and rapid calculations.
- The reality in the offshore industry is that a gap exists between the crew onboard vessels and the office staff. In the office developed tools are often disregarded as soon as offshore operations yield different results. It is recommended to compare the model with real-time measurements to facilitate its implementation onboard the vessels. It is essential to demonstrate that the model operates with consistent accuracy, and there must be a provision for feedback.

References

Balash, C., Colbourne, B., Bose, N., & Raman-Nair, W. (2009). Aquaculture net drag force and added mass. *Aquacultural Engineering*, *41*, 14–21. https://doi.org/10.1016/j.aquaeng.2009.04.003

Balash, C., & Sterling, D. J. (2012). Prawn trawl drag due to material properties - an investigation of the potential for drag reduction. *Proceedings of the 2nd International Symposium on Fishing Vessel Energy Efficiency E-fishing*, 1–9. http://ecite.utas.edu.au/79064/

Blocken, B. B., Van Druenen, T., Toparlar, Y., Malizia, F., Mannion, P., Andrianne, T., Marchal, T., Maas, G.-J., & Diepens, J. (2018). Aerodynamic drag in cycling pelotons: New insights by CFD simulation and wind tunnel testing. *Journal of wind engineering and industrial aerodynamics*, *179*, 319–337. https://doi.org/10.1016/j.jweia.2018.06.011

Bouhoubeiny, E., Druault, P., & Germain, G. (2014). Phase-averaged mean properties of turbulent flow developing around a fluttering sheet of net. *Ocean Engineering*, *82*, 160–168. https://doi.org/10.1016/j.oceaneng.2014.03.009

Broadhurst, M. K., Millar, R. B., Kennelly, S. J., Macbeth, W. G., Young, D. J., & Gray, C. A. (2004). Selectivity of conventional diamond- and novel square-mesh codends in an Australian estuarine Penaeid-trawl fishery. *Fisheries Research*, *67*(2), 183–194. https://doi.org/10.1016/j.fishres.2003.09.043

Carter, C. (2002). Great Circle Distances: Computing the distance between two points on the surface of the Earth. *SiRF White Paper*.

Castellano, S., Mugnozza, G. S., Russo, G. F., Briassoulis, D., Mistriotis, A., Hemming, S., & Waaijenberg, D. (2008). Plastic Nets in agriculture: A General Review of Types and Applications. *Applied Engineering in Agriculture*, *24*(6), 799–808. https://doi.org/10.13031/2013.25368

Cheng, H., Li, L., Aarsæther, K. G., & Ong, M. C. (2020). Typical hydrodynamic models for aquaculture nets: A comparative study under pure current conditions. *Aquacultural Engineering*, *90*. https://doi.org/10.1016/j.aquaeng.2020.102070

Colless, B. (2019, June). My Top 5 Pet Peeves with Time Trial Bikes. https://nozawaphysio.com/blog/my-top-5-pet-peeves-with-time-trial-bikes/

[DNV], D. N. V. (2011, April). *DNV-RP-H103: Modelling and Analysis of Marine Operations* (tech. rep.). https://home.hvl.no/ansatte/gste/ftp/MarinLab_files/Litteratur/DNV/rp-h103_2011-04.pdf

[DNV], D. N. V. (2014, April). *DNV-RP-C205: Environmental Conditions and Environmental Loads* (tech. rep.). https://www.docenti.unina.it/webdocenti-be/allegati/materiale-didattico/584574

Eriksen, M., Cowger, W., Erdle, L. M., Coffin, S., Villarrubia-Gómez, P., Moore, C. J., Carpenter, E., Day, R. H., Thiel, M., & Wilcox, C. (2023). A growing plastic smog, now estimated to be over 170 trillion plastic particles afloat in the world's oceans—Urgent solutions required. *PloS one*, *18*(3), e0281596. https://doi.org/10.1371/journal.pone.0281596

Fredheim, A. (2005). *Current forces on net structure* (Publication No. 2005:64) [Doctoral thesis]. Norwegian University of Science and Technology. https://brage.bibsys.no/xmlui/handle/11250/231260

Froude, W. (1877). Wave-Making Resistance of Ships. *Scientific American*, *3*(74supp), 1167–1169. https://doi.org/10.1038/scientificamerican06021877-1167bsupp

Gad el Hak, M. (1987). The water towing tank as an experimental facility. *Experiments in Fluids*, *5*(5), 289–297. https://doi.org/10.1007/bf00277707

Hao, Z., Sun, C., Lu, Y., Bi, K., & Zhou, T. (2022). Suppression of Vortex-Induced Vibration and Phase-Averaged Analysis of the Wake Generated by a Circular Cylinder Covered with Helical Grooves. *Fluids*, *7*(6), 194. https://doi.org/10.3390/fluids7060194

Hodson, T. O. (2022). Root-Mean-square Error (RMSE) or Mean Absolute Error (MAE): when to use them or not. *Geoscientific Model Development*, *15*(14), 5481–5487. https://doi.org/10.5194/gmd-15-5481-2022

Holthuijsen, L. H. (2007, February). *Waves in Oceanic and Coastal Waters*. Cambridge University Press.

Ivanco, T. G. (2009, July). Development and Validation of an Aeroelastic Ground Wind Loads Analysis Tool for Launch Vehicles. https://vtechworks.lib.vt.edu/handle/10919/34462

Jentzsch, M. P., Schmidt, H.-J., Woszidlo, R., Nayeri, C. N., & Paschereit, C. O. (2021). Challenges and procedures for experiments with steady and unsteady model velocities in a water towing tank. *Experiments in Fluids*, *62*(4). https://doi.org/10.1007/s00348-021-03151-5

Jiménez, M., Rakotonirina, A. D., Sainte-Rose, B., & Cox, D. J. (2023). On the Digital Twin of the Ocean Cleanup Systems—Part I: Calibration of the Drag Coefficients of a Netted Screen in OrcaFlex Using CFD and Full-Scale Experiments. *Journal of Marine Science and Engineering*, *11*(10), 1943. https://doi.org/10.3390/jmse11101943

Jonsson, P. R., Van Duren, L. A., Amielh, M., Asmus, R., Aspden, R. J., Daunys, D., Friedrichs, M., Friend, P. L., Olivier, F., Pope, N., Precht, E., Sauriau, P.-G., & Schaaff, E. (2006). Making Water Flow: A comparison of the hydrodynamic characteristics of 12 different benthic biological flumes. *Aquatic Ecology*, *40*(4), 409–438. https://doi.org/10.1007/s10452-006-9049-z

Khair, U., Fahmi, H., Hakim, S. A., & Rahim, R. (2017). Forecasting error calculation with mean absolute deviation and mean absolute percentage error. *Journal of physics*, *930*, 012002. https://doi.org/10.1088/1742-6596/930/1/012002

Kristiansen, D., Lader, P., Jensen, Ø., & Fredriksson, D. (2015). Experimental study of an aquaculture net cage in waves and current. *China Ocean Engineering*, *29*, 325–340. https://doi.org/10.1007/s13344-015-0023-1

Kumazawa, T., Hu, F., Kinoshita, H., & Tokai, T. (2012). Hydrodynamic characteristics of plane Minnow netting made of high-strength polyethylene (Dyneema). *Nippon Suisan Gakkaishi*, *78*(2), 180–188. https://doi.org/10.2331/suisan.78.180

Løland, G. (1993). Current forces on, and water flow through and around, floating fish farms. *Aquaculture International*, *1*(1), 72–89. https://doi.org/10.1007/bf00692665

Madsen, N., Hansen, K., & Enerhaug, B. (2011). Experimental Analysis of the Hydrodynamic Coefficients of the Net Panels in the Flume Tank in Hirtshals. *Contributions on the Theory of Fishing Gears and Related Marine Systems*, *7*, 131–140.

Miettinen, A., Sarmaja Korjonen, K., Sonninen, E., Junger, H., Lempiäinen, T., Ylikoski, K., Mäkiaho, J.-P., Carpelan, C., & Jungner, H. (2008). The palaeoenvironment of the 'Antrea Net Find'. *Karelian Isthmus – Stone Age Studies in 1998–2003*, *16*, 71–87. https://researchportal.helsinki.fi/en/publications/the-palaeoenvironment-of-the-antrea-net-find

Moret, K., & Legge, G. (2014). Flume tank. *The Journal of Ocean Technology*, *9*(Special Issue), 92–93. https://brage.bibsys.no/xmlui/handle/11250/231260

Morison, J., Johnson, J., & Schaaf, S. (1950). The Force Exerted by Surface Waves on Piles. *Journal of Petroleum Technology*, *2*(05), 149–154. https://doi.org/10.2118/950149-G

Naumov, A. V., Velikanov, N., & Kikot, A. (2013). The hydrodynamic drag coefficient of flat netting at a cross-section flow. *Mathematical modeling of pumps in the network View project Theoretical Simulation of Fish Cutting Process View project*. https://www.researchgate.net/publication/279957685_The_hydrodynamic_drag_coefficient_of_flat_netting_at_a_cross-section_flow

Niño, Y., Vidal, K., Tamburrino, A., Zamorano, L. R. M., Beltrán, J. F., Estay, G., & Muñoz, A. D. (2020). Normal and tangential drag forces of nylon nets, clean and with fouling, in fish farming. an experimental study. *Water*, *12*(8), 2238. https://doi.org/10.3390/w12082238

Novais, M., Silva, A., Mantha, V., Ramos, R., Rouboa, A., Vilas-Boas, J. P., Luís, S., & Marinho, D. A. (2012). The Effect of Depth on Drag During the Streamlined Glide: A Three-Dimensional CFD Analysis. *Journal of Human Kinetics*, *33*(2012), 55–62. https://doi.org/10.2478/v10078-012-0044-2

OECD. (2022). Global plastics outlook: Economic drivers, environmental impacts and policiy options. https://doi.org/https://doi.org/10.1787/de747aef-en

Patursson, Ø., Swift, M., Tsukrov, I., Simonsen, K., Baldwin, K. C., Fredriksson, D. W., & Çelıkkol, B. (2010). Development of a porous media model with application to flow through and around a net panel. *Ocean Engineering*, *37*(2-3), 314–324. https://doi.org/10.1016/j.oceaneng.2009.10.001

Pham, Y. (2023, October). Interview with Yannick Pham, Steering Strategy Manager at The Ocean Cleanup.

Philippe-Janon, M. (2023, October). Interview with Marceau Philippe-Janon, Hydrodynamics team at The Ocean Cleanup.

Ramzi, N. A. S., Quen, L. K., Senga, H., Kang, H.-S., Lim, M. H., & Sukarnoor, N. I. M. (2022). Suppression of vortex-induced vibration of a rigid cylinder using flexible shrouding. *Applied ocean research*, *123*, 103154. https://doi.org/10.1016/j.apor.2022.103154

Rapp, B. E. (2017). *Microfluidics: Modelling, mechanics and mathematics* [https://doi.org/10.1016/C2012-0-02230-2]. Elsevier.

Reynolds, O. (1883). An experimental investigation of the circumstances which determine whether the motion of water shall be direct of sinuous, and of the law of resistance in parallel channels [https://doi.org/10.1098/rstl.1883.0029]. *Philosophical transactions of the Royal Society of London*, *174*, 935–982.

Ritchie, H. (2023, October). How much plastic waste ends up in the ocean? https://ourworldindata.org/how-much-plastic-waste-ends-up-in-the-ocean#article-citation

Sanborn, B., DiLeonardi, A. M., & Weerasooriya, T. (2014). Tensile properties of dyneema SK76 single fibers at multiple loading rates using a direct gripping method. *Journal of Dynamic Behavior of Materials*, *1*(1), 4–14. https://doi.org/10.1007/s40870-014-0001-3

Shevtsov, S. (1988). Selective properties of trawl cod-ends with various mesh shapes for baltic herring fishery. https://www.researchgate.net/publication/279957685

Shimizu, H., Mizukami, Y., & Kitazawa, D. (2018). Experimental study of the drag on fine-mesh netting. *Aquacultural Engineering*, *81*, 101–106. https://doi.org/10.1016/j.aquaeng.2018.03.005

Slat, B. (2014). *How the oceans can clean themselves: A feasibility study*. Ocean Cleanup. https://books.google.nl/books?id=8OgTrgEACAAJ

Slat, B. (2012, October). How the oceans can clean Themselves: Boyan Slat at TEDxDelft. https://www.youtube.com/watch?v=ROW9F-c0kIQ

Stewart, P. A., & Ferro, R. (1985). Measurements on Gill nets in a flume tank. *Fisheries Research*, *3*, 29–46. https://doi.org/10.1016/0165-7836(85)90006-2

Swift, M. R., Fredriksson, D. W., Unrein, A., Fullerton, B., Patursson, O., & Baldwin, K. (2006). Drag force acting on biofouled net panels. *Aquacultural Engineering*, *35*, 292–299. https://doi.org/10.1016/j.aquaeng.2006.03.002

Tang, H., Hu, F., Xu, L., Dong, S., Zhou, C., & Wang, X. (2017). The effect of netting solidity ratio and inclined angle on the hydrodynamic characteristics of knotless polyethylene netting. *Journal of Ocean University of China*, *16*, 814–822. https://doi.org/10.1007/s11802-017-3227-6

Tang, H., Xu, L., & Hu, F. (2018). Hydrodynamic characteristics of knotted and knotless purse seine netting panels as determined in a flume tank. *PLoS ONE*, *13*. https://doi.org/10.1371/journal.pone.0192206

The Ocean Cleanup. (n.d.). The ocean cleanup [Accessed: 2024-05-17]. https://theoceancleanup.com/our-mission/

Thierry, N. N. B., Tang, H., Achile, N. P., Xu, L., Hu, F., & You, X. (2020). Comparative study on the full-scale prediction performance of four trawl nets used in the coastal bottom trawl fishery by Flume Tank Experimental Investigation. *Applied Ocean Research*, *95*, 102022. https://doi.org/10.1016/j.apor.2019.102022

Tsukrov, I., Drach, A., Decew, J., Swift, M. R., & Celikkol, B. (2011). Characterization of geometry and normal drag coefficients of copper nets. *Ocean Engineering*, *38*, 1979–1988. https://doi.org/10.1016/j.oceaneng.2011.09.019

Van Sebille, E., Wilcox, C., Lebreton, L., Maximenko, N., Hardesty, B. D., Van Franeker, J., Eriksen, M., Siegel, D. A., Galgani, F., & Law, K. L. (2015). A global inventory of small floating plastic debris. *Environmental Research Letters*, *10*(12), 124006. https://doi.org/10.1088/1748-9326/10/12/124006

Vennell, R., Pease, D., & Wilson, B. (2006). Wave drag on human swimmers. *Journal of biomechanics*, *39*(4), 664–671. https://doi.org/10.1016/j.jbiomech.2005.01.023

Wu, W., & Cao, X. (2016). Mechanics model and its equation of wire rope based on elastic thin rod theory. *International Journal of Solids and Structures*, *102-103*, 21–29. https://doi.org/10.1016/j.ijsolstr.2016.10.021

Zdravkovich, M. M. (1992). Aerodynamics of bicycle wheel and frame. *Journal of Wind Engineering and Industrial Aerodynamics*, *40*(1), 55–70. https://doi.org/10.1016/0167-6105(92)90520-k

Zhan, J. M., Jia, X. P., Li, Y. S., Sun, M. G., Guo, G. X., & Hu, Y. Z. (2006). Analytical and experimental investigation of drag on nets of fish cages. *Aquacultural Engineering*, *35*, 91–101. https://doi.org/10.1016/j.aquaeng.2005.08.013

Zhou, C., Xu, L., Hu, F., & Qu, X. (2015). Hydrodynamic characteristics of knotless nylon netting normal to free stream and effect of inclination. *Ocean Engineering*, *110*, 89–97. https://doi.org/10.1016/j.oceaneng.2015.09.043

Zou, B., Thierry, N. N. B., Tang, H., Xu, L., Dong, S., & Hu, F. (2022). The deformation characteristics and flow field around knotless polyethylene netting based on fluid structure interaction (FSI) one-way coupling. *Aquaculture and Fisheries*, *7*(1), 89–102. https://doi.org/10.1016/j.aaf.2020.07.012

A

GPGP measurements

This appendix presents the measurement data obtained from the GPGP. The signals recorded per trip serve as both inputs and validation data for the model. The inputs for the model include system length, vessel separation, effective span, speed over ground, current, speed through water, significant wave height and wave period. The measured loads are used for validation.

System length During the timeperiod, the system was in transition to System 03. In this transition, modules of floaters and nets are connected to the original system. In this dataset, the system length starts at 783 meters in trip 12 and ends at 2150 meters in trip 17.

Vessel separation By comparing the location of the towing vessels, the vessel separation is determined. This vessel separation determines the effective span of the system. The vessel separation is used as an input for the model.

Effective span The effective span represents the distance between the front two modules on both sides of the system. A large effective span is used in high-density plastic areas to gather the most plastics. A larger effective span results in higher forces on the system.

Speed Over Ground GPS data is used to determine the speed of both vessels over ground, the absolute speed. Both direction and magnitude are presented in the dataset.

Current Current direction and current magnitude are measured and presented in the dataset.

Speed Through Water The Speed Through Water is a combination of the Speed Over Ground and the current and represents the relative speed of the vessel. The STW direction and magnitude are used as an input for the model.

Load Tender Load Tender represents the load on one of the two vessels. A sensor measures the force exerted by the system on the winch. This signal will be used to validate the load calculations.

Significant wave height The significant wave height is an average measurement of the largest one-third of the waves. The signal is used as input for the model and in the calculation of the total drag

Peak wave period The peak wave period is the time it takes for the peak to complete one full oscillation. Such as the significant wave height, the peak wave period is used as input for the model and in the calculation of the total drag.

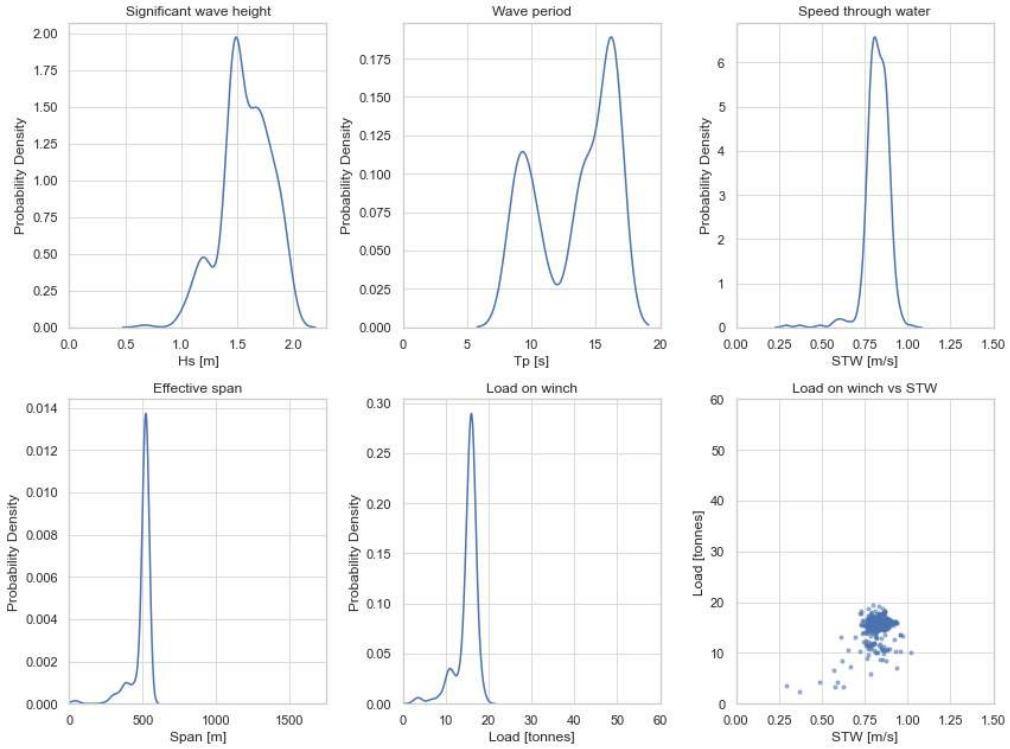

Figure A.1: Trip 12 GPGP measurements

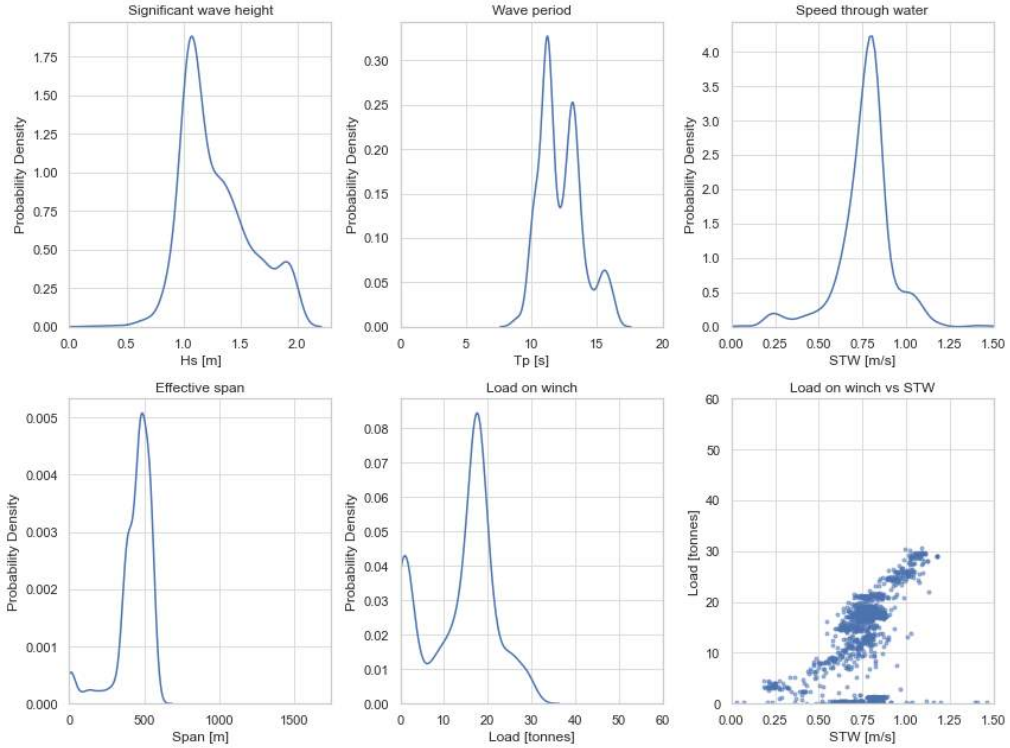

Figure A.2: Trip 13 GPGP measurements

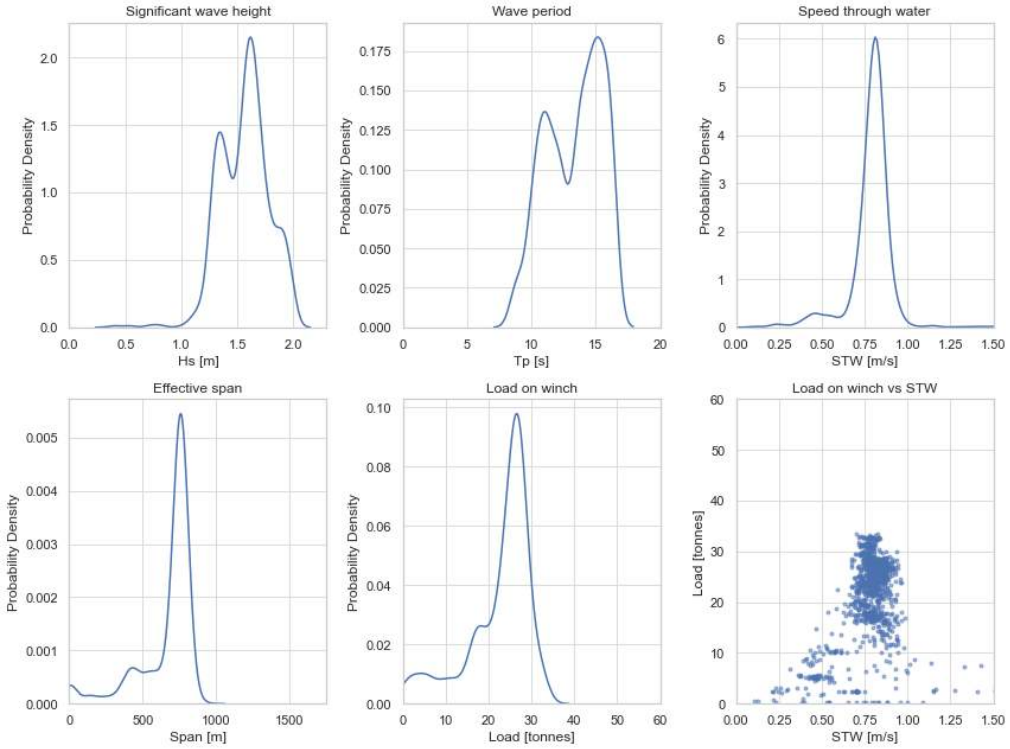

Figure A.3: Trip 14 GPGP measurements

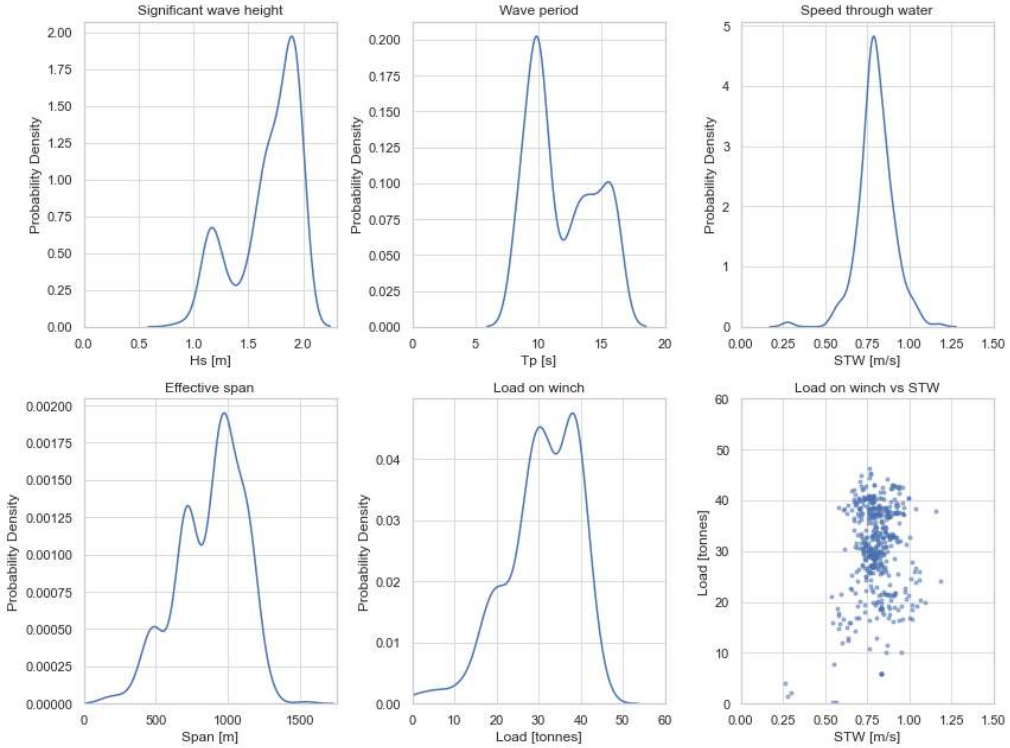

Figure A.4: Trip 15 GPGP measurements

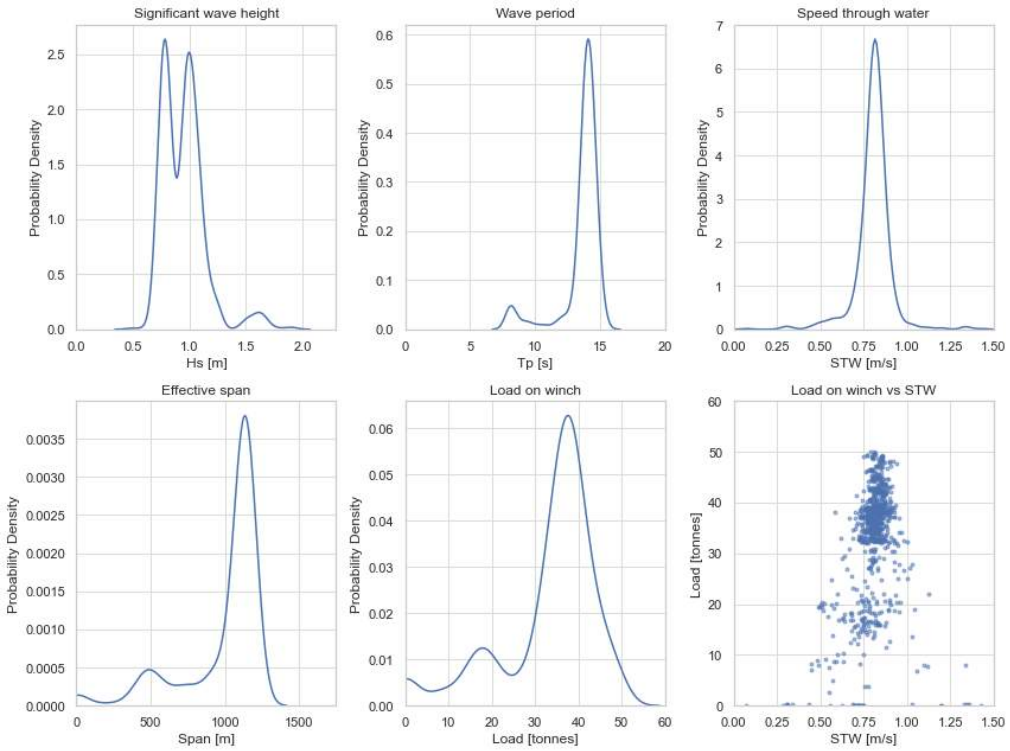

Figure A.5: Trip 16_S2c GPGP measurements

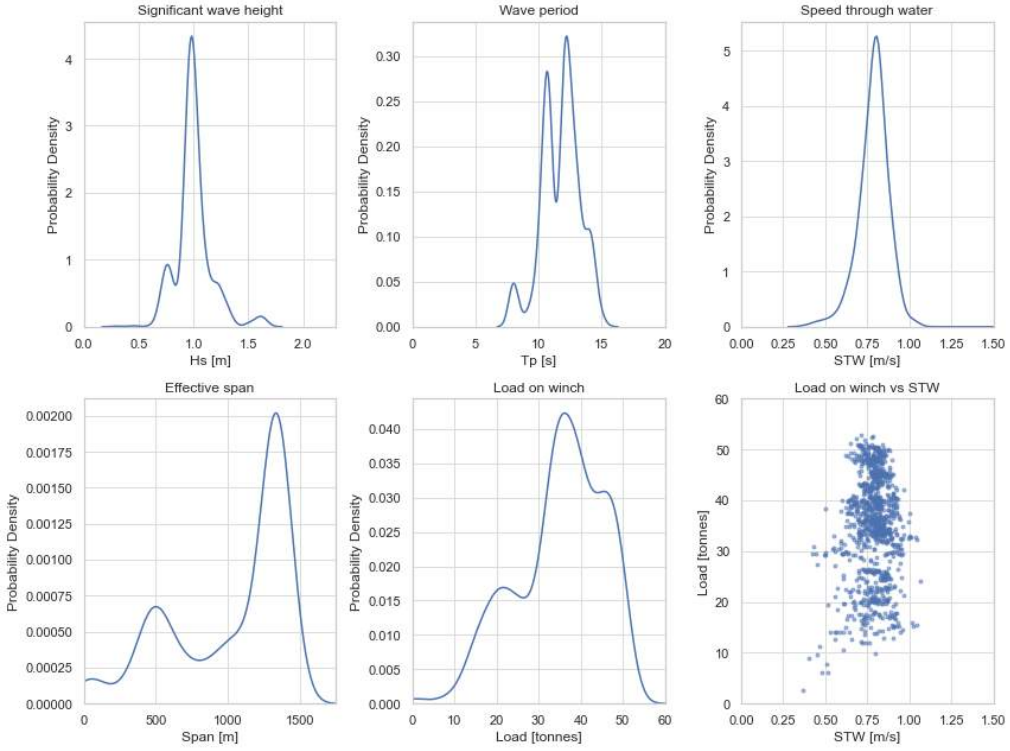

Figure A.6: Trip 16_S3 GPGP measurements

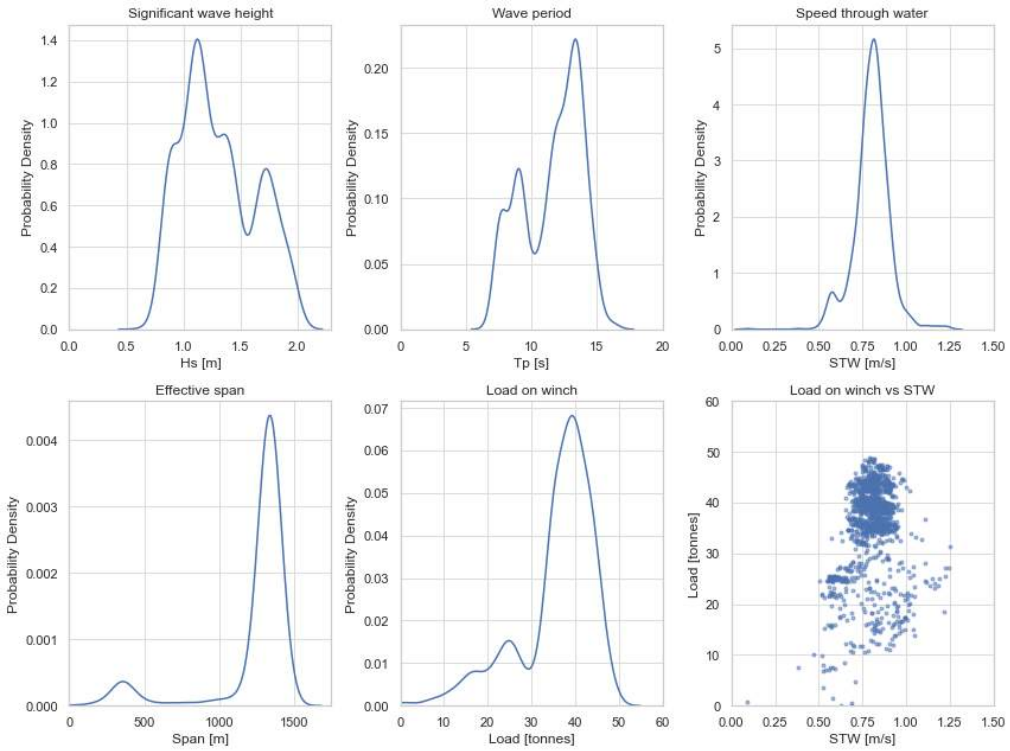

Figure A.7: Trip 17 GPGP measurements

B

Model results

This appendix presents per trip the results of the 2D- and 3D-model compared to the measurements. The graphs show: probability density function of the loads, probability density function of the measured span, the measured and predicted loads for small span and the measured and predicted loads for wide span.

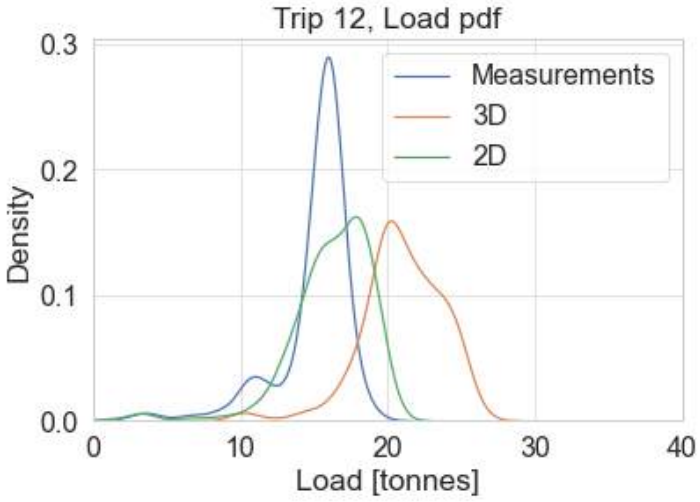

Figure B.1: Load PDF, Trip 12

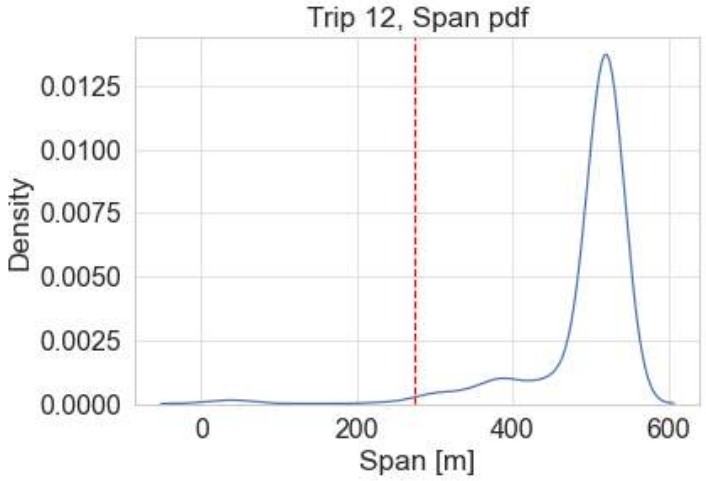

Figure B.2: Span PDF, Trip 12

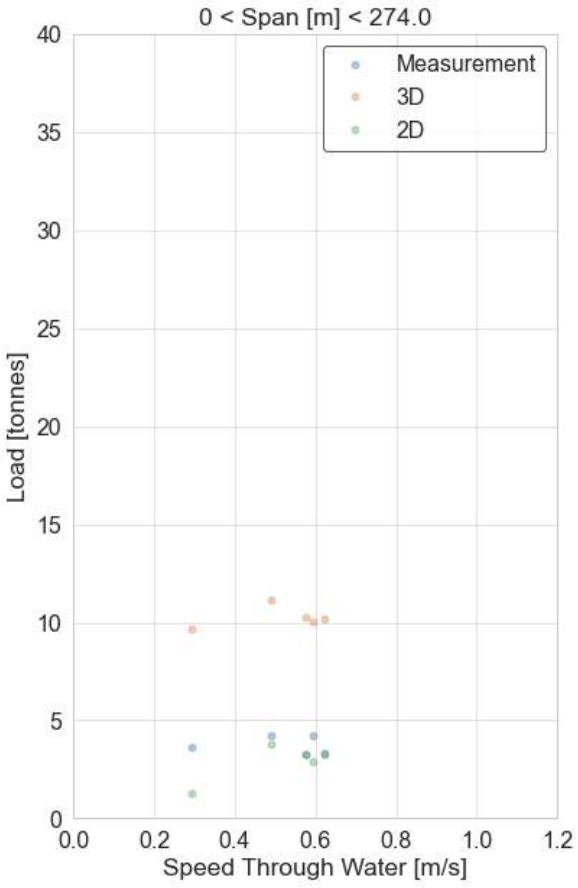

Figure B.3: Trip 12, small span results

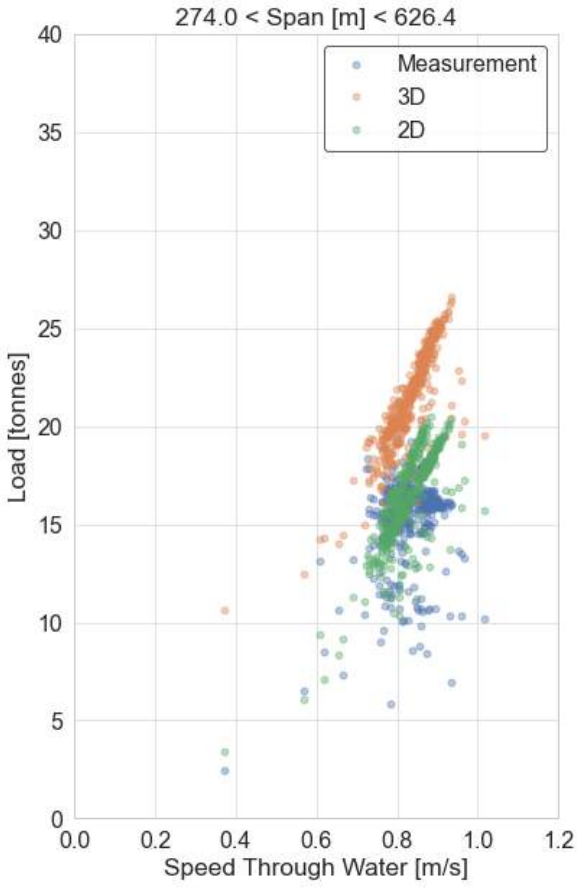

Figure B.4: Trip 12, wide span results

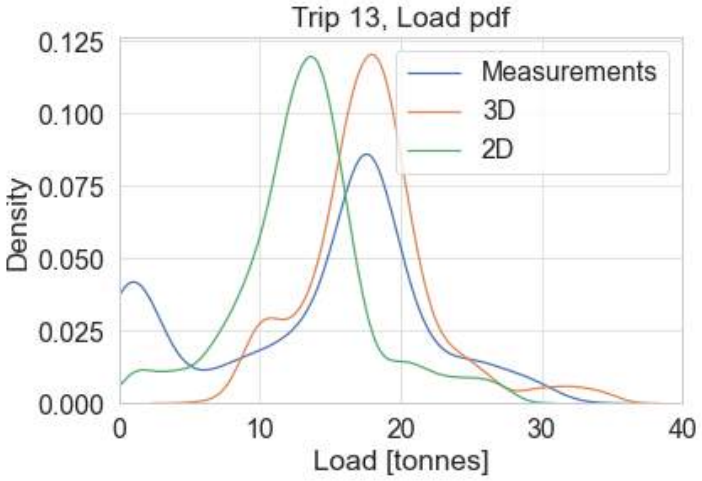

Figure B.5: Load PDF, Trip 13

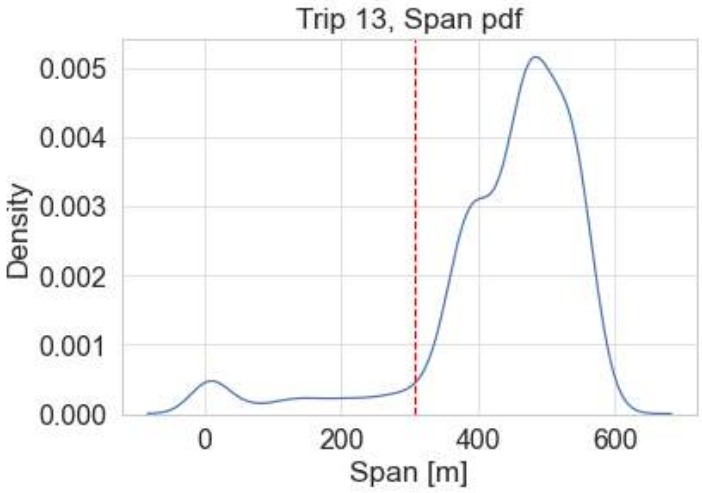

Figure B.6: Span PDF, Trip 13

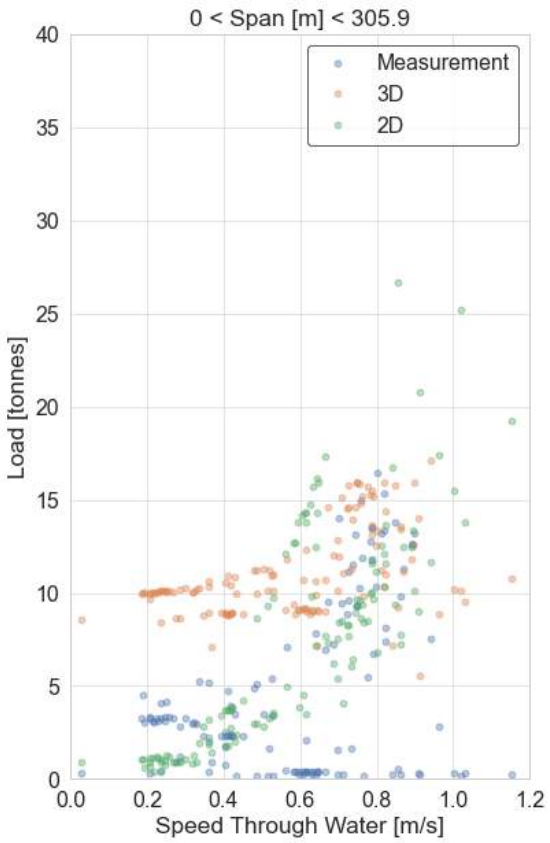

Figure B.7: Trip 13, small span results

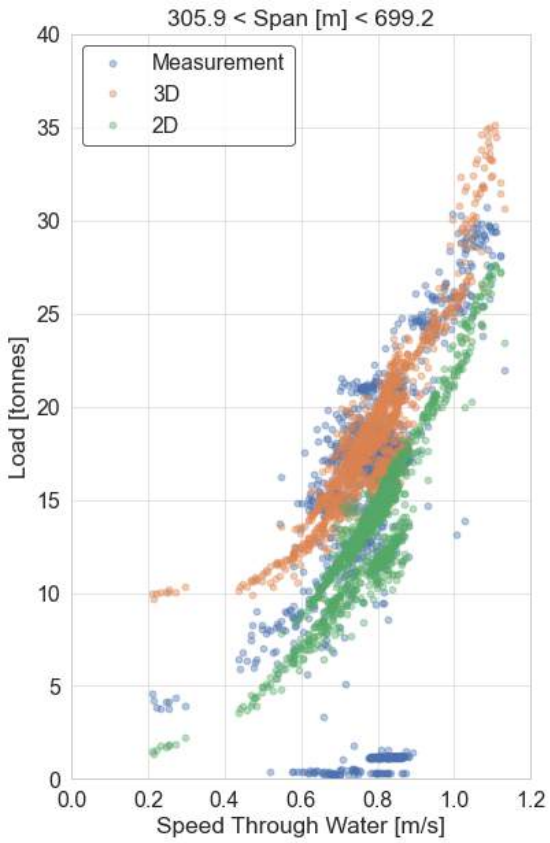

Figure B.8: Trip 13, wide span results

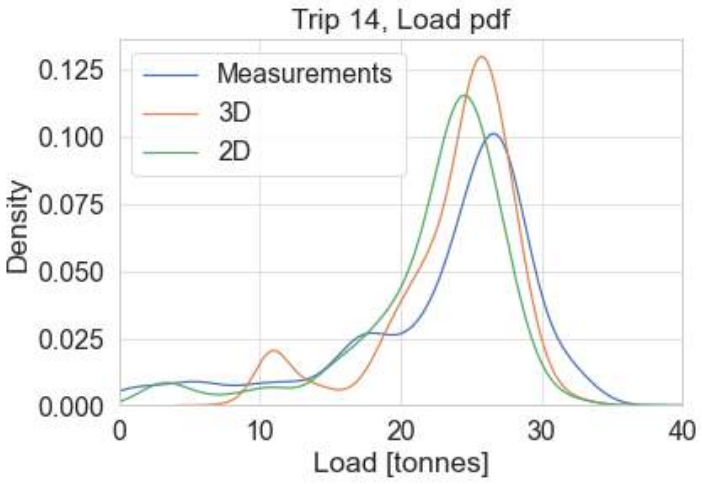

Figure B.9: Load PDF, Trip 14

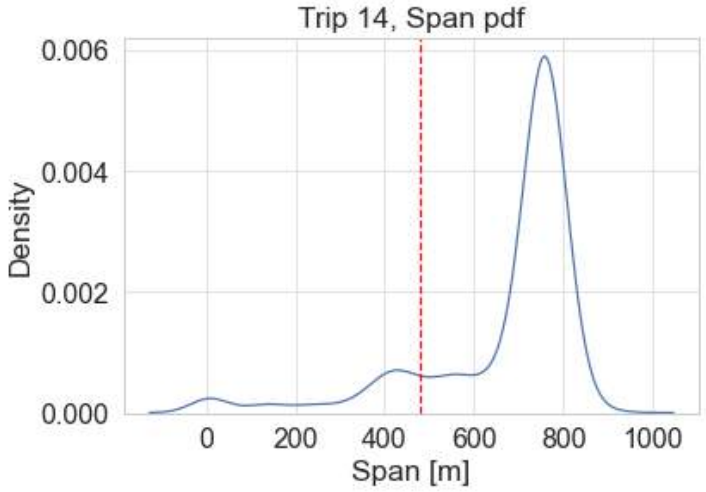

Figure B.10: Span PDF, Trip 14

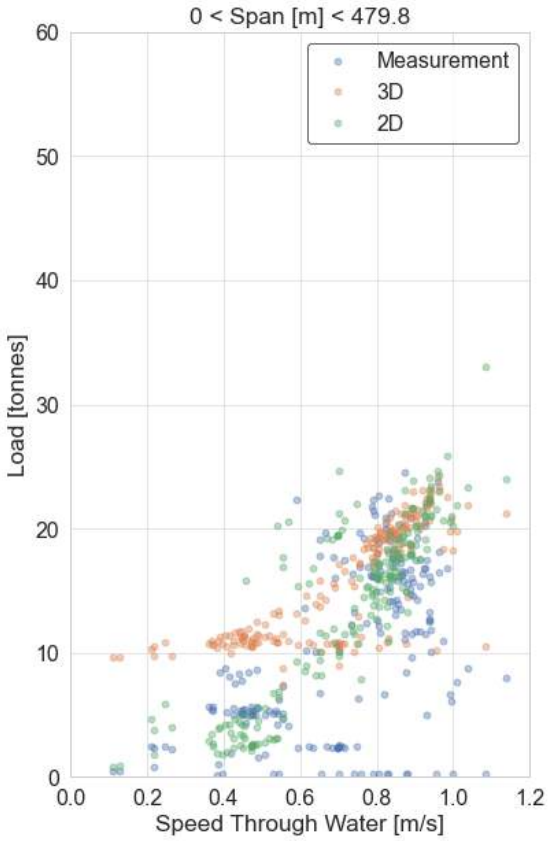

Figure B.11: Trip 14, small span results

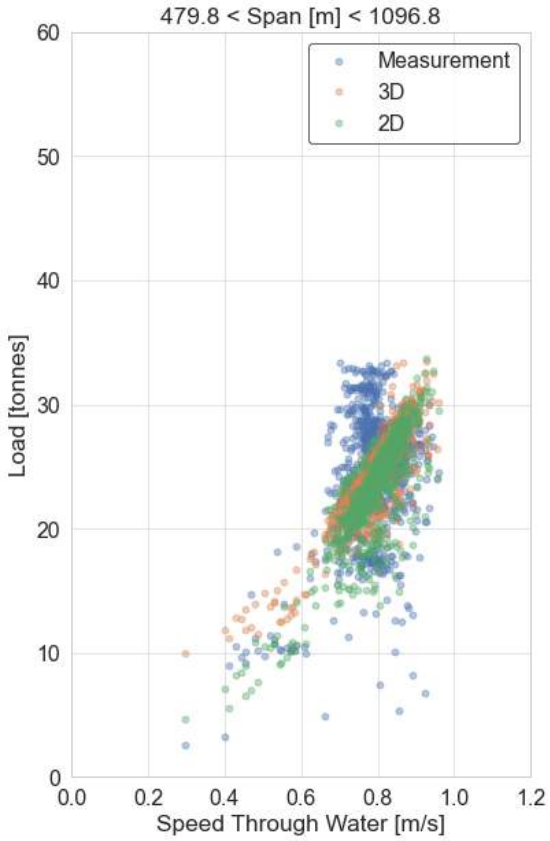

Figure B.12: Trip 14, wide span results

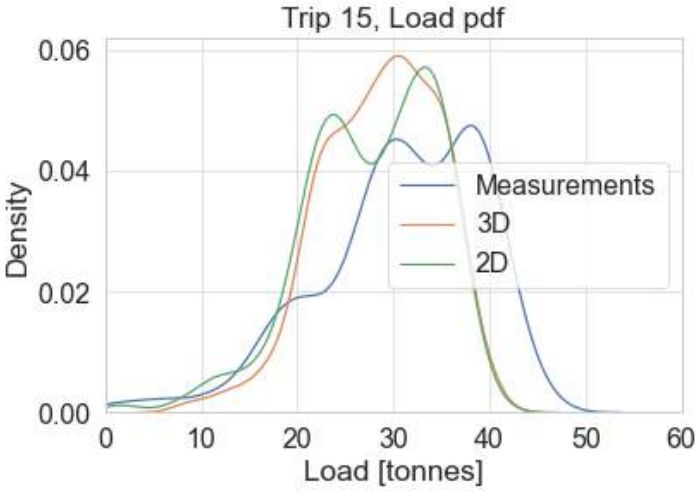

Figure B.13: Load PDF, Trip 15

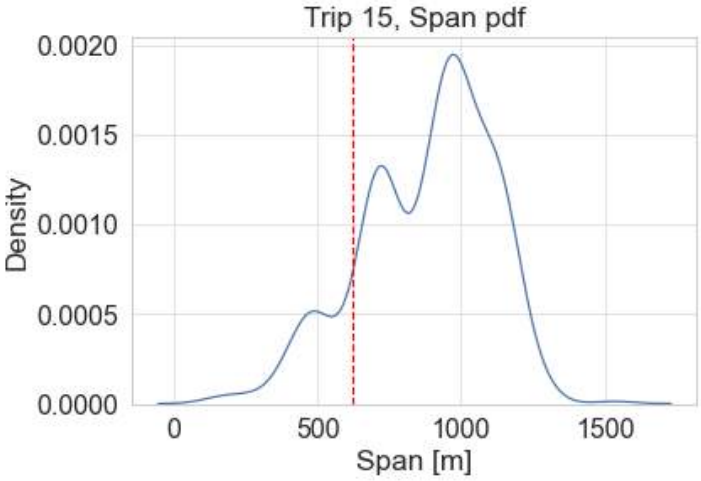

Figure B.14: Span PDF, Trip 15

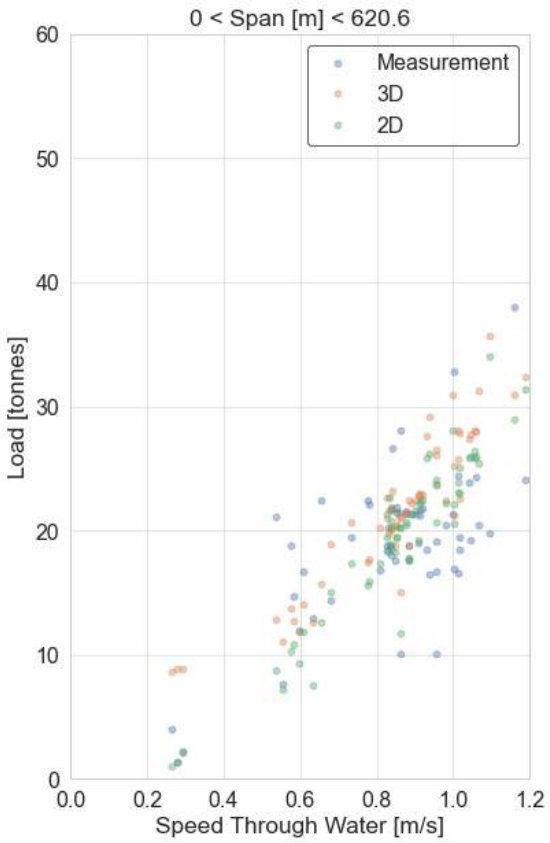

Figure B.15: Trip 15, small span results

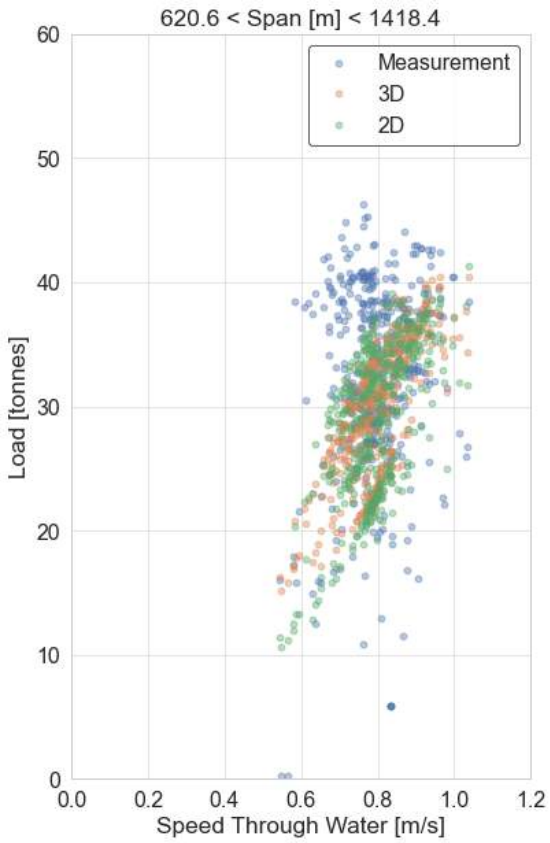

Figure B.16: Trip 15, wide span results

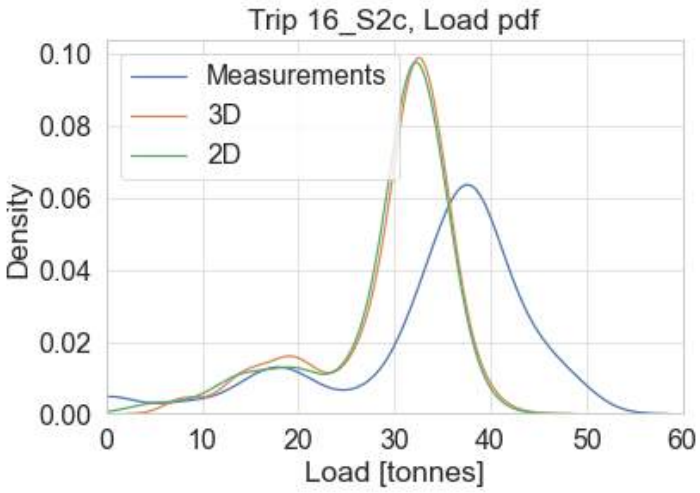

Figure B.17: Load PDF, Trip 16_S2c

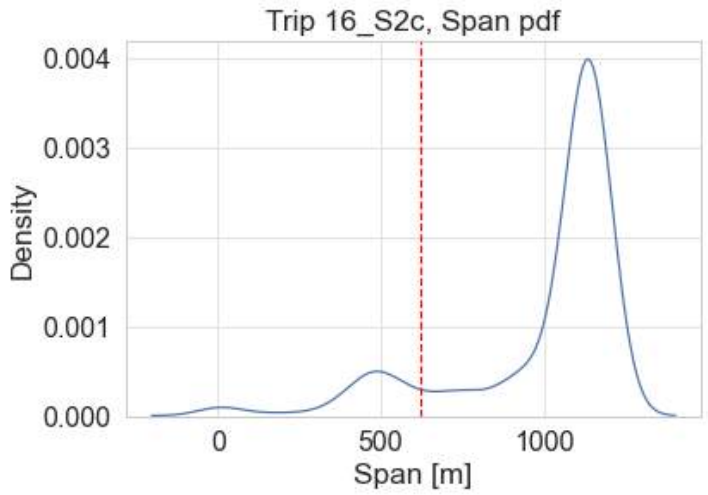

Figure B.18: Span PDF, Trip 16_S2c

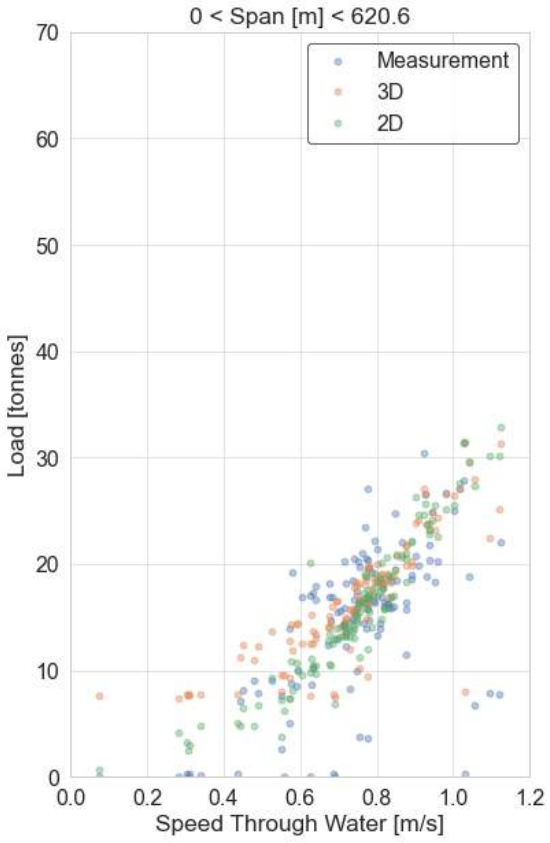

Figure B.19: Trip 16_S2c, small span results

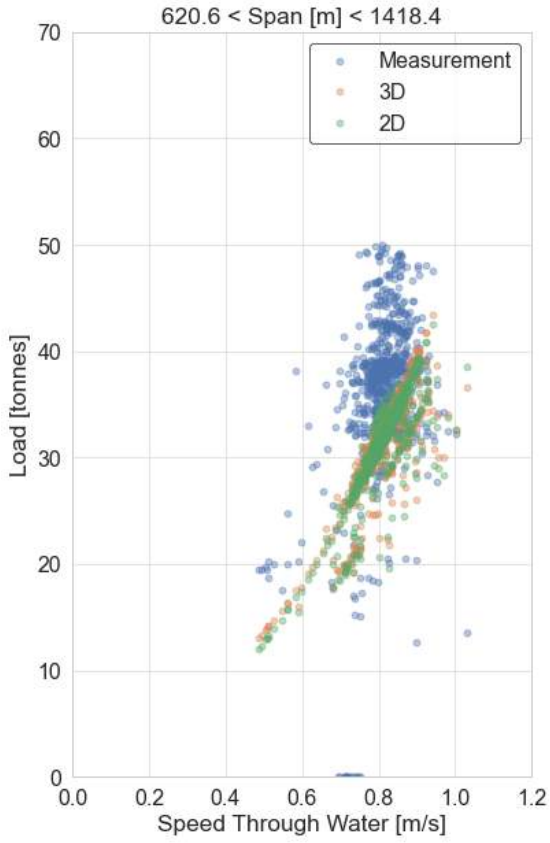

Figure B.20: Trip 16_S2c, wide span results

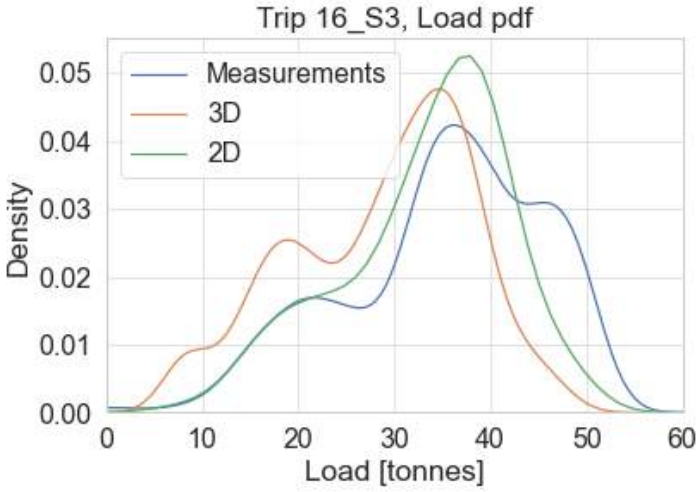

Figure B.21: Load PDF, Trip 16_S3

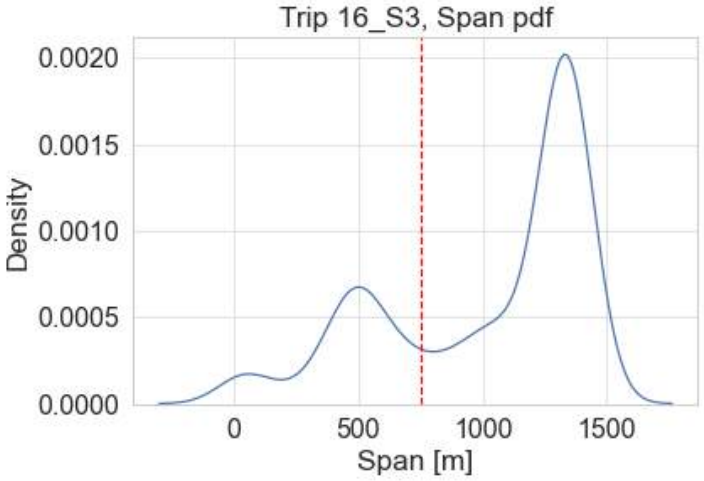

Figure B.22: Span PDF, Trip 16_S3

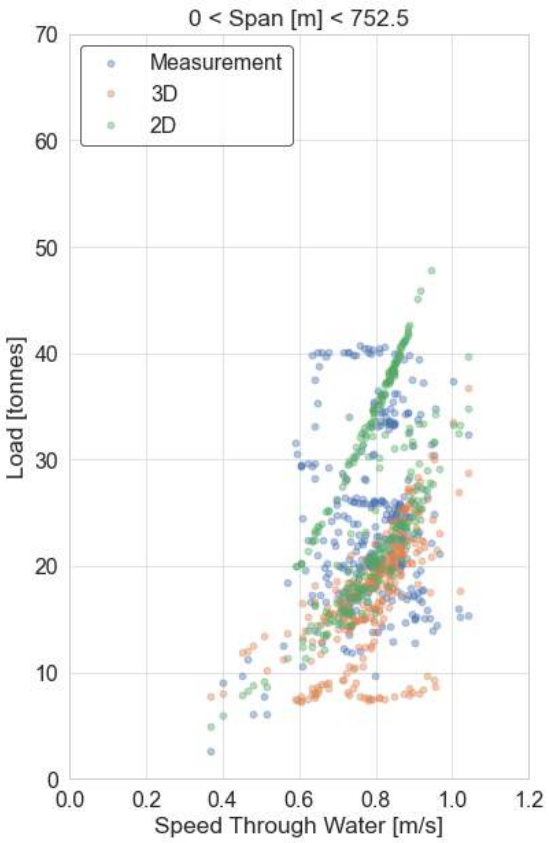

Figure B.23: Trip 16_S3, small span results

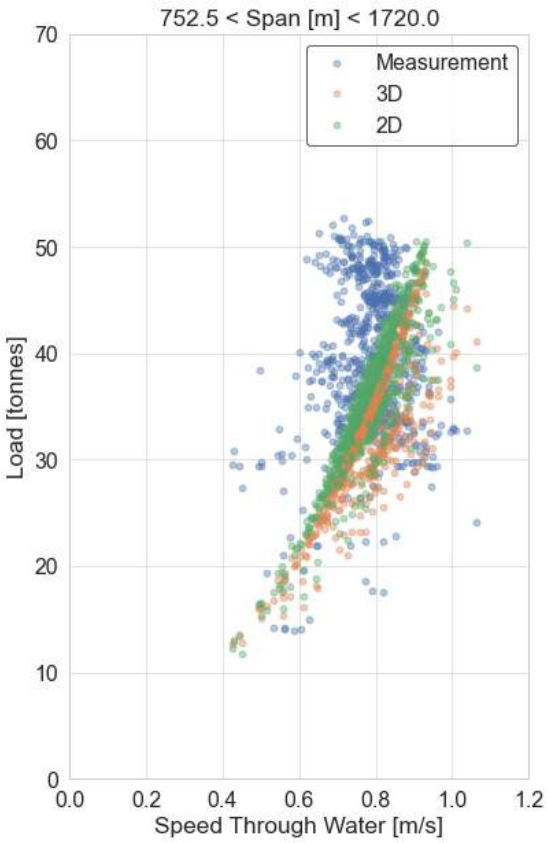

Figure B.24: Trip 16_S3, wide span results

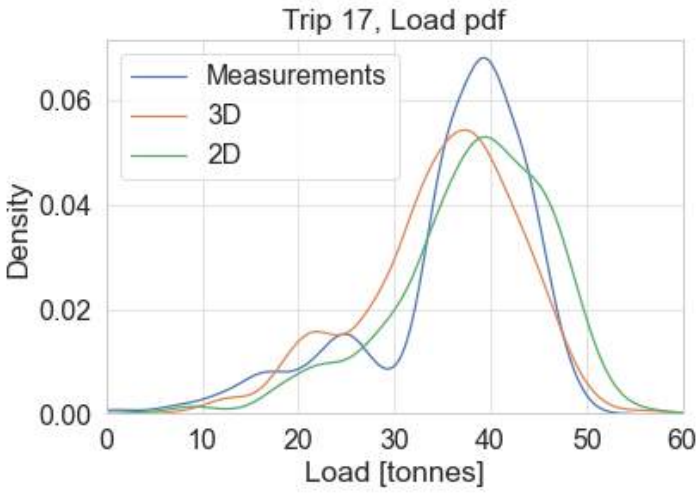

Figure B.25: Load PDF, Trip 17

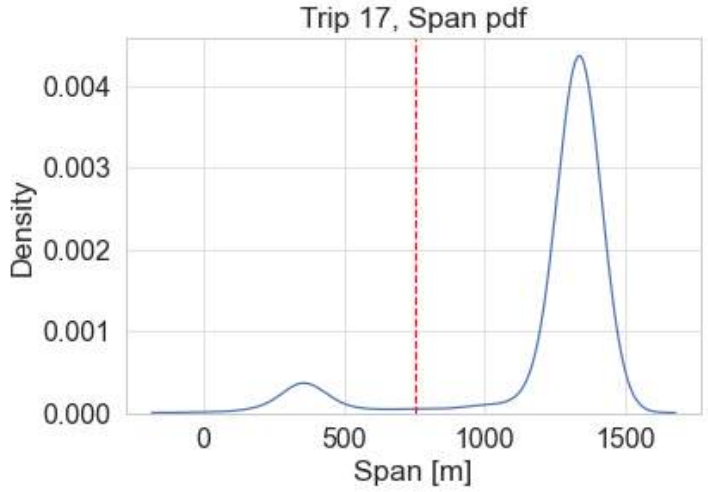

Figure B.26: Span PDF, Trip 17

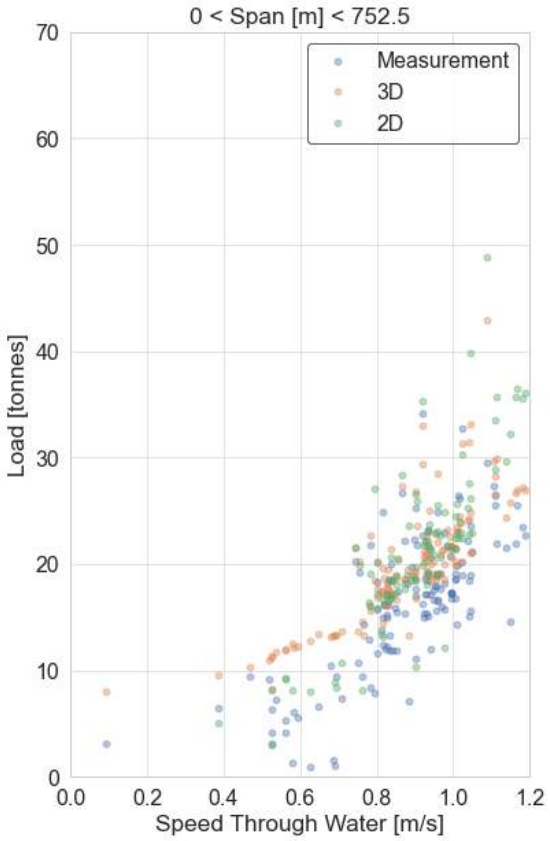

Figure B.27: Trip 17, small span results

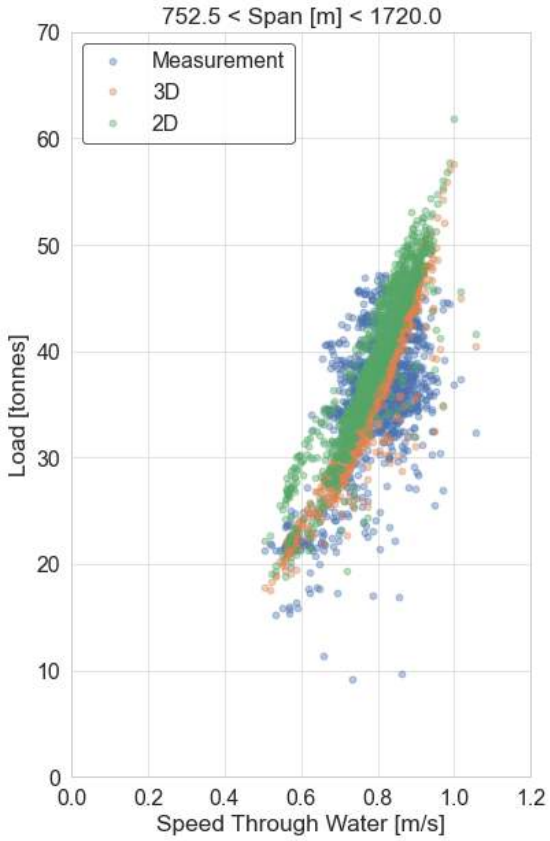

Figure B.28: Trip 17, wide span results

C

Model Results in Numbers

All trips combined			
# Segments	**# Cases**	**Sim.time per case [s]**	**Sim. time [s]**
15	1571	0.14	1012

Total: load = 16.92 kg/m	**3D**	**2D**
MAE [kg/m]	3.75	3.70
Error [%]	22.1	21.9

Small: load = 8.62 kg/m	**3D**	**2D**
MAE [kg/m]	4.22	5.58
Error [%]	49.0	64.8

Wide: load = 18.23 kg/m	**3D**	**2D**
MAE [kg/m]	3.67	3.41
Error [%]	20.1	18.7

Table C.1: All trips combined

		Trip 12	Trip 13	Trip 14	Trip 15	Trip 16_S2c	Trip 16_S3	Trip 17	All
Total									
2D	Error [%]	**13.5**	34.1	15.7	**16.4**	19.7	**20.3**	15.7	**21.9**
3D	Error [%]	39.3	**33.2**	**15.1**	16.8	**18.7**	23.7	**15.1**	22.1
Small span									
2D	Error [%]	**22.8**	**112.2**	60.0	**20.3**	32.6	**30.8**	26.7	64.8
3D	Error [%]	175.7	148.7	**59.2**	23.9	**29.2**	37.3	**20.7**	**49.0**
Wide span									
2D	Error [%]	**13.5**	31.8	12.4	**16.0**	18.8	**17.8**	15.2	**18.7**
3D	Error [%]	38.9	**29.8**	**11.8**	16.2	**18.0**	20.4	**14.8**	20.1

Figure C.1: 2D and 3D model results